TECHNISCHE
UNIVERSITÄT
WIEN
Vienna, Austria

DISSERTATION

Global and seasonal analysis of ^{7}Be concentrations and large-scale atmospheric circulation dynamics

ausgeführt zum Zwecke der Erlangung des akademischen Grades einer Doktorin
der technischen Wissenschaften unter der Leitung von

Privatdoz. Mag.rer.nat. Dr.techn. Georg Steinhauser
und
Ao. Univ. Prof. Dipl.-Ing. Dr.techn. Helmuth Böck
Atominstitut, Technische Universität Wien

eingereicht an der Technische Universität Wien
Fakultät für Physik von

Dott. Mag. Lucrezia Terzi
Matrikelnummer 11802317

Vienna, June 2020

To Martin and my children

Leonhard, Philipp, Marie and Isabelle.

Abstract

Beryllium-7 (^{7}Be) is a cosmogenic radionuclide formed through collision between highly energetic particles (cosmic rays) and atmospheric constituents such as oxygen and nitrogen. Once formed ^{7}Be attaches to aerosol particles and is transported around the globe according to atmospheric circulation dynamics.

Since the 1960's ^{7}Be is known to be an ideal atmospheric tracer due to its steady production in the upper troposphere and lower stratosphere (UTLS region), its short half-life and its worldwide detectability.

In a simplified scheme Hadley, Ferrel and Polar cells are the three large scale atmospheric cells present in both northern and southern Hemisphere. Hadley is the driving cells followed by polar and the resulting eddy Ferrel cells in between.

Beryllium-7 reaches the surface primarily through the downward branch of the Hadley cell, or Hadley-Ferrel-Divergence Zone (HFDZ). Highest concentrations of ^{7}Be are found in correlation with the downward branch of the Hadley cell providing clear signatures for the interface zones position at any point in time. ^{7}Be-rich stratospheric air is transported to the troposphere episodically within tropopause folds along the axis of the subtropical as well as the polar jet stream. This process is referred to as stratospheric intrusion.

The surface air is monitored for radionuclide particles by the International Monitoring System (IMS) of the Comprehensive Nuclear-Test-Ban-Treaty Organization (CTBTO). Upon completion, its radionuclide network (RN) will consist of 80 stations worldwide.

Although the primary goal of the IMS is to detect nuclear test explosions, for calibration purposes, daily activity concentrations of ^{7}Be are recorded creating a unique dataset for civil and scientific applications.

Global coverage of IMS RN stations allows to interpolate ^{7}Be activity concentrations from different locations and study the progression of the atmospheric cells over time. This has a major implication: with 20 years' worth of data, any decadal atmospheric process that affects the stratosphere-troposphere exchange (STE) can be studied through the eyes of ^{7}Be. As STE is connected to the global atmospheric circulation and its seasonal and multi-year changes, the analysis of ^{7}Be allows and improved understanding of these changes.

Subjects considered for this research work include: intertropical convergence zone (ITCZ), solar cycle, Walker circulation pattern, El Niño southern oscillation (ENSO), quasi-biannual oscillation (QBO), sudden stratospheric warming (SSW) events, solar energetic particle (SEP) events, monsoons, tropopause breathing and static weather patterns.

This work describes how these radionuclides can be used to predict seasonal weather and shows that decadal change patterns such as weakening of general circulation and poleward movement of Hadley cell can also be monitored effectively through such cosmogenic radionuclides. These changes may be attributable to global warming.

Beryllium-7 data indicate that change phenomena observed within the ^{7}Be records are not primarily driven and cannot be explained by solar flux or earth magnetic field variations.

Furthermore, ^{7}Be is a good tracer for tropopause height changes which are presumably related to the rising of CO_2 concentrations which is also the main driver for extended summer periods.

Near-surface measurement of cosmogenic radionuclides can help address outstanding challenges in atmospheric circulation research by integrating a new perspective across the disciplines of environmental radiation monitoring and meteorology. After decades of research, an improved understanding of STE, including its causes and its consequences, is still needed.

Kurzfassung

Beryllium-7 (^{7}Be) ist ein kosmogenes Radionuklid, das durch Kollision zwischen hochenergetischen Partikeln (kosmischen Strahlen) und atmosphärischen Bestandteilen wie Sauerstoff und Stickstoff gebildet wird. Einmal gebildet, bindet sich ^{7}Be an Aerosolpartikel und wird entsprechend der atmosphärischen Zirkulationsdynamik um den Globus transportiert. Seit den 1960er Jahren ist ^{7}Be aufgrund seiner stetigen Produktion in der oberen Troposphäre und unteren Stratosphäre (UTLS-Region), seiner kurzen Halbwertszeit und seiner weltweiten Nachweisbarkeit ein idealer atmosphärischer Tracer.

In einem vereinfachten Schema sind Hadley-, Ferrel- und Polarzellen die drei großräumigen atmosphärischen Zellen, die sowohl in der nördlichen als auch in der südlichen Hemisphäre vorhanden sind. Hadley ist die treibende Zelle, gefolgt von polaren und den resultierenden Wirbel-Ferrel-Zellen dazwischen.

Beryllium-7 erreicht die Oberfläche hauptsächlich über den nach unten gerichteten Zweig der Hadley-Zelle oder die Hadley-Ferrel-Divergenzzone (HFDZ). Die höchsten Konzentrationen von ^{7}Be werden in Korrelation mit dem nach unten gerichteten Zweig der Hadley-Zelle gefunden, was zu jedem Zeitpunkt eindeutige Signaturen für die Position der Grenzflächenzonen liefert. ^{7}Be-reiche stratosphärische Luft wird episodisch innerhalb von Tropopausenfalten entlang der Achse des subtropischen sowie des polaren Strahls in die Troposphäre transportiert. Dieser Prozess wird als stratosphärisches Eindringen bezeichnet.

Die Oberflächenluft wird vom International Monitoring System (IMS) der Comprehensive Nuclear-Test-Ban-Treaty Organization (CTBTO) auf Radionuklidpartikel überwacht. Nach Fertigstellung wird das Radionuklidnetzwerk (RN) aus 80 Stationen weltweit bestehen.

Obwohl das Hauptziel des IMS darin besteht, Explosionen von Atomtests zu erkennen, werden zu Kalibrierungszwecken tägliche Aktivitätskonzentrationen von ^{7}Be aufgezeichnet, wodurch ein einzigartiger Datensatz für zivile und wissenschaftliche Anwendungen erstellt wird.

Die globale Abdeckung von IMS-RN-Stationen ermöglicht es, ^{7}Be-Aktivitätskonzentrationen von verschiedenen Orten aus zu interpolieren und den zeitlichen Verlauf der atmosphärischen Zellen zu untersuchen. Dies hat eine wichtige Auswirkung: Mit Daten aus 20 Jahren kann jeder dekadische atmosphärische Prozess, der den Stratosphäre-Troposphäre-Austausch (STE) beeinflusst, mit den Augen von ^{7}Be untersucht werden. Da STE mit der globalen atmosphärischen Zirkulation und ihren saisonalen und mehrjährigen Veränderungen verbunden ist, ermöglicht die Analyse von ^{7}Be ein besseres Verständnis dieser Veränderungen.

Zu den für diese Forschungsarbeit berücksichtigten Themen gehören: intertropische Konvergenzzone (ITCZ), Sonnenzyklus, Walker-Zirkulationsmuster, El Niño-Südschwingung (ENSO), quasi halbjährliche Schwingung (QBO), plötzliche stratosphärische Erwärmung (SSW), solarenergische Partikel (SEP) Ereignisse, Monsun, Tropopausenatmung und statische Wettermuster.

Diese Arbeit beschreibt, wie diese Radionuklide zur Vorhersage des saisonalen Wetters verwendet werden können, und zeigt, dass dekadische Veränderungsmuster wie die Abschwächung von Passatwinden und die Poleward-Bewegung von Hadley-Zellen auch durch solche kosmogenen Radionuklide effektiv überwacht werden können. Diese Veränderungen können auf die globale Erwärmung zurückzuführen sein.

Beryllium-7-Daten weisen darauf hin, dass in den ^{7}Be-Aufzeichnungen beobachtete Änderungsphänomene nicht primär gesteuert werden und nicht durch Sonnenfluss- oder Erdmagnetfeldschwankungen erklärt werden können.

Darüber hinaus ist ^{7}Be ein guter Indikator für Höhenänderungen in der Tropopause, die vermutlich mit dem Anstieg der CO_2-Konzentrationen zusammenhängen, was auch der Haupttreiber für längere Sommerperioden ist.

Die oberflächennahe Messung kosmogener Radionuklide kann dazu beitragen, herausragende Herausforderungen in der atmosphärischen Zirkulationsforschung zu bewältigen, indem eine neue Perspektive in die Disziplinen Umweltstrahlungsüberwachung und Meteorologie integriert wird. Nach jahrzehntelanger Forschung ist immer noch ein besseres Verständnis von STE einschließlich seiner Ursachen und Folgen erforderlich.

Schlüsselwörter: kosmogene Radioisotope, Radionuklidüberwachung, ^{7}Be, atmosphärische Dynamik, saisonale Wettervorhersage, Monsun, Klimawandel, Erhöhung der Tropopause.

Contents

Introduction

The present thesis develops different methodologies to study global atmospheric dynamics through the eyes of cosmogenic radioisotopes. The study focuses on beryllium-7 (^{7}Be) which is monitored worldwide thanks to the radionuclide stations of the International Monitoring System (IMS).

The aim is to explore possible civil and scientific applications of ^{7}Be monitoring. In terms of atmospheric circulation and meteorological phenomena, what can this isotope see on the global scale? Where can it be efficiently applied as a large-scale atmospheric tracer? When can it provide value added to classic meteorological measurement tools?

This thesis is subdivided into four chapters:

- Chapter 1 introduces the main concepts related to ^{7}Be production, its transport and measurement of isotopic activity concentrations derived from previous studies and literature.

- Chapter 2 presents different statistical methods applied to ^{7}Be data. The original dataset is presented as daily activity concentrations from worldwide measurement stations which show a strong variability and need to be post process to filter out local processes such as wash out effect due to precipitation. Data are then combined into surface interpolation maps at local, regional or global level.

- Chapter 3 discusses the correlation results between ^{7}Be and relevant meteorological phenomena: The first step was to establish the ^{7}Be signature correspondent to the atmospheric cell interface zones.
  Once this was verified the research moved into utilizing ^{7}Be timeseries to study atmospheric processes like El Nino Southern Oscillation and the Indian monsoon. Finally, ^{7}Be data have been used to study current circulation changes involving

tropopause height and stalling of weather systems possibly related to global warming. As some of these changes are labelled with medium to low confidence in the most recent assessment report of the Intergovernmental Panel on Climate Change (IPCC)[33], using ^{7}Be as a new analysis tool could be beneficial.

- Chapter 4 summarizes the findings and highlights of ^{7}Be as a tracer for STE and the global atmospheric dynamics. ^{7}Be has been utilized to study a comprehensive spectrum of meteorological phenomena and therefore this work should promote further research into the field of cosmogenic radionuclides. The strength of the presented methodologies resides in the combination with current atmospheric tracking tools. ^{7}Be is a reliable complementary tool for seasonal weather prediction and provide a simple and straightforward solution for tracking the ongoing changes in the atmospheric circulation probably driven by anthropogenic global temperature increase.

Chapter 1

1.1. Beryllium-7

Berylium-7 is a cosmogenic radioisotope and decays with a 53.2 days half-life by electron capture into lithium-7. This isotope is largely produced in the UTLS region [39, 96] as a result of spallation of nuclei of atmospheric gases, mainly oxygen and nitrogen (Figure 2).

Spallation is a process where high-energy particles hit heavy nucleus resulting in the emission of numerous nucleons, thereby greatly reducing the atomic weight of the particles involved.

As shown in Figure 1, production rates are approximately twice as high in the stratosphere as in the troposphere.
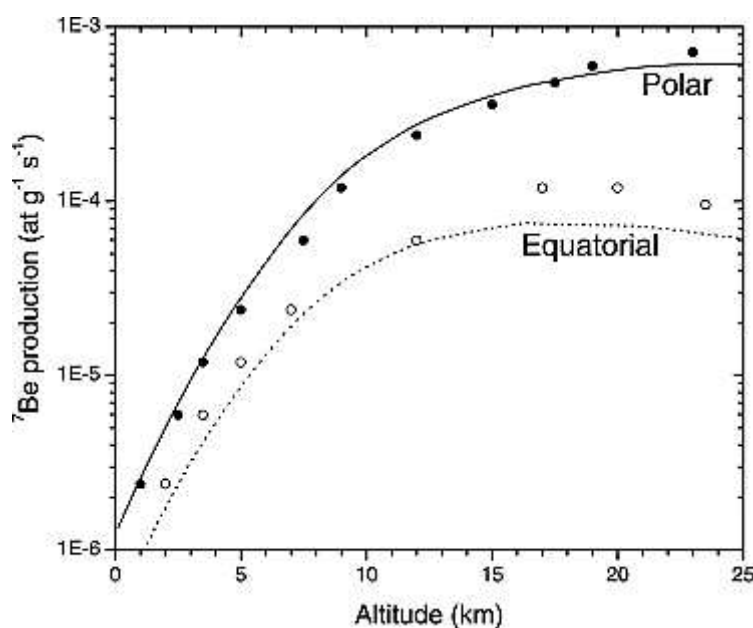

Figure 1 ^{7}Be production is governed by the exponential decrease of atmospheric pressure and the exponential increase of cosmogenic radiation with height. (Usoskin et al., 2008)[99]

Once created, radionuclides attach to aerosols and are subject to atmospheric circulation until they decay.

Aerosols are transported horizontally and vertically by winds and redistributed vertically by gravitational sedimentation. They are ultimately removed by wet deposition in the troposphere (within and below the cloud level) and dry deposition through interaction with the surface. ^{7}Be is further removed from the atmosphere due to its radioactive decay. Most important for the surface concentrations of ^{7}Be is, besides its global production rate, the global STE strength.

Concentrations of ^{7}Be vary from the order of hundreds mBq/m³ in the lower stratosphere to tens mBq/m³ in the upper troposphere. The surface air contains a few mBq/m³ worldwide [21]. While ^{7}Be is present in surface air all around the globe, it has unique source and sink characteristics[35], and therefore ^{7}Be is a suitable tracer for atmospheric dynamics. It has been shown that ^{7}Be is generated steadily and its production increases as one approaches the poles[40], with maximum concentration levels in the stratosphere at mid-latitudes,, which makes its transport a good indicator of STE[35]. The ^{7}Be production rate is not only dependent on the altitude in the atmosphere, but has temporal variation over the 11-year solar cycle[39]. It exhibits latitudinal variation due to the deflection of incoming cosmic rays, as the earth magnetic field is stronger above the equator. Worldwide ^{7}Be concentrations on ground level follow an annual cycle because its transport in the atmosphere is regulated by the seasonal atmospheric processes[39].

Lal and Peters published already in 1962 regarding the strong links between atmospheric phenomena and ground level ^{7}Be activity concentrations[39]. Two main processes determine the abundance of these isotopes at ground level: (1) the production rate in the UTLS region, and (2) the subsequent transport to the surface (Figure 2). At lower altitudes during horizontal transport, the ^{7}Be concentration may be diminished by dilution and rainout. There is a clear dependency between the transport processes investigated in this thesis and changes in the atmospheric circulation patterns during the last decade[72].
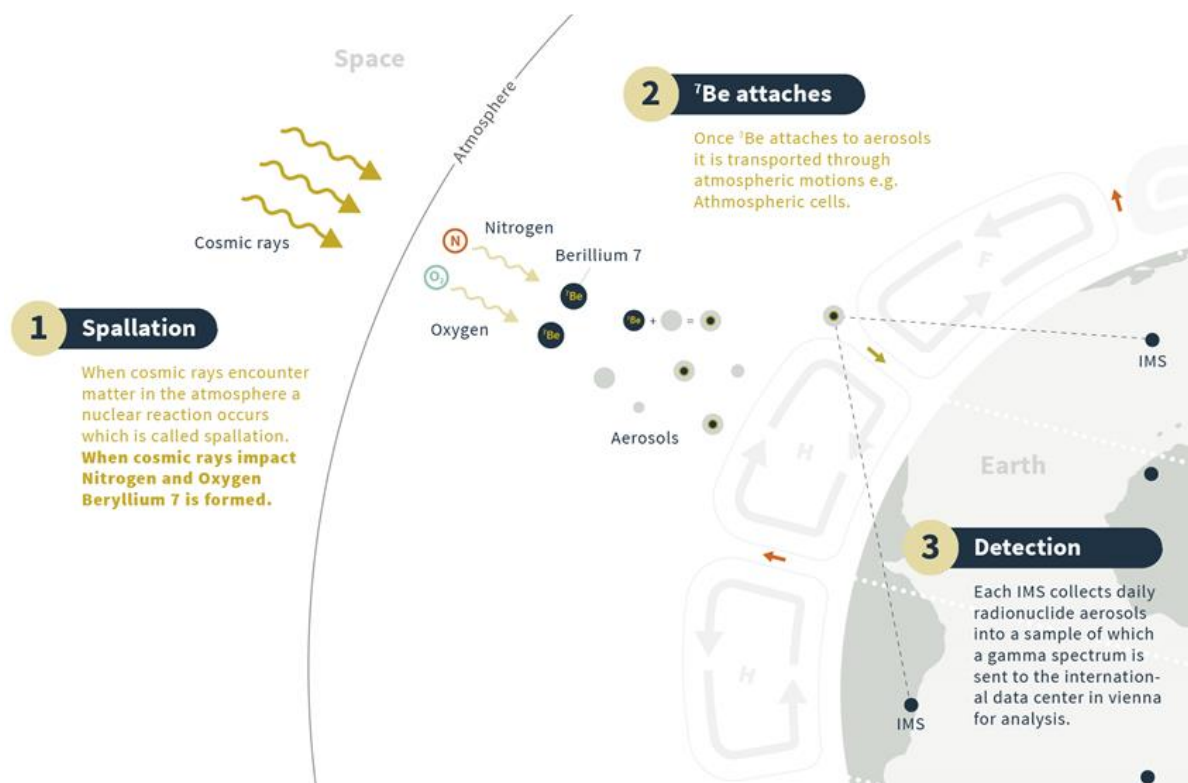
Figure 2. **⁷Be origin, production and transport. H and F indicate Hadley and Ferrel cells respectively. (Terzi et al., 2019)**

1.2. Production through cosmic rays

The production of cosmogenic radioisotopes in the UTLS region is governed by incoming cosmic rays[16, 21, 27, 35, 52]. The incoming flux density of cosmic rays (solar irradiance, frequently referred to as solar constant which is slightly misleading) is not constant but is modulated on shorter timescales by the approximately 11-year cycle of solar activity[22]. An increased solar activity, as indicated by a higher number of sunspots, is accompanied by strong magnetic fields that retain charged particles. Thus, the flux density of cosmic rays reaching the Earth is anti-correlated with the number of sunspots[22]. Other known variations of the solar irradiance are acting on much longer time scales and are thus irrelevant for this study.

Since an increased influx of cosmic rays leads to a proportionally increased spallation activity, an analysis of the radionuclide concentrations at ground level with a focus on atmospheric circulation must include a correction against these variations in the production.

The large uncertainties in current observational data are identified as a major reason for this by Dohmse et al. (2016)[17]. The database of global ^{7}Be observations presented here may contribute to reducing these uncertainties.

There are also other relevant factors impacting ^{7}Be formation. Delaygue et al. (2015)[16] find that stratospheric aerosol load to be highly variable and suggest that it can, for example, increase by more than two orders of magnitude following volcanic eruptions. Lederer (2007)[43] also suggest large forest fires may episodically inject aerosols into the stratosphere.

Sodium-22 (^{22}Na) another cosmogenic radionuclide produced by spallation of cosmic rays with argon but with longer half-life (2.6 years), can help in reducing uncertainties between transport and production processes.

Analysing ^{22}Na/^{7}Be ratio provides a better indicator for the origin of air masses, since the ratio is very sensitive to the height of production with much lower values in the lower stratosphere than in the upper troposphere. Unfortunately, due to the much lower abundance of ^{22}Na no global ^{22}Na dataset is available comparable to the further discussed ^{7}Be data.

1.3. Transport through atmospheric processes

The second process, which is the transport of ^{7}Be from the UTLS region to the surface, is mainly governed by the systematic vertical downward movement taking place within the descending branch of the Hadley Cell also referred to in this thesis as the Hadley-Ferrel-Divergence Zone (HFDZ)[81,86,89]. As shown in Figure 3 the HFDZ features the large-scale downward movement of air masses, while the tropical and polar interface zones feature convergence and upward movements. The HFDZ follows an annual cyclic latitudinal movement due to the poleward expansion of the Hadley cell during summer seasons in the respective hemispheres[21].

STE, however, is not limited to the HFDZ and the sub-tropics. It is also observed regularly in the mid-latitudes associated to tropopause folding close to the axis of the polar jet. Such STE events are mostly not associated with direct transport to the surface, but they inject air of stratospheric origin into the mid- to upper troposphere. Such stratospheric intrusions show a seasonal pattern related to mid-latitude frontal activity, with a maximum in winter and spring and a pronounced minimum in summer.
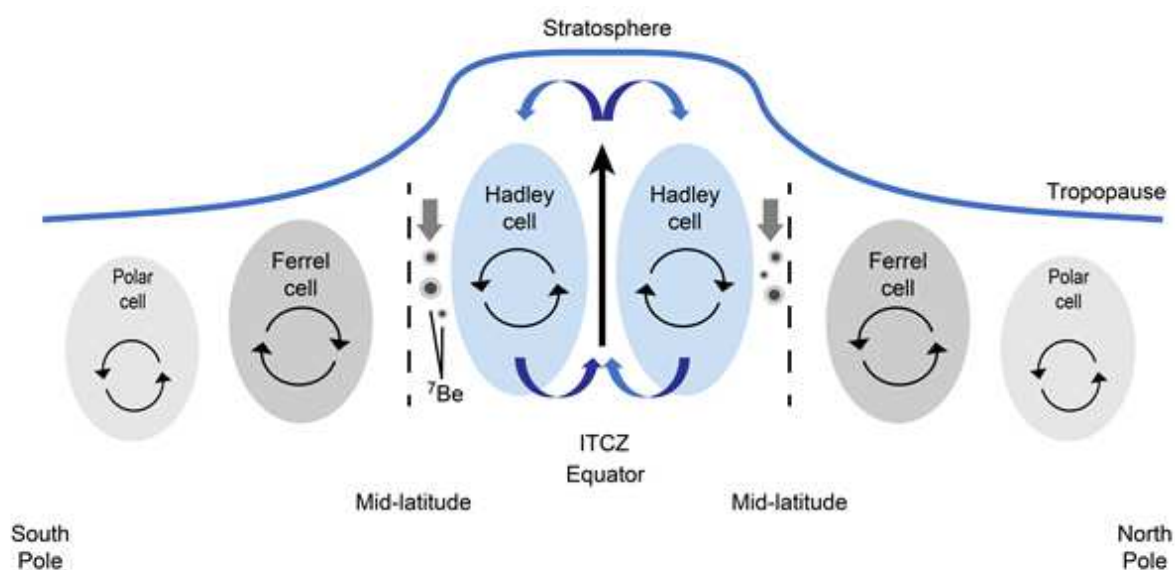
Figure 3. Simplified diagram featuring the downward branch of the Hadley cell and the eddy Ferrel cell. The tropopause separates stratosphere from troposphere. [7]Be as indicated in the picture is transported from the UTLS region to the surface ground thanks to downward vertical influx of air masses taking place in the interface zone also called the STE of the HFDZ. (Terzi et al., 2020)

[7]Be attaches to aerosol particles which are removed mainly by wet deposition. This effect of wash out by precipitation is highly marked in the intertropical convergence Zone (ITCZ)[37]. Although wash out effect is a predominant effect at ITCZ, it has been shown by numerous studies based on surface measurement that to disentangle different factors affecting the [7]Be variability is not straightforward. A recent example of this finding is the study by Taylor et al. (2016)[88] who use sampling sites in England (Plymouth and Chilton) and Wales (Aberporth) during 2009 and 2010. They can explain the variability in deposition to a high degree by rainfall dynamics. The study also identifies STE and convective circulation within the troposphere as factors influencing the [7]Be concentrations. Another recent confirmation of the influence of atmospheric circulations is provided by Neroda et al. (2016)[56]. They report a seasonal variation of [7]Be concentration in Vladivostok, Russia, for the years 2013-2014. Neroda et al. (2016)[56] use a regression model for meteorological data and aerosol concentrations. This confirms that the direction and height of incoming air masses strongly influence [7]Be concentration. Inclusion of meteorological data along backward trajectories also improves their analysis.

Before better methods of observing stratospheric ozone were available, STE was utilized to determine the stratospheric ozone content by measuring [7]Be /ozone (O_3) ratios at ground level. See for example Dutkiewicz and Husain (1979)[19]. The correlation of [7]Be with O_3 on surface

level remains a topic of current research[42]. In this study the day-to-day variations were smoothened out by the post-processing of the data, as described in the following chapter. Longer time scales are more robust against such fluctuations.

Since the 1960s it is known that ^{7}Be due to its short half-life and global detection, serves as an ideal tracer to study STE and circulation dynamics. Literature on ^{7}Be, however, is mainly local or regional so far, covering limited areas.

Previous studies publicised the efficiency of radionuclides as a tracer for atmospheric processes focusing on Hadley cells and the ITCZ. However, the sampled locations were limited to a small number of sites where air was sampled and mainly focusing the research on a local or regional scale. Bollhöfer and Schlosser (2014)[8] for example studied correlation between ITCZ and ^{85}Kr at a single location in Darwin. Doering and Saey (2014)[18] reconcile the Hadley cell seasonal shift with ^{7}Be annual cycles measured at four Australian IMS Stations. Läppanen and Usoskin (2012)[45] observed ^{7}Be periodicities in connection to large scale atmospheric processes using data from four stations in Finland.

This thesis presents ^{7}Be on a global scale and attempts to highlight the full potential of this isotope.

Around 270,000 samples have been analysed and collected from over 70 different locations worldwide. 62 sites provide longer time series covering 7 to 20 years of data (see Table 1). This level of data coverage allows to visualize the location of the HFDZ, the PFCZ and the ITCZ through ^{7}Be maps covering the whole world. It describes the seasonal shift of these zones at longitudinal bands over the course of one year. The spatial and temporal development of the convergence zone can be quantified by interpolating an approximate speed of the cell progression.

Table 1. International Monitoring System Stations used in this thesis. (www.CTBTO.org)

A

Total n. of stations	62
Total n. of samples	268752
Average time series length (n. of years)	12
Minimum time series length (n. of years)	7
Maximum time series length (n. of years)	16
Outliers filtered out (single spikes above factor of 2 over overall average). Filtered data averaged over 0/-120 days and normalized over overall average (2003-2019).	

B

Station code	Treaty number	State	Location	Latitude	Longitude	N. of samples from 2003-2019 (5967 days)
ARP01	RN01	Argentina	Buenos Aires	-34.54	-58.47	5784
ARP03	RN03	Argentina	Bariloche	-41.15	-71.16	4563
AUP04	RN04	Australia	Melbourne, VIC	-37.73	145.10	5776
AUP05	RN05	Australia	Mawson, Antarctica	-67.60	62.87	2387
AUP06	RN06	Australia	Townsville, QLD	-19.25	146.77	5476
AUP07	RN07	Australia	Macquarie Island	-54.50	158.95	2673
AUP08	RN08	Australia	Cocos Islands	-12.19	96.83	5342
AUP09	RN09	Australia	Darwin, NT	-12.43	130.89	5291
AUP10	RN10	Australia	Perth, WA	-31.93	115.98	5410
BRP11	RN11	Brazil	Rio de Janeiro	-22.99	-43.42	5405
CMP13	RN13	Cameroon	Edea	3.78	10.15	3450
CAP14	RN14	Canada	Sidney	48.65	-123.45	3381
CAP15	RN15	Canada	Resolute, NU	74.71	-94.97	4089
CAP16	RN16	Canada	Yellowknife, N.W.T.	62.48	-114.47	5668
CAP17	RN17	Canada	St. John's N.L.	47.59	-52.74	4592
CLP18	RN18	Chile	Punta Arenas	-53.14	-70.88	4685
CLP19	RN19	Chile	Hanga Roa, Easter Island	-27.13	-109.35	3582
CKP23	RN23	Cook Islands	Rarotonga	-21.20	-159.81	5467
FJP26	RN26	Fiji	Nadi	-17.76	177.45	4775
FRP27	RN27	France	Papeete, Tahiti	-17.57	-149.57	4410
FRP28	RN28	France	Pointe-à-Pitre, Guadeloupe	16.26	-61.53	3844
FRP29	RN29	France	Réunion	-20.91	55.59	4575
FRP30	RN30	France	Port-aux-Français, Kerguelen	-49.35	70.26	4170
FRP31	RN31	France	Kourou, French Guiana	5.17	-52.69	4453
DEP33	RN33	Germany	Schauinsland/Freiburg	47.92	7.91	4144
ISP34	RN34	Iceland	Reykjavik	64.13	-21.90	4185
JPP37	RN37	Japan	Okinawa	26.50	127.90	4342
JPP38	RN38	Japan	Takasaki, Gunma	36.30	139.08	4683
KIP39	RN39	Kiribati	Kiritimati	2.01	-157.39	3200
KWP40	RN40	Kuwait	Kuwait City	29.34	47.91	3718
MYP42	RN42	Malaysia	Tanah Rata	4.48	101.37	3572

Station code	Treaty number	State	Location	Latitude	Longitude	N. of samples from 2003-2019 (5967 days)
MRP43	RN43	Mauritania	Nouakchott	18.14	-15.92	4206
MXP44	RN44	Mexico	Guerrero Negro, Baja California	27.96	-114.06	2654
MNP45	RN45	Mongolia	Ulaanbaatar	47.89	106.33	5288
NZP46	RN46	New Zealand	Chatham Island	-43.82	-176.48	4827
NZP47	RN47	New Zealand	Kaitaia	-35.07	173.29	5614
NOP49	RN49	Norway	Spitsbergen	78.23	15.39	4215
PAP50	RN50	Panama	Panama City	8.98	-79.53	4863
PGP51	RN51	Papua New Guinea	Kavieng, New Ireland	-2.58	150.81	3902
PHP52	RN52	Philippines	Tanay	14.58	121.37	4706
PTP53	RN53	Portugal	Ponta Delgada, São Miguel, Azores	37.74	-25.70	2422
RUP54	RN54	Russian Federation	Kirov	58.59	49.41	2961
RUP58	RN58	Russian Federation	Ussuriysk	44.15	132.00	3277
RUP59	RN59	Russian Federation	Zalesovo	53.94	84.79	3315
RUP60	RN60	Russian Federation	Petropavlovsk-Kamchatskiy	53.05	158.78	3472
RUP61	RN61	Russian Federation	Dubna	56.74	37.25	3840
SEP63_	RN63	Sweden	Stockholm	59.41	17.95	4814
TZP64	RN64	United Republic of Tanzania	Dar es Salaam	-6.78	39.20	4003
GBP66	RN66	United Kingdom of Great Britain and Northern Ireland	BIOT/Chagos Archipelago	-7.28	72.37	4290
GBP67	RN67	United Kingdom of Great Britain and Northern Ireland	St. Helena	-15.94	-5.67	3769
GBP68	RN68	United Kingdom of Great Britain and Northern Ireland	Tristan da Cunha	-37.07	-12.31	4974
USP70	RN70	United States of America	Sacramento, CA	38.67	-121.36	5030
USP71	RN71	United States of America	Sand Point, AK	55.34	-160.49	4361
USP72	RN72	United States of America	Melbourne, FL	28.10	-80.65	5060
USP73	RN73	United States of America	Palmer Station	-64.77	-64.05	4553
USP74	RN74	United States of America	Ashland, KS	37.17	-99.77	5319
USP75	RN75	United States of America	Charlottesville, VA	38.00	-78.40	5324
USP76	RN76	United States of America	Salchaket, AK	64.67	-147.10	4449
USP77	RN77	United States of America	Wake Island	19.29	166.61	3882
USP78	RN78	United States of America	Midway Islands	28.22	-177.37	3722
USP79	RN79	United States of America	Oahu, HI	21.52	-157.99	4721
USP80	RN80	United States of America	Upi, Guam	13.57	144.93	3827

1.4. Monitoring through the Radionuclide Network

Beryllium-7 datasets analysed in this thesis come from the International Monitoring System operated by the Comprehensive Nuclear-Test-Ban Treaty Organization (CTBTO).

The Comprehensive Nuclear-Test-Ban Treaty (CTBT) first opened for signatures 1996. The treaty bans all nuclear test explosions and establishes an extensive verification regime through its international body, the Provisional Technical Secretariat (PTS) of the Comprehensive Nuclear-Test-Ban Treaty Organization (CTBTO).

To ensure compliance, the CTBT provides the installation of an International Monitoring System (IMS) based on waveform and radionuclide (RN) technologies, the latter of which aims at the detection of signature isotopes from nuclear explosions. The RN network will comprise 80 stations at completion (Figure 4) of which 73 are already certified and operational as of mid-2020.

Each RN station collects daily radionuclide aerosols for 24 h on a filter using a high-volume air sampler. These filters are then measured with a High Purity Germanium (HPGe) detector system (Figure 5). The collected spectra are then sent to the International Data Centre (IDC) of the PTS located in Vienna/Austria for analysis (Figure 6). Stations are operated with a high data availability (95%, i.e. the percentage of the data, on time or delayed, that reaches the IDC per year)[1].

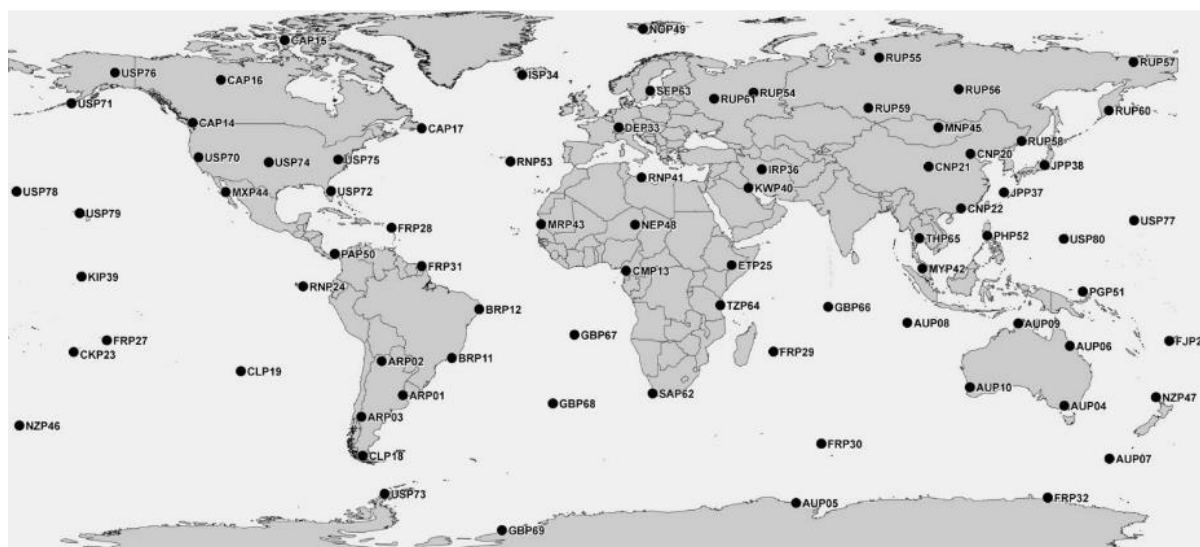[1] Equivalent to ≤ 15 days' downtime annually with ≤ 7 days consecutive.

Figure 4. The radionuclide components of the International Monitoring System. (The original data of this map are found at www.ctbto.org)

For particulate radionuclides, each gamma spectrum is analysed for a defined list of natural isotopes, activation and fission products.

The measurement cycle for one sample consists of 24 h sampling, 24 h decay and 24 h gamma spectral acquisition. The complete sampling cycle is, therefore, 72 h long. The minimum requirements for an IMS particulate radionuclide station are listed in Table 2.

Table 2. Minimum requirements for an IMS particulate radionuclide station. (www.ctbto.org)

| Typical characteristics for an IMS radionuclide particulate station	
Air flow	500 m³/h
Collection time	24 h
Decay time	24 h
Measurement time	20 h
Time before reporting	72 h
Measurement mode	HPGe High resolution gamma spectrometry
HPGe relative efficiency	> 40%
HPGe resolution	< 2.5 KeV at 1332 KeV
Baseline sensitivity	10 to 30 µBq m-3
Calibration range	88 to 1836 KeV
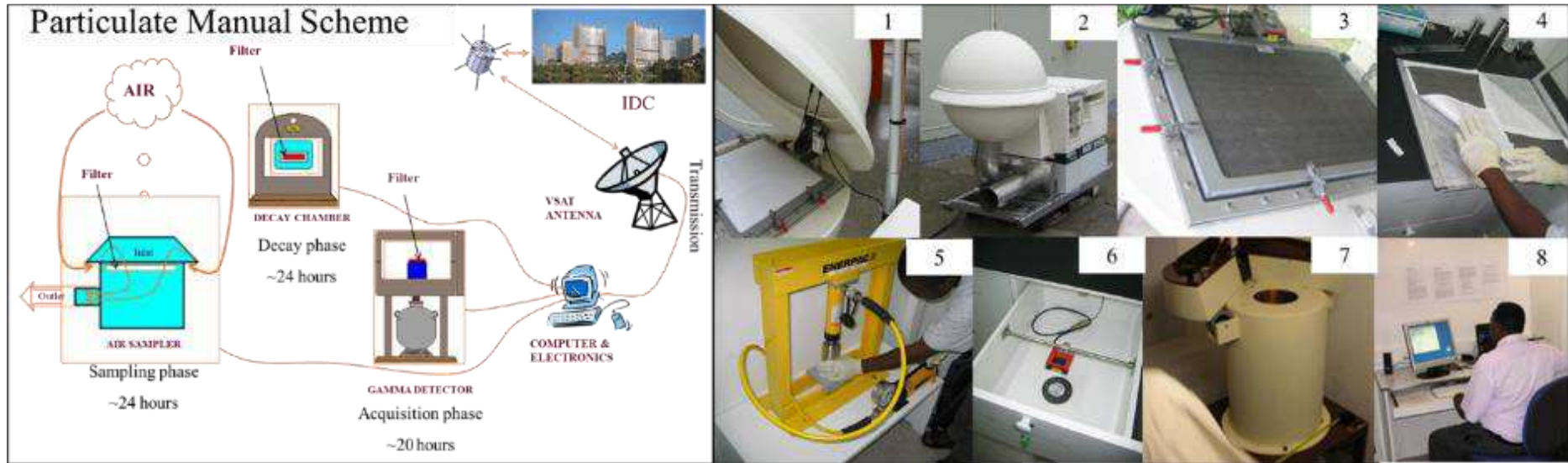
Figure 5: Particulate radionuclide station diagram. The right pictures show the steps followed at a typical particulate station: 1. Unexposed filter placed in the air sampler (white colour). 2. Filter in air sampler for sampling phase ~24 h. 3. Exposed filter (grey). 4 and 5. Filter folded and compressed into a 5 cm diameter disc. 6. Disc left ~24h for decay. 7. The filter is placed in the HPGe detector for counting phase ~20 h. 8. Sample pulse height data (SPHD) spectra analysis. (www.ctbto.org)

Figure 5 shows a simplified diagram of a particulate radionuclide station. The IMS radionuclide stations send their data via the Global Communication Infrastructure (GCI) to the International Data Centre (IDC). From there, they are automatically transmitted to the CTBT Member States.

Samples come from all stations currently in operation and they have been interactively reviewed for quality control.
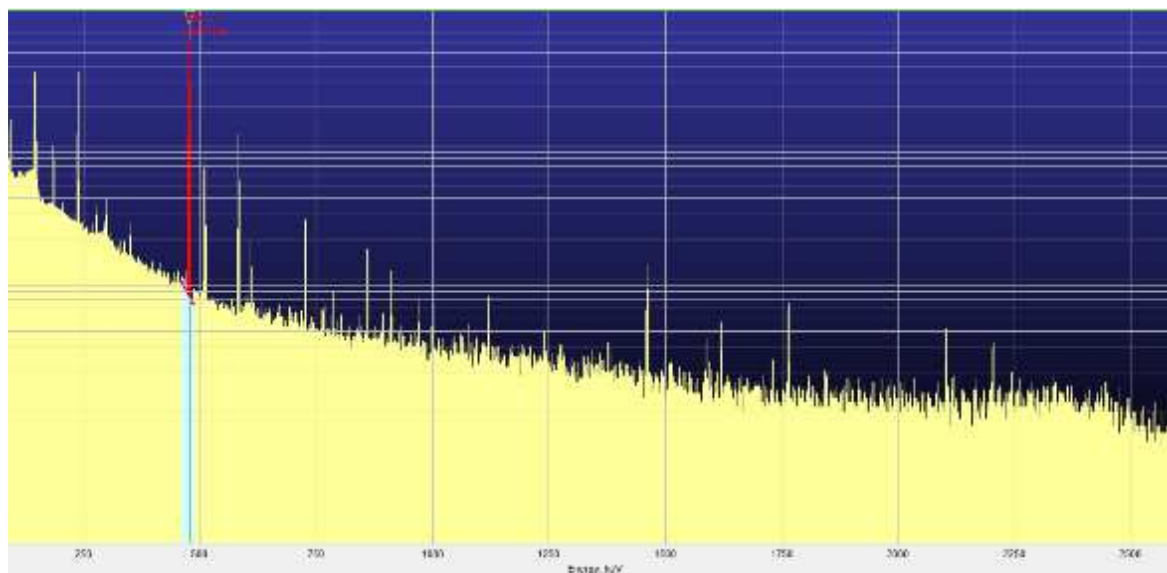

Figure 6. Sample pulse height data (SPHD) spectra analysis. Highlighted in red is the ^{7}Be peak (at 477 KeV).

1.5. Meteorological phenomena observed

For deciphering various meteorological processes on a large scale, the global network of IMS RN stations offers an unprecedented opportunity using ^{7}Be as aerosol tracer. In chapter three, it is demonstrated how the location and progression of the downward branch of the Hadley cell can be reconstructed with ^{7}Be data at any point in time on a global scale.

Time series of ^{7}Be activity concentrations can be interpreted as precipitation associated to monsoons and accordingly associated with Walker circulation patterns and ENSO.

A comprehensive list of meteorological phenomena has been analysed through the eyes of this radioisotope and are discussed in chapter two. A basic description of each process is presented below:

- Progression of Atmospheric circulation cells

In a simplistic model, each Hemisphere has three atmospheric cells: the tropical Hadley cell moving air to the equator at ground level, the Ferrel cell in the mid-latitudes and the Polar cell which moves air from the poles towards mid-latitudes. The driving cell for STE is the Hadley cell with its large-scale downward air flux at the interface between subtropics and mid latitudes around 30° N/S. The Ferrel cell, on the other hand, is an indirect, eddy type of circulation cell that transports air at upper levels from the pole towards the tropics, with prevailing westerly winds due to the rotation of the earth (Coriolis force).

Interface zones of these three cells are: Intertropical Convergence Zone (ITCZ), Hadley Ferrel Divergence Zone (HFDZ) and Polar Ferrel Convergence Zone (PFCZ) (Figure 7). There are two narrow, meandering bands of strong winds close to the tropopause, namely the polar jet at the PFCZ and the subtropical jet at the HFDZ. The movements of these jet streams, generally referred to as Rossby waves or planetary waves, are of major importance for the prevailing weather on a hemispheric scale.

While HFDZ features the downward branch of the Hadley cell marking the divergence of trade winds; the tropical and polar interface zones feature convergence and upward movements. The interface represents the STE area. The intertropical convergence zone circles the earth and marks the region where easterly[2] and westerly[3] winds converge. At ITCZ air masses move upwards, this means that ^{7}Be particle can only reach the ITCZ region by horizontal transport from higher latitudes and not through STE. The Hadley-Ferrel-Divergence Zone (HFDZ), on the other hand, exhibits the strongest STE, with a net downward flux of air, bringing ^{7}Be to the surface. HFDZ offers the clearest ^{7}Be signature thereby allowing the tracking of its position and latitudinal progression[16,18,35]. STE also occurs in connection with tropopause folds at the axis of the polar jet, affecting the mid-latitudes mainly in winter and spring, the time of the strongest frontal activity.

_____

[2] Easterly or trade winds are permanent east to west prevailing winds in the equatorial region, i.e. between 30°N and 30°S.
[3] Westerly or anti-trade winds are permanent west to east prevailing winds between 30° and 60°.
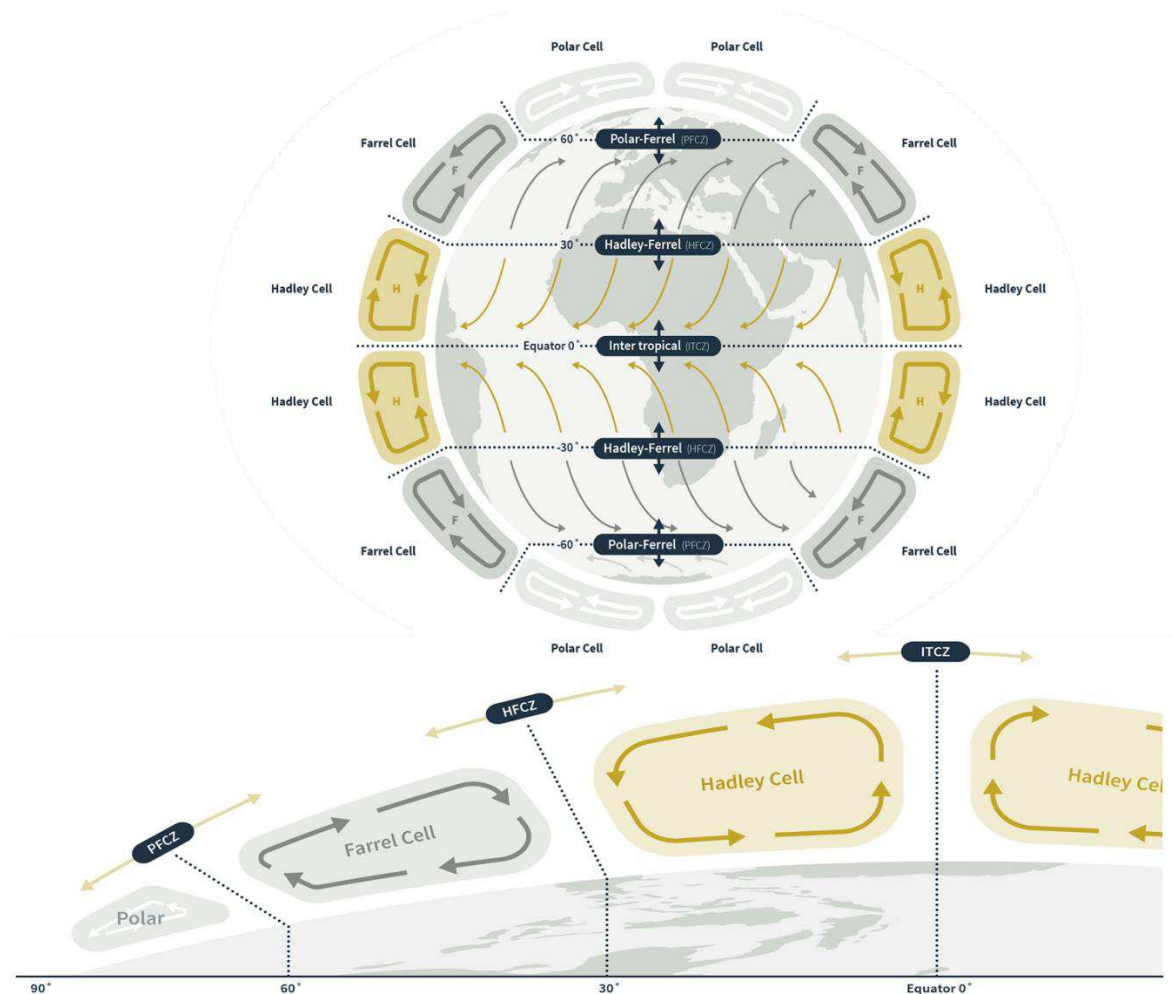
Figure 7 Hadley, Ferrel and Polar cells simplified structure. Black dotted lines mark the position of interface zones between atmospheric cells. (Terzi et al., 2017)

- Walker Circulations

The Walker circulation is the equatorial circulation which is observed on the surface as easterlies trade winds move warmed air towards the west. There are mainly north-easterly winds in the Northern and south-easterly winds in the Southern Hemisphere. This circulation is affected by El Niño Southern Oscillation[41].

- El Niño Southern Oscillation (ENSO)

El Niño Southern Oscillation is an irregular periodic variation in winds and sea surface temperatures over the tropical eastern Pacific Ocean. ENSO has two phases; one warming sea surface temperature called el Niño, and one cooling sea surface temperature called la Niña[109].

Official ENSO indicators are Southern Oscillation Index (SOI) and Oceanic Niño Index (ONI) which are defined as follow:

- o SOI is the difference between barometric readings at Darwin, Australia and Tahiti.

- o ONI is the average sea surface temperature in the Niño 3.4 region (between 120°W and 170°W) averaged over three months.

- **Quasi-biannual Oscillation (QBO)**

Quasi-biannual Oscillation is a quasiperiodic oscillation of the equatorial zonal wind between easterlies and westerlies in the tropical stratosphere with a mean period of 28 to 29 months[5].

- **Sudden Stratospheric Warming (SSW)**

Sudden Stratospheric Warming is an event in which the polar stratospheric temperature increases drastically over the course of a few days. It affects all layers of the atmosphere, changing the wind circulation patterns[58,75].

- **Solar Energy Particle (SEP) events**

Solar energetic particles are high-energy particles coming from the Sun and reaching near speed of light velocity. They are released during solar flares and produce an increase of cosmic rays penetrating the atmosphere[97,98,99].

- **Monsoons**

Monsoons are generally defined as a seasonal reversing trade wind accompanied by corresponding changes in precipitation.

Monsoons are governed by the periodic seasonal movement of the Intertropical Convergence Zone (ITCZ)[3,78,76,106]. They are associated with periods of frequent and intense precipitation, typically lasting a few months, preceded and followed by dry and stable weather conditions. They are linked to the trade winds, influenced by earth's rotation, axis and intense solar heating, and associated with deep convection in the equatorial region, which activates the Hadley circulation. Monsoon are in fact triggered by the progression of atmospheric cells interface zones. As air masses over land, compared to those over the sea, heat up faster with the beginning of summer, moist air first moves inland, which loses its water content while rising.

There are several geographically distributed monsoons. The South Asian monsoon season runs from June to September and affects the climate of most India and South Asia. Originally,

monsoon forecasts were based on statistical models of local variables such as temperature, pressure, wind and humidity. Today, most of the short-term monsoon predictions are based on numerical weather prediction or taking local meteorological parameters as indicators.

- Monsoon over Kerala (MOK)

The summer monsoon in Kerala, India is well researched and documented. Based on historical average, the Indian Meteorological Department (IMD) assigned the normal monsoon onset date to June 1st, and announces its onset forecast in the mid of May. Monsoon onset is defined by the IMD as change in rainfall, wind field, and Outgoing Longwave Radiation (OLR). Given that the monsoon onset moves in a time window of 25 days according to the IMD onset dates since 1980, the warning time currently provided is between 1–3 weeks with an error margin of ±5 days[54].

Monsoon in India is of particular importance for the $2 trillion economy, which is highly dependent on agriculture. Monsoon rains water two-thirds of India's harvest. However, the monsoon season also causes large-scale flooding, resulting in loss of human life and economic damage estimated around $7 billion annually[59,64].

- Tropopause height and jet streams

The tropopause is the thermogradient layer separating stratosphere and troposphere. From the surface up to the tropopause, temperature decreases with altitude, in the tropopause it remains constant and upwards it increases with altitude.

The tropopause is high in the tropics (15-20 km) and low at the poles (<10 km). It does not gradually decrease from equator to pole, but decreases drastically in the vicinity of the subtropical as well as the polar jet. Within tropopause folds close to the jet axis, STE is strongly allowing more ^{7}Be to be transported from upper tropopause regions to the surface. Delaygue et al. (2015)[8] describe the relationship between ^{7}Be and tropopause as the concentration of ^{7}Be augment as a function of altitude and latitudes (Figure 8).
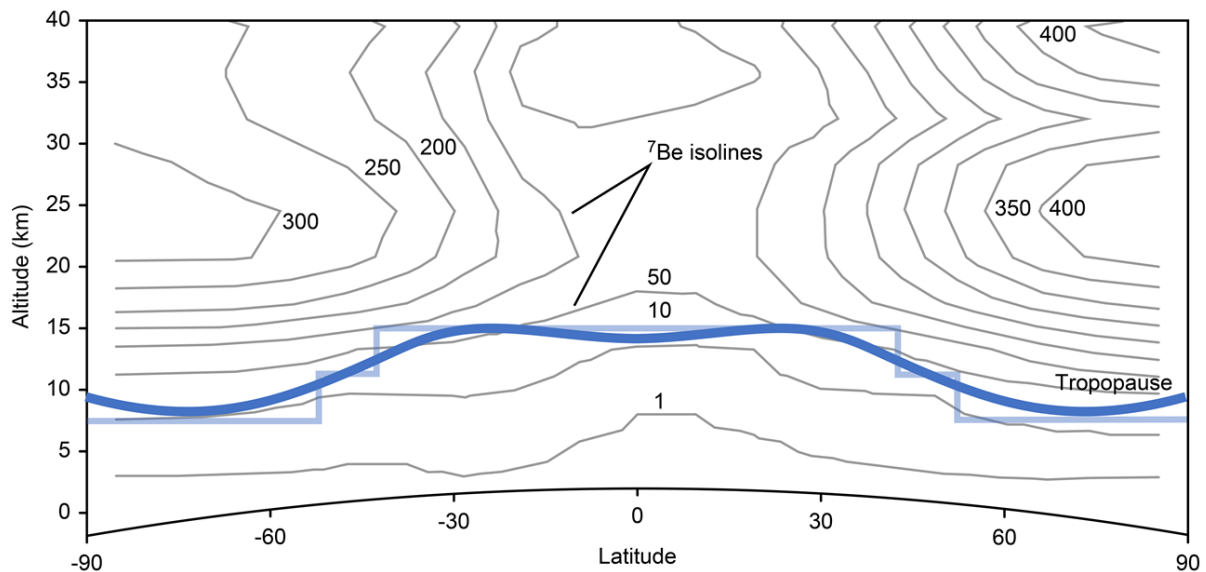
Figure 8. Beryllium-7 concentrations profile from Delaygue et al. (2015)[8] shows the relationship between tropopause height (blue line) and beryllium-7 concentrations, indicated by isolines[8].

Tropopause height variations or "breathing" indicate the inter annual and multi annual height variation of tropopause based on reanalysis data and GPS-RO data. Re-analysis data are a hybrid dataset, incorporating observations (including radiosondes, satellite data, and more) and filling in gaps in space and time around the globe using a weather model. GPS-RO data are retrieved temperature profiles generated by satellites.

The rapid growth of greenhouse gas concentrations in the atmosphere is expected to lead to significant changes in global atmospheric circulation patterns. Some of the changes under discussion are:

- Poleward movement of circulation patterns, meaning that the Hadley cell further extends towards the Pole in summer time[23,83,104].

- Stalling patterns (blocking) of the Rossby wave circulation. Atmospheric blocking is a phenomenon that leads to a static weather pattern lasting from one to several weeks, often associated with extreme weather events - heat waves in summer and cold waves in winter[86]. Frequently, the onset of a block starts with the rapid poleward transport of subtropical air. Weather and climate models have a tendency to underpredict blocks and to underestimate their duration. It is so far not well established whether blocks are becoming more or less frequent under global warming conditions, although regional increases in blocking conditions have been identified.

- Multi-annual variation of the troposphere and global tropopause heightening at mid-latitudes. The tropopause layer is controlled by complex atmospheric dynamics with different frequency cycles that range from sub-seasonal to year-to-year and multi-year variations. The resulting effect is a breathing of the tropopause height (fluctuations from lower to higher altitude)[24]. What has been observed in this work is an overall positive trend, meaning that the average tropopause height has increased in altitude over the past 20 years.

The expected changes in global circulation triggered by global warming, mainly caused by the high CO_2 emissions, and the resulting effects on ^7Be concentrations[93] is described by a simplified diagram in Figure 9. This is further discussed in Chapter 3.
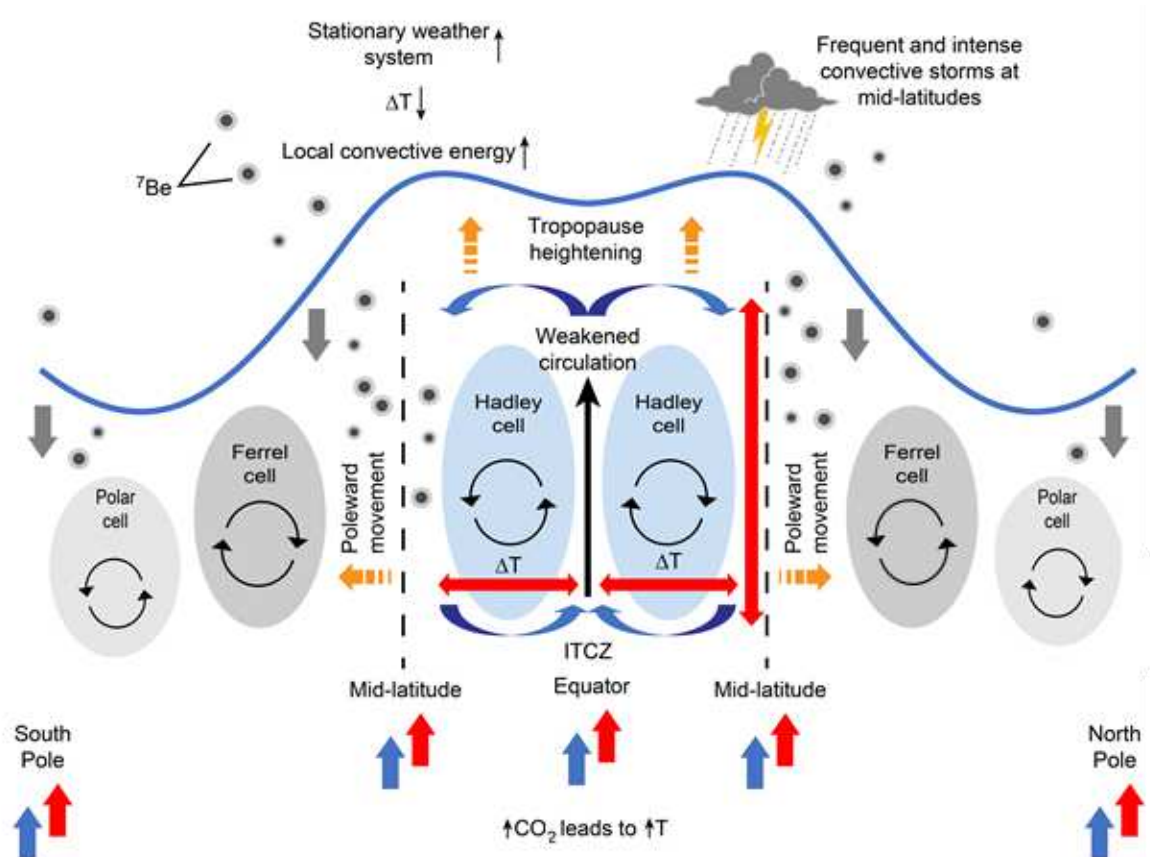

Figure 9. CO_2 emission leads to temperature increase producing tropopause heightening, poleward movement of the Hadley cell and weakening of the general circulation. The slowing down of the atmospheric circulation at mid latitude is expressed through blocking of jet stream, which produces stalling weather systems. Stalling weather systems are associated with increased local convective energy produce not only extended summer periods and droughts but also a higher frequency of extreme weather events such as floods and hailstorms[93]. (Terzi et al, 2020)

Chapter 2

Methods

Beryllium-7 data are recorded as daily activity concentration values in µBq/m³. Out of 70 operating IMS stations 62 stations presented times series longer than 7 years. In total, approximately 270,000 radionuclide samples were selected. Most of the samples analysed contained between 1000 and 9500 µBq/m³ of ^{7}Be.

Time series of the continuous monitoring of cosmogenic ^{7}Be at IMS stations show in the long-term a regular annual cycle, but with significant daily and weekly fluctuations that amount to a factor of two or more. There are multiple causes for the variability of ^{7}Be activity concentrations in ground-level air[6,7,34,37,76,111]. Time series were post-processed with different moving averages to smooth out these variations and further normalized.

- Mean and normalization are calculated on the base of equation 1.1 and 1.2. Where $\mathbf{x^i}$ is the ^{7}Be activity concentration recorded each day [µBq/m³]. N is the number of days for which the mean is calculated: 0/-15 and 0/-30 days average for seasonal analysis, 0/-120 days average to study multi-annual variations such as tropopause breathing and atmospheric blocking. M is the calculated mean. $\mathbf{\bar{x}}$ is the overall averaged activity concentration of ^{7}Be [µBq/m³] measured at each location: 2003-2019 for all listed IMS Station. N(M) is the calculated normalized mean.

Equation 1. (1.1) Mean calculation and (1.2) normalized mean calculation.

1.1 $\mathbf{M = \frac{1}{n} * \sum_{i=1}^{n} x^i}$

1.2 $\mathbf{N(M)} = \frac{1}{\bar{x}} * \frac{1}{n} * \sum_{i=1}^{n} x^i$

- Normalisation has been calculated by dividing the mean by the overall average of the timeseries. Normalised values are helpful to highlight the changes of [7]Be trends over time and to compare [7]Be trends at different locations that present strong differences in activity concentrations. It is the case that high latitude stations may have a level of concentration by a factor of two higher than station at lower latitudes. No postprocessing (raw [7]Be timeseries) was applied to analysed SEP events, since for these events the raw data are required to be able to see expected spikes which would otherwise be flattened out through short- or long-term averages.

- Correlation coefficient presented throughout this study are based on the Pearson correlation coefficient (PCC). PCC measures linear correlation between two variables X and Y. It has a value between $+1$ and -1, where 1 is total positive linear correlation, 0 is no linear correlation, and -1 is total negative linear correlation.

2.1. Latitudinal and equatorial bands

For the better reconstruction of atmospheric cells movement monthly mean of [7]Be (μBq/m³) time series have been divided into clusters based on their IMS station coordinates.

Monthly averages are built on the daily averaged activity concentrations in order to smooth short-term fluctuations. The 12 monthly data points are used to compare the seasonal variation for stations with a common longitude (Figure 10). Since similar patterns were found especially for latitudes between 10° and 50° in both hemispheres, the time series from two stations with different latitude and similar longitude are compared to see the pattern shift.

In a second stage, monthly averaged values per longitudinal bands are displayed, showing [7]Be activity concentrations from the most north-eastern station to the most southern one, using all stations located within a small longitudinal range. By doing this it is possible to view, through a [7]Be map of that specific longitude range, the main atmospheric convergence zones (Figure 11).

The shift represents the progression of atmospheric cells convergence zones: ITCZ, HFDZ or PFCZ.

Using monthly average values, over all available years has two positive factors: it simplifies the data analysis and smoothens the wash out effect as it happens at different times each year.
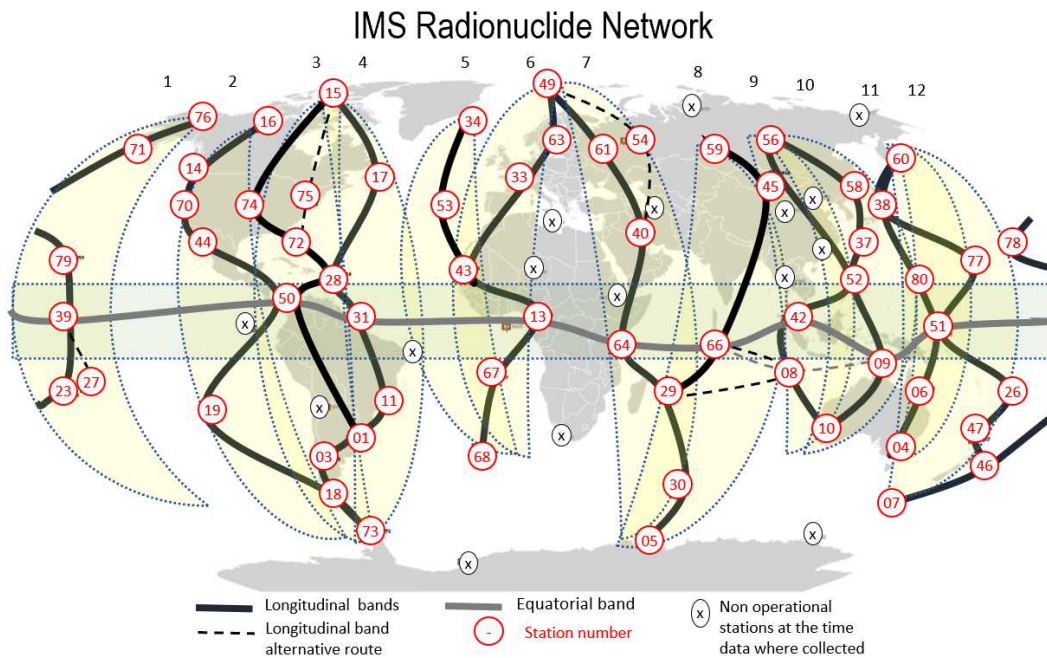

Figure 10. IMS radionuclide network divided into 12 Longitudinal bands and 1 Equatorial band. (Terzi et al., 2019)

Figure 10 shows the RN network divided into 12 longitudinal bands and 1 equatorial band, a description of each IMS stations and bands can be found in Table 1.

The yellow areas in Figure 10 are drawn only to indicate the approximate length and width covered by each band. Black lines connect the stations which represent the bands. The most northern and most southern stations are commonly used for two neighbouring bands as the longer the band the easier it is to see convergence zones. Dashed lines are alternative routes to the chosen band. The reason those stations have been left out is because they are parallel to stations with similar longitude and latitude and with similar dataset.

The signature of the ITCZ, HFDZ and PFCZ (Figure 11) is produced using more than a decade of [7]Be activity concentrations measured. These three structures are visible all around the globe using the surface coverage of [7]Be observations, see paragraph 3.1.
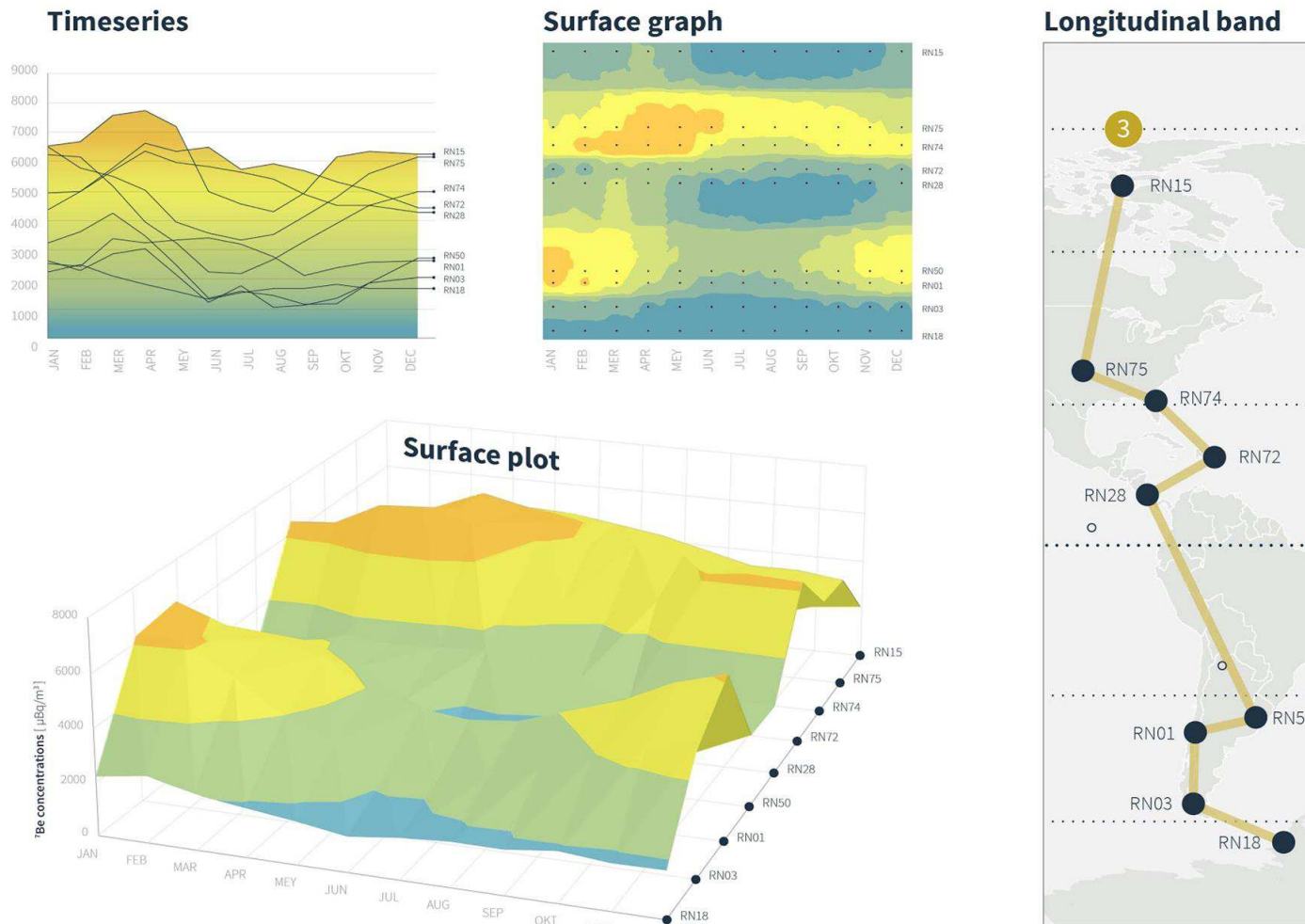
Figure 11. Example of convergence zone reconstruction through ^{7}Be time series. Hadley cells are marked in yellow-orange. ITCZ and Polar Ferrel cells are marked in light blue. Time series are pivoted into surface charts to visually display the atmospheric structures. On the right, the longitudinal band shows which station has been utilized for the selected area. (Terzi et al., 2017)

For the equatorial band (Figure 12), similar equatorial latitude stations have been chosen along all longitudes in order to study the signature of the Walker circulation and ENSO patterns in ⁷Be observations. After successful reconstruction of the interface zones in each band, the whole dataset was aggregated to visualize the global ⁷Be concentration structure in the third stage of this study.
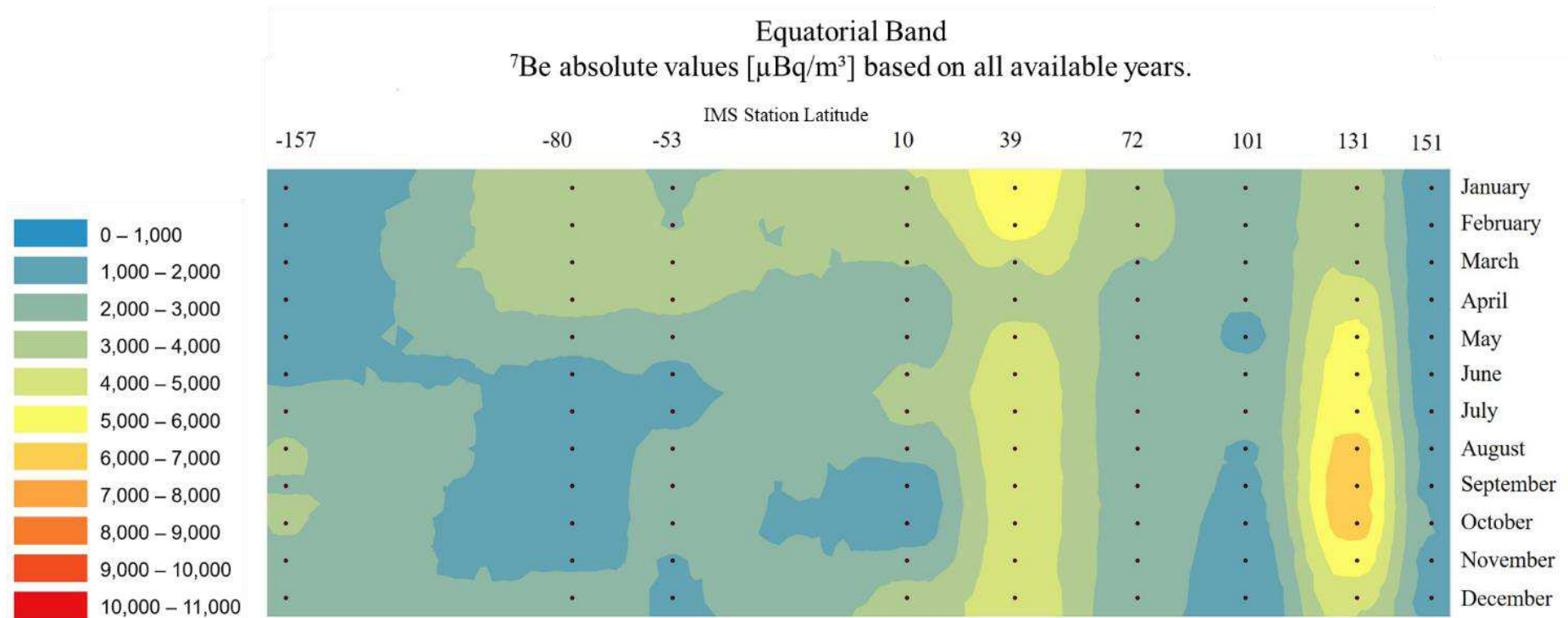

Figure 12. Equatorial band. (Terzi and Kalinowski, 2017)

2.2. Beryllium-7 interpolation maps

To study the global dataset in a systematic way, the average values of each station are redistributed into a global grid (sample shown in Figure 13). Grey grid points, in Figure 13a and b, are non-operational stations at the time of this study and whose data were not available. Black grid points are operational stations whose data have been used in the analysis.

Each grid displays the position of convergence zones based on ^{7}Be concentrations worldwide during a specific month, a rather constant pattern that repeats each month with small modulations.

To highlight the difference between each modulation at a given month, Figure 13b and d, are showing the normalized values at each grid point. The normalized ^{7}Be concentrations are calculated by dividing the monthly average concentrations by the average over all months for each station site. The latter can be found in Table 10. By comparing monthly grids, it is possible to follow the convergence zone progression with time, i.e. the impact of the convergence zones moving north and south.

The plots and maps of the absolute and normalized ^{7}Be concentrations shown in Figure 13 use two different types of interpolation.

Figure 13a and b interpolations are based on the Inverse Distance Weighting method. For each interpolated point the weighting is based on the inverse of the distance to neighbouring data points. The values for points between IMS stations are calculated with a monthly weighted average of the available data. Figure 13c and d plots are interpolated using a multilevel b-spline function which provides smoother boundary effect.
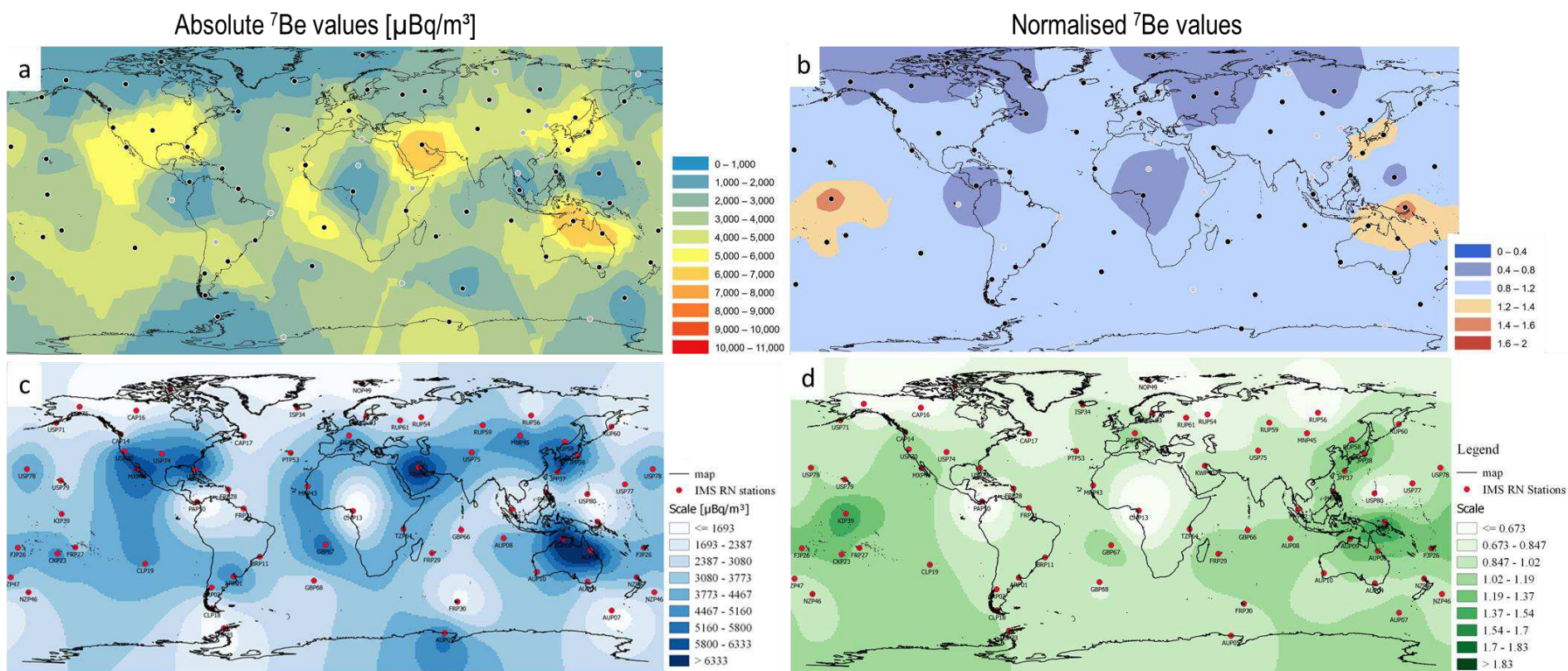
Figure 13. Global ⁷Be interpolation maps based on monthly averages data of ⁷Be for the month of October. On the left (a and c) absolute values, on the right (b and d) normalized values. The top charts (a and b) interpolation is built on Inverse Distance Weighting method. Lower charts (c and d) interpolation is based on Multilevel b-spline function. (Terzi and Kalinowski, 2017)

2.3. 3D surface concentrations of ^{7}Be

Changes in atmospheric circulation dynamics such as the tropopause breathing and the blocking of jet stream are studied through a multi-year analysis of long term ^{7}Be averaged data.

In a first step ^{7}Be daily activity concentrations are transformed into normalized long term (0/-120 days) averages (equation1.1 and 1.2).

In a second step the timeseries are plotted into surface charts (Figure 14) to highlight:

o   Growth of ^{7}Be concentration over the last 15 years.
o   Extended periods of ^{7}Be growth over the summer months over the past 15 years.

Figure 14 shows the transition from line chart to surface with different prospectives.

Figure 14 (middle plot) presents the 3D surface charts where a value of 1 indicate the average over all years. Any value above 1 is considered growth. In the right plot the attention goes to the number of days when the levels of ^{7}Be above 1 (growth) increase over the years.

To study the correlation between tropopause trend and ^{7}Be Figure 15 (right plot) shows a surface chart built on ^{7}Be post-processed data of all available stations in latitude order. The left plot presents the tropopause profile based on reanalysis data (grey-red dotted line) and the profile of ^{7}Be growth measured in 2017 (compared to the overall average) built on stations located along the Canada-Antarctica axis.
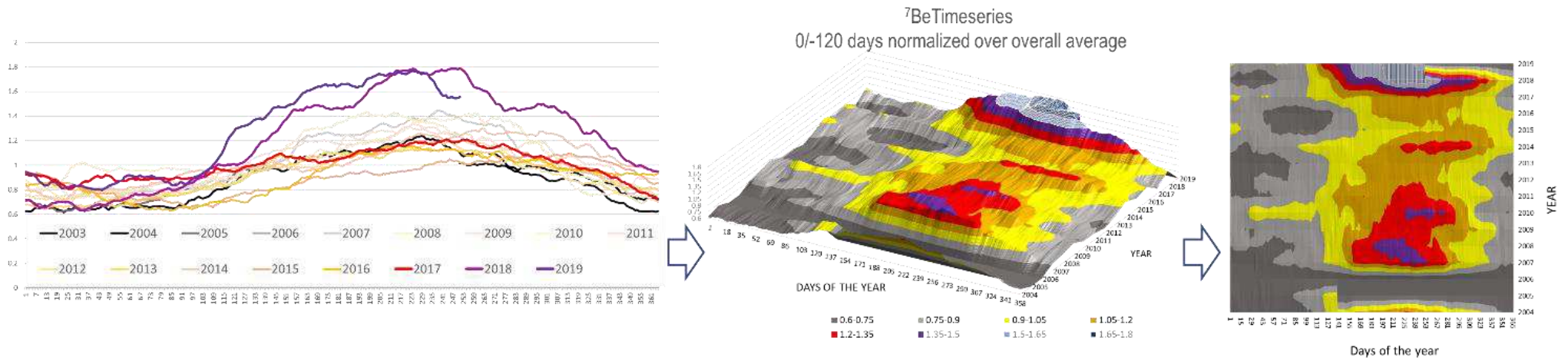
Figure 14. SEP63 (Sweden) trend of ⁷Be timeseries post processed with 0/-120 days average and normalized over all available years presented as line chart (left), 3D surface (middle) and 3D surface bird view or contour chart(right).
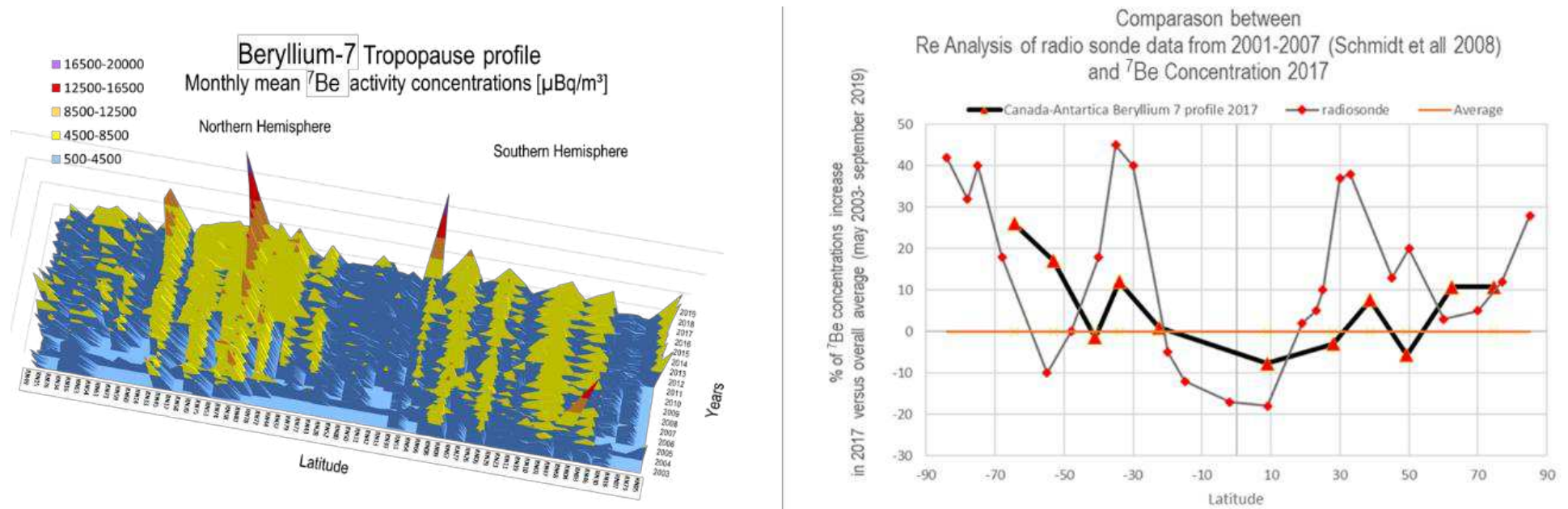
Figure 15. On the left plot, [7]Be timeseries from all IMS stations displayed in a surface chart in order of latitude. On the right plot, tropopause profile based on reanalysis data (2001-2007) compared to [7]Be growth measured in 2017 (% of growth versus overall average) from stations located between Canada and Antarctica. (Terzi et al., 2020)

2.4. Trans-equatorial approach

The trans-equatorial approach is based on the use of averaged ^{7}Be timeseries from two locations that are positioned on opposite sides of the equator to forecast the onset and withdrawal of the world's monsoons.

There is an indirect link between monsoon and ^{7}Be:

- The seasonal variations of the Hadley circulation due to the tilt of the earth's axis are the driving force for the world's monsoons.
- ^{7}Be concentration time series can be used to track the position of the downward branch of the Hadley cell which triggers the monsoon.

Thereby a hypothesis can be made that monsoon onsets and withdrawals can be forecasted with ^{7}Be, depending on whether the cell progresses earlier or later which is visible in the data sets. To explain the origin of the transequatorial approach a more detailed explanation of the Indian monsoon is needed.

The Indian monsoon is part of the global monsoon system[44]. Prior to monsoon onset, humidity (H) and temperature (T) cross a critical threshold in two specific regions, Eastern Ghats (EG) and North Pakistan (NP). These geographic locations are tipping elements of the monsoon. Occurrences of critical threshold conditions in term of H and T allows adjustment in prediction of monsoon for abnormal years often associated with ENSO. A few days before the monsoon onset, the relative H increases abruptly and T drops at EG crossing NP T line[82]. Monsoon withdrawal is caused by southward movement of the ITCZ via displacement of moist with dry air, anticyclonic flow, and rainfall reduction. In Stoblova's work[82] regions are used to predict onset and withdrawal of the monsoon based on time series analysis of near-surface air temperature and relative humidity.

Stolbova et al. (2016) [82] propose a new method for forecasting onset and withdrawal of monsoon suggesting the use of relative humidity and temperature thresholds. The indirect link between monsoon and ^{7}Be provided the basis to test Stoblova's work in terms of ^{7}Be thresholds[93].

Historically, several methods have been applied to study the monsoon phenomena. These methods are usually based on different indicators or a combination of indicators such as precipitation, moisture, and winds transition[20,62,82,85,87,101,103,105].

The trans-equatorial approach looks at the seasonality of ^{7}Be concentrations along the high-pressure ridge, also called subtropical high belt. It is continuous in both hemispheres and is the result of the subtropical jet stream formed by the HFDZ[50]. All stations located under this high-pressure ridge can be used for determination and prediction of the monsoon tipping point.

In a preliminary phase the research focused on whether ^{7}Be thresholds are found for different paired locations that are affected by Indian monsoon such as the IMS station MYP42 and JPP37 (Figure 16).

For MYP42 and JPP37 the seasonal pattern is constant for the past 4 years. At MYP42 ITCZ is approaching end of April and leaving towards September. For JPP37 the ITCZ is approaching end of May and moving away end of August. MYP42 has lower activity values and seasonal variation probably due to its closer location in respect to ITCZ. One can see two distinguished crossed points: first, JPP37 has a major drop in values at the end of May where the levels of concentration reach towards MYP42, this could indicate an ITCZ positioned right between the two stations. Second, the concentration levels depart from each other in a second phase around end of August meaning the ITCZ is reaching its furthest point from JPP37 and getting closer and closer to MYP42. Heavy rains in JPP37 region start in August (www.monsoon.yale.edu). The drop of ^{7}Be levels appears about 30 days prior to the monsoon onset, this may indicate the possibility to use cross points (i.e. where levels of ^{7}Be are equal) as new monsoon-indicating threshold. Rather than considering the increase of ^{7}Be concentration at JPP37 alone, cross points indicate the position of an atmospheric cell relative to two locations giving more guarantee that the time window delimited by the cross point is indeed monsoon related.
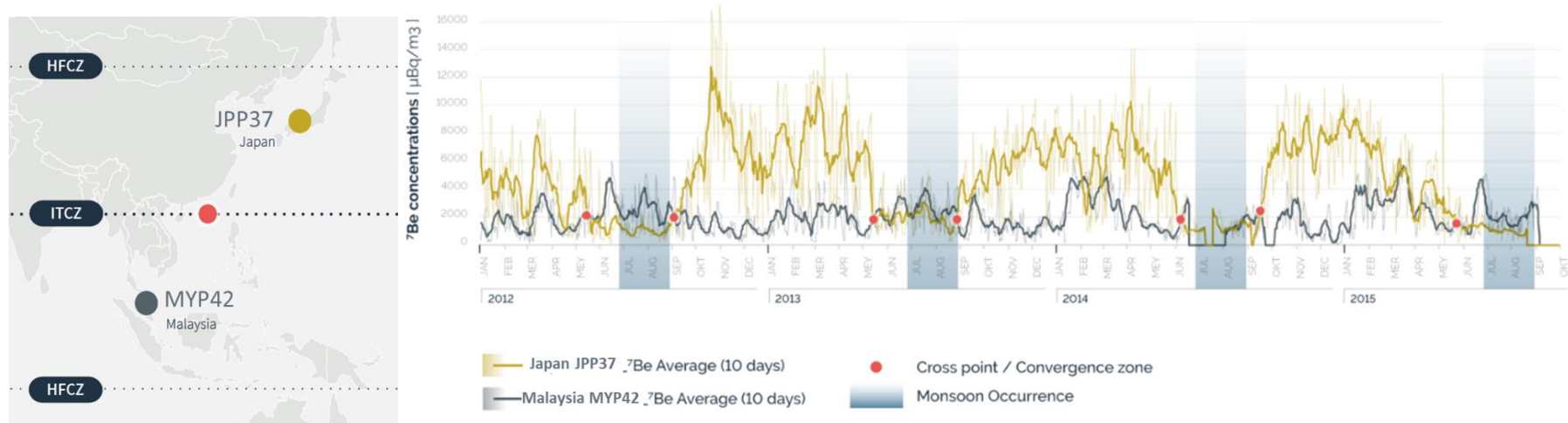
Figure 16. Averaged daily activity of ⁷Be (µBq/m³) from 2012 to 2015 for MYP42 and JPP37. Only four years are displayed for clarity, all years can be viewed in the supplementary file. Red dots indicate the approximate position of the crossing points. Blue-grey area indicates the approximate monsoon onset window. (Terzi et al., 2017)

The trans-equatorial approach applied to the Indian monsoon case study (chapter three) involves a station in Russia, Dubna (RUP61) and a station in Australia, Melbourne (AUP04):

Every time the trendlines of the Russian and Australian stations (RUP61 and AUP04) cross each other, that particular date is referred to as a cross point (Figure 17). There are two cross points per year: CP1 in early spring and CP2 in late summer. The number of days from CP1 to the monsoon onset is the forecast lead-time (alias the monsoon onset warning time). By averaging the onset warning time from CP1 over the past 10 years, an almost constant alerting time for the monsoon onset of 52 ± 3 days is achieved. After the monsoon onset date has passed, the second cross point (CP2) occurs between the two stations on average 42 ± 7 days before the monsoon withdrawal date, representing the monsoon withdrawal lead time. All cross points are correlated with monsoon onset and withdrawal times because the seasonal movement of the Hadley-Ferrel-Divergence Zone (northward and southward) is coherent with the Hadley circulation, which drives the monsoons in and out of India.

Furthermore, CP2 is on average 8.7 months before the monsoon onset of the following year. There is a weak correlation (PCC 0.37) between CP2 and monsoon onset the next year, indicating a certain dependence between the southward regression of Hadley-Ferrel cell (pushing the monsoon away from the Indian Peninsula) and the return of the Hadley-Ferrel cell the following year (which drives the arrival of the monsoon).

The average lag time between cross points and monsoon onset and withdrawal is built through a ^{7}Be multi-year average of RUP61 (Dubna, Russia) and AUP04 (Melbourne, Australia) (Figure 18).
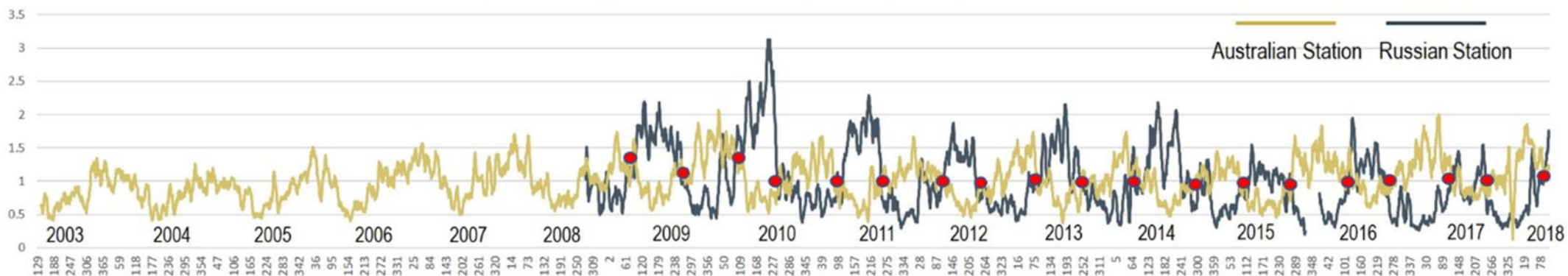
Figure 17. [7]**Be timeseries from Dubna Russia (blue line) and Melbourne, Australia (yellow line). The red dots mark the cross points (CP) between the two locations. (Terzi et al., 2019)**
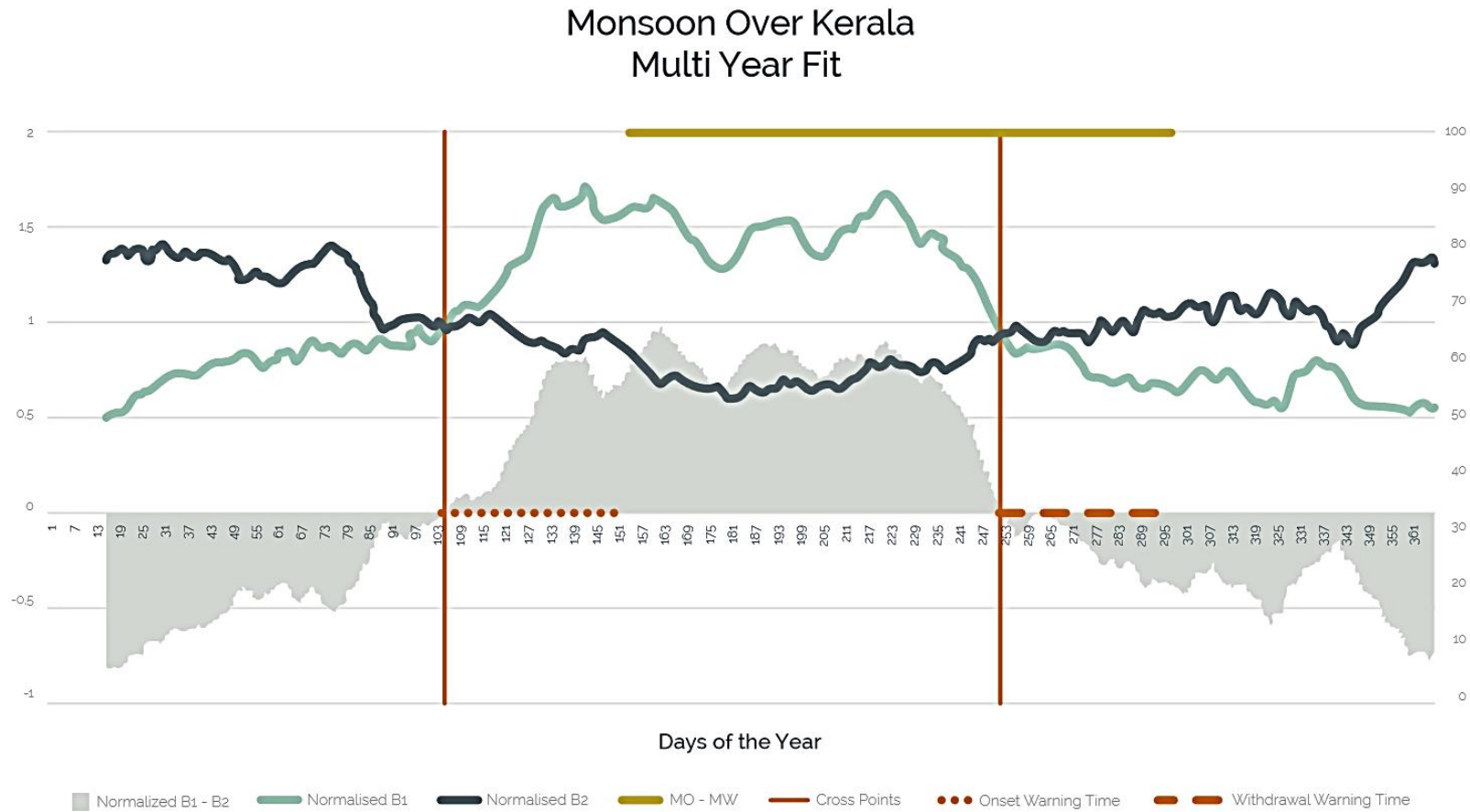
Figure 18. 15 day running average of the [7]Be activity concentrations for the 2009 to 2018 period. [7]Be [µBq/m³] time series from Russian (B1 – light green line) and Australian (B2- dark blue line) stations (RUP61 and AUP04) are averaged using 0/-15-day average and normalized with the overall average value of each time series. Cross points 1 (method B) and cross point 2 (method E) are marked with red bars, their provided warning times on onset (52 days) and withdrawal (42 days) are marked with red dotted lines. Monsoon period is shown with yellow bar on top of the chart. Onset and withdrawal dates of monsoon over Kerala are retrieved by the Indian Meteorological Institute. (Terzi et al., 2019)

Chapter 3

Results and Discussion

The analysis of ^{7}Be timeseries demonstrates that the seasonal movement of atmospheric cells is visible in the data (Figure 19). Data from the global IMS network can therefore be used to study large-scale atmospheric circulation.

Figure 19a shows the seasonal ^{7}Be variations at AUP09 in Darwin, Australia and PHP52 in Tanay, Philippines. AUP09 has 12.43° S latitude, 130.89° E longitude, PHP52 has 14.58° N latitude, 121.37° E longitude. Both stations are in South East Asia and strongly affected by the monsoon season. Beryllium-7 flux patterns exhibit a 6 months' shift between Darwin and Tanay as the two stations are located within similar longitude but with latitude on either side of the ITCZ. Kusmierczyk-Michulec et al. (2015)[37] demonstrate that in part depletion in ^{7}Be concentration is attributed to the wet deposition which happens to be very intense within the ITCZ. Figure 19a and b present a clear annual cycle of minima and maxima, which is modulated by shorter fluctuations which are already significantly smoothened by aggregation to monthly averages. The short-term fluctuations can mainly be explained by episodes of heavy rain and are a confirmation of the impact of wet deposition. The minima and maxima with an annual cycle correlate with movements of the ITCZ and HFDZ. The correlation between activity concentration and the wash-out effect is visible and in this case is especially predominant during monsoon season. The yearly trend is also displaying a slow variation of the value reached by the annual maxima which is associated with the 11-year solar cycle, here marked with yellow dots (Figure 19.b) representing the number of monitored sun spots (www.sidc.be).
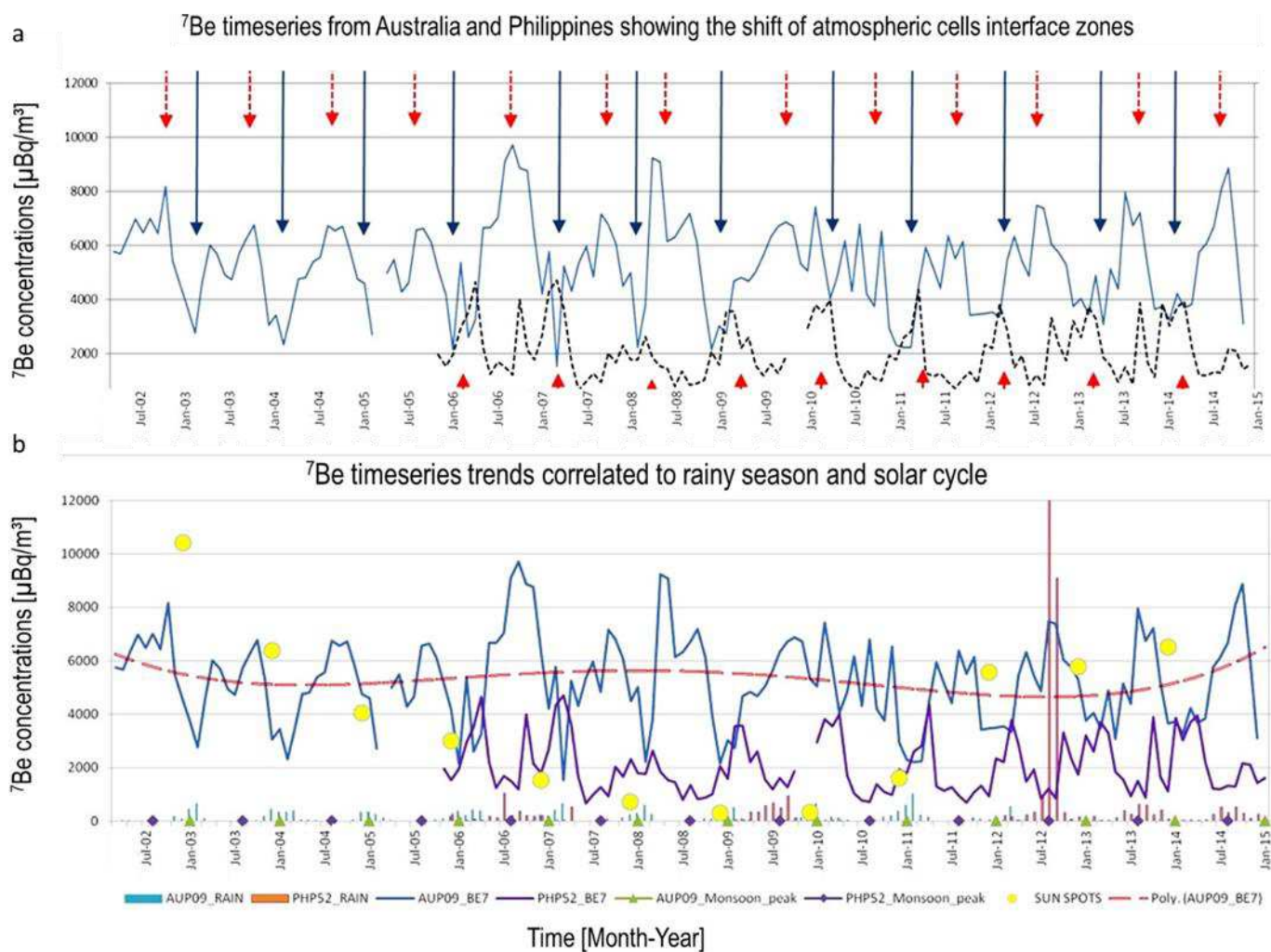
Figure 19a. AUP09 in Darwin, Australia (blue solid line) and PHP52 in Tanay, Philippines (black dashed line) time series of ⁷Be concentrations (µBq/m³) showing the shift between minima and maxima which represent the transition of ITCZ (blue arrows) and HFDZ (red arrows).

Figure 19b. ⁷Be time series for AUP09 shown as blue upper curve and PHP52 as magenta lower curve. Data are averaged per months, null and negative values, spikes are filtered out. Rain measurements (green and red bar series) come from meteorological data collected at IMS stations. Monsoon peaks (green triangles and purple diamonds) are shown as reference, for AUP09 and PHP52 regions the monsoons usually peak in August and January respectively (www.monsoon.yale.edu). Polynomial trend of AUP09 ⁷Be concentrations (red dotted line) is shown in reference to the sun spot number (www.sidc.be) highlighting the inverse correlation between lower number of sun spots and higher ⁷Be. Activity concentrations measured in µBq/m³. (Terzi and Kalinowski, 2017)

3.1. Seasonal movement of Atmospheric cells

Figure 20 presents the resulting concentrations as they change over time (lower plot) for each longitudinal band (indicated in the upper plot with a red line connecting the stations and a red box around the number of the band). Table 8 shows the data used to produce each band plot.

The position of the Headley cell and the associated HFDZ can be well seen by the concentration minima (blue-green) and maxima (orange-red). It should be noted that absolute minima and maxima are likely not observed due to the limited density of the network. This, however, does not impact the analysis as any minima or maxima moving north or south with the season will cross the IMS sites at one point in time and will therefore not be missed. Moreover, the higher density of operational stations in the northern hemisphere needs to be taken into account.

In order to show how the north-south movement of the convergence zones imprint their signature on these kinds of ^{7}Be concentration plots, a theoretical model is shown in longitudinal alignment with the concentration plot of one longitudinal band in Figure 21.
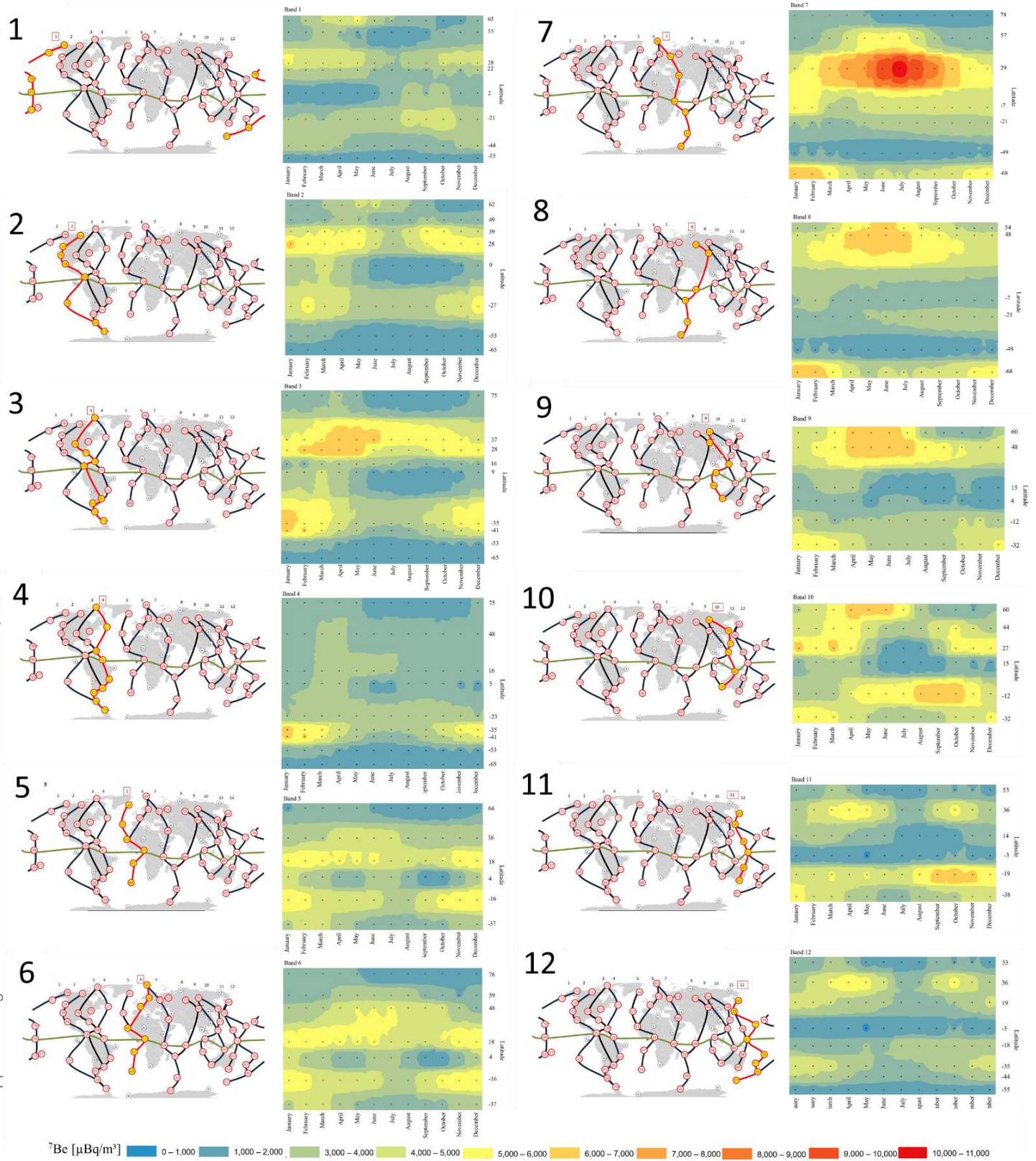
Figure 20. Monthly averages of ^{7}Be concentrations [μBq/m³] displayed next to each respective longitudinal band. X and Y axis display months and latitude respectively. (Terzi and Kalinowski, 2017)
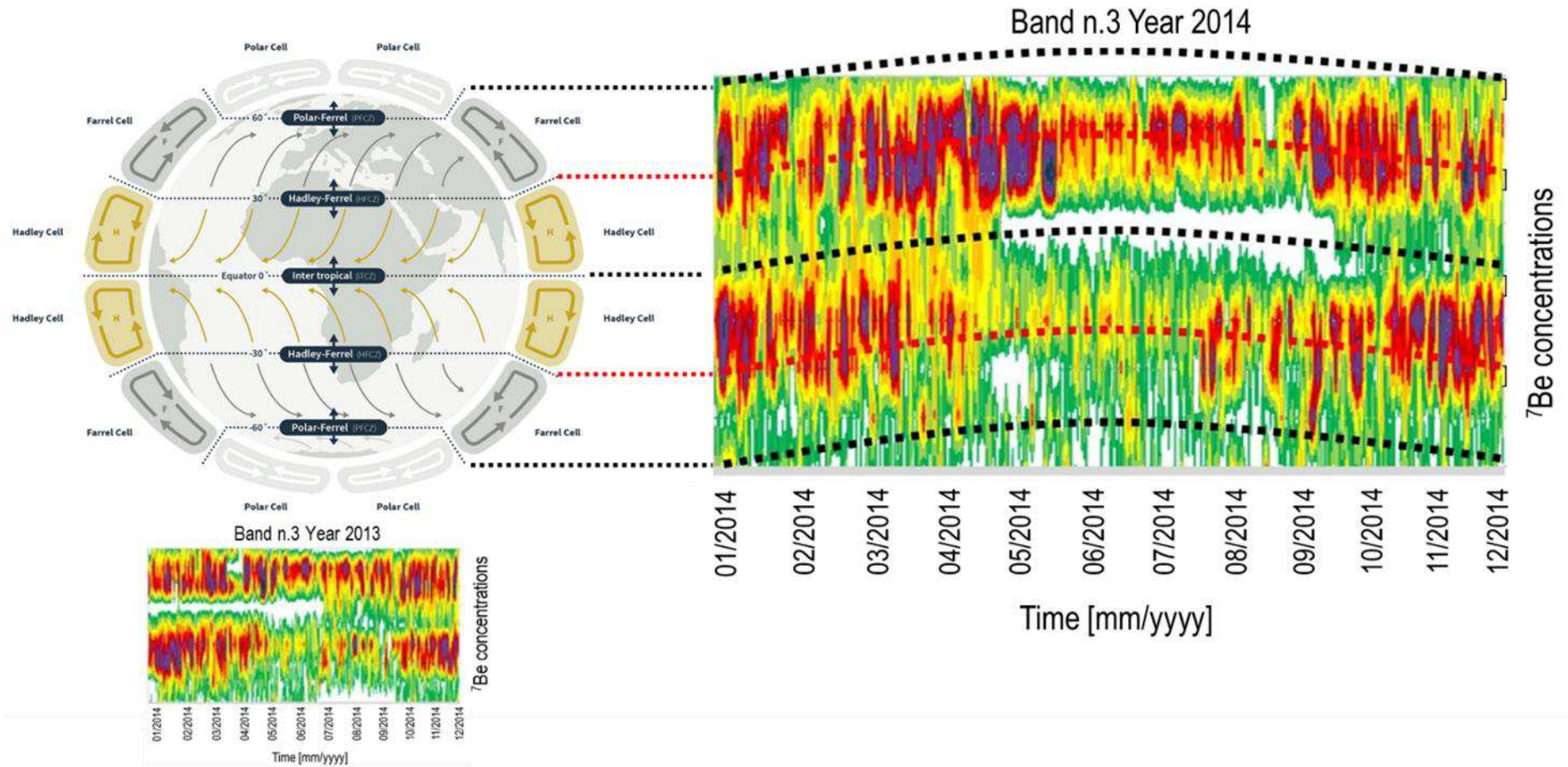
Figure 21. Theoretical model of atmospheric cells and convergence zones with dynamic pattern structures of band 3 for the year 2014. Interface zones line follow a "Bow" Structures, these are marked by dotted lines. (Terzi and Kalinowski, 2017)

Based on Figure 20 and Figure 21, the following observations can be made.

- The output based on ^{7}Be activity concentrations confirms the theoretical model (Figure 21) with two maximum concentration lines related to the HFDZ (northern and southern hemisphere) alternated by three minimum concentration lines related to one ITCZ and two PFCZ (northern and southern hemisphere).

- The ITCZ is most pronounced not only because of the absence of vertical down-mixing from the stratosphere but also due to the intensified wet deposition. All signatures of ^{7}Be relative to the atmospheric cell interface zones follow an "arch" or "bow" like structures as expected given the northward and southward progression of the Hadley cells over the course of one year.

- "Bow" structures at equatorial latitudes are also clearly visible in bands 3, 5, 6, 10 (Figure 20) and may be due to progression of ITCZ and to wash out effect. Longitudinal band 10 present a very strong change in northern hemisphere over time with red levels moving high up in summer and lower in winter giving the "Bow" shape.

- Band 2 (Figure 20) shows a straight line at low latitudes possibly indicating weak longitudinal circulation, but more likely due to the large spacing between stations (the next north at 16° degrees distance, next south at 26° degrees).

- Band 3 (Figure 20) has a clear arched structure which can be used to possibly interpolate cell progression speed. If one divides the distance of USP74 (latitude 37.1°, longitude -99.7°) and USP72 (latitude 28.1°, longitude -80.6°) by the time it takes the highest ^{7}Be concentration (purple) to go from USP74 to USP72 it is possible to interpolate an approximate average speed of 2.8 km/h for the northward movement of ITCZ or regression of HFDZ. The average speed of the HFDC progression is calculated based on a monthly average over all available years.

- Bows at polar latitudes are mainly shown in band 3 and 12 marking the arrival of the PFCZ.

- Highest values are present in band 3 and 7. ^{7}Be levels reached by the station in Kuwait confirms the fact that this region in the world has the highest surface concentrations of ^{7}Be[4].

- Lowest concentrations are seen in band 1, northern hemisphere (NH) of band 4 and band 12 which are areas highly exposed to precipitation. The NH of band 4 may be blind to maxima due to the locations of stations. The northern hemisphere in fact, shows

higher activity except for band 4 and 11 which may be due to the distribution of the RN network.

- Band 5 and 6 (Figure 20) are similar as they share 3 stations, CMP13 to mark ITCZ, GBP67 for HFDZ and GBP68 for PFCZ.

- Part of band 5 consists of GBP67 and GBP68 with latitude of -16° and -37° respectively. These two stations together with GBP66 (part of band 9) are hosted by the United Kingdom and their ^{7}Be concentrations values have been analysed in a study by Burnett and Davies (2014)[10] to provide information on ^{7}Be distribution. According to these authors, GBP67 has the highest calculated ^{7}Be concentrations, while they are lowest in GBP66. These findings correlate well with latitude positions and elevation and match the levels shown in band 5 and 9. GBP67 enhanced sampling has a windier and exposed condition whereas GBP66 is found in a low latitude position where stratospheric influx of ^{7}Be into the troposphere is lower (Figure 22).
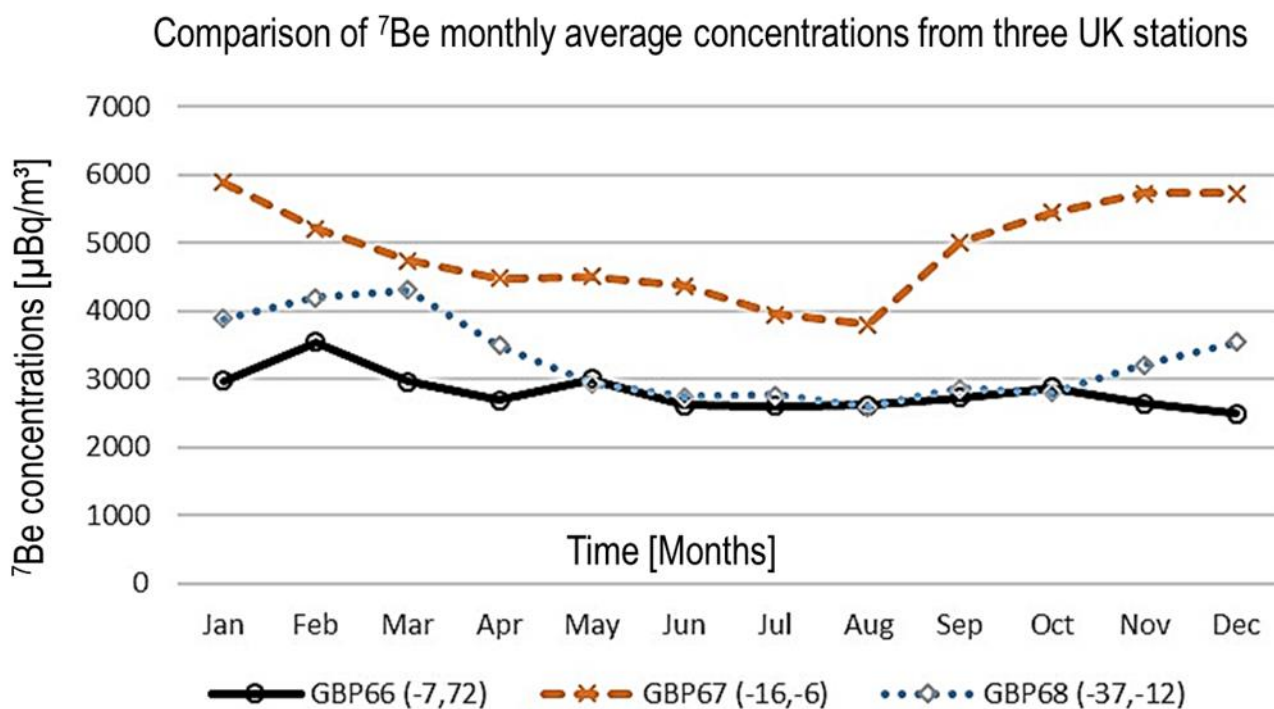
Figure 22. Monthly averaged (µBq/m³) trend recorded at Biot/Chagos Archipelago (GBP66), St. Helena (GBP67) and Tristan da Cunha (GBP68). The geographical setting of GBP67 has a remarkable effect on ^{7}Be levels detected. (Terzi and Kalinowski, 2017)

Unusual concentrations are found in band 1 northeast latitude, USP76 with 65° N latitude has anomalously high concentration between March-April. These observations may be explained with higher level of ^{7}Be in the arctic vortex during wintertime, which influences USP76

during springtime once the vortex breaks up, or they may be due to the effect of stratospheric intrusions.

- The same scenario applies for lowest latitude in bands 7, and 8 sharing AUP05 with high concentrations around the year, peaking between November-February.

- Band 7 present the highest concentration span from zero to 11,000 µBq/m³. It does not show much seasonal variation like band 8 as they share FRP29 and FRP30 with steady low ^{7}Be levels probably due to continuous washout effect. Similarly, in band 11 and 12 at PGP51 with latitude of 3° S typically in the middle of the ITCZ which is characterized by regular precipitations as explained by Kusmierczyk-Michulec et al.(2015)[37].

- Band 9 and 10 share 3 stations: RUP56, PHP52, AUP10. Plots are substantially different because the stations marking the HFDZ lines are different ones for each band. With the exception of band 1, 8, and 12 all bands present strongest seasonal activity variations between May and September.

3.1.2. Latitude effect

Europe is covered in the northern part of Band 6 and 7. Hernandez-Ceballos et al. (2016)[27] made a feasibility study using ^{7}Be to identify airborne radioactive spatial patterns in three European clusters denoted as C1, C2, and C3. This study suggests as previous works[15,31,32] that the spring–summer ^{7}Be maximum concentration is mainly due to the impact of the tropopause height. A tropopause fold is often associated with the injection of stratospheric air into the troposphere. Results by Hernandez and Iannidou[26,27,31,32] present the tendency to increase the tropopause height with decreasing latitude. There is a positive correlation observed between tropopause height and ^{7}Be activity concentration.

A comparison is done of the dataset from SEP63, DEP33, MRP43 (Latitudes 59°, 48°, 18° in band 6 and 7) with European clusters C1, C2, C3 respectively for the years 2007, 2008, 2009, 2010. Data were compared based on the monthly index mean calculation as described in the paper of Hernandez-Ceballos et al. (2016)[27].

Taking into account the statistical significance of comparing few datapoints, Figure 23 indicate that there is an indication that dataset correlate, both displaying the same ^{7}Be concentration trend influenced by latitude, lower north and increasing southward (Figure 23, right plot).
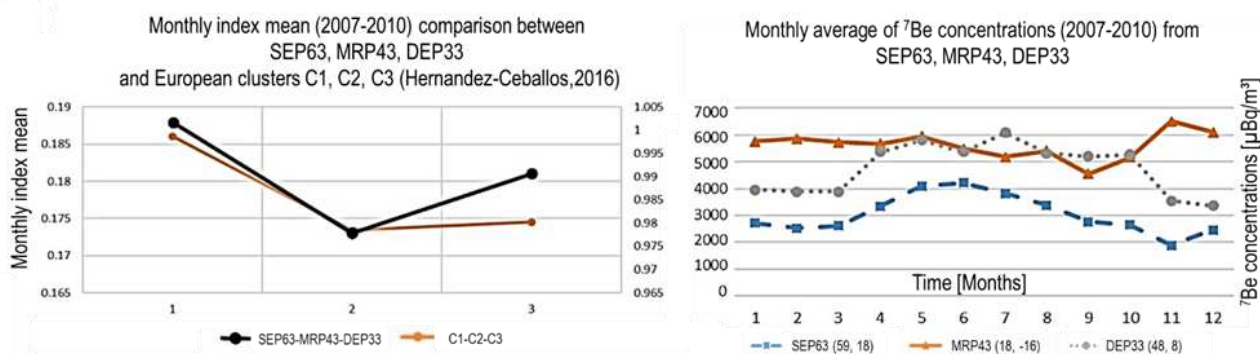
Figure 23. Left plot: Monthly Index Mean trend calculated over 4 years from 2007 to 2010 for SEP63, DEP33, MRP43 and European Clusters C1, C2, C3 27. Right plot: ^{7}Be concentration trend influenced by latitude, lower north and increasing southward (µBq/m^3). (Terzi and Kalinowski, 2017)

3.1.3. Beryllium-7 global concentration maps

Figure 24 and Figure 26 illustrate the global ^{7}Be concentration map for each month. Like in the longitudinal bands' plots, Figure 24 green-blue areas are synonymous for ITCZ and PFCZ while yellow-orange-red are related to HFDZ in both Northern and Southern Hemispheres. Table 9 shows for each monthly plot the data used as reference.

Examining the sequence ^{7}Be levels increase between June and August from the Middle East to East Asia and decrease until minimum is reached in December. That area is correlating with the position of the HFDZ in the Northern Hemisphere. In the Southern Hemisphere, HFDZ is strong in December -January and decreases till a minimum is reached in June. Summertime hot spot over Middle East is related to the tropopause fold due to dynamical interactions between the subtropical jet and the Asian monsoon anticyclone[1].

Small modulations occurring during the 12 months are better highlighted in Figure 25 and Figure 27 where for each grid point the normalized activity value has been used. Normalized values were calculated dividing the monthly average by the average over all months for each grid point. Table 10 presents the normalized values while averages over all months used to normalize each grid point value can be found in Table 9. Modulations seem to have a northward trend from January to July and southward from July to December with peaks in March/April and October.
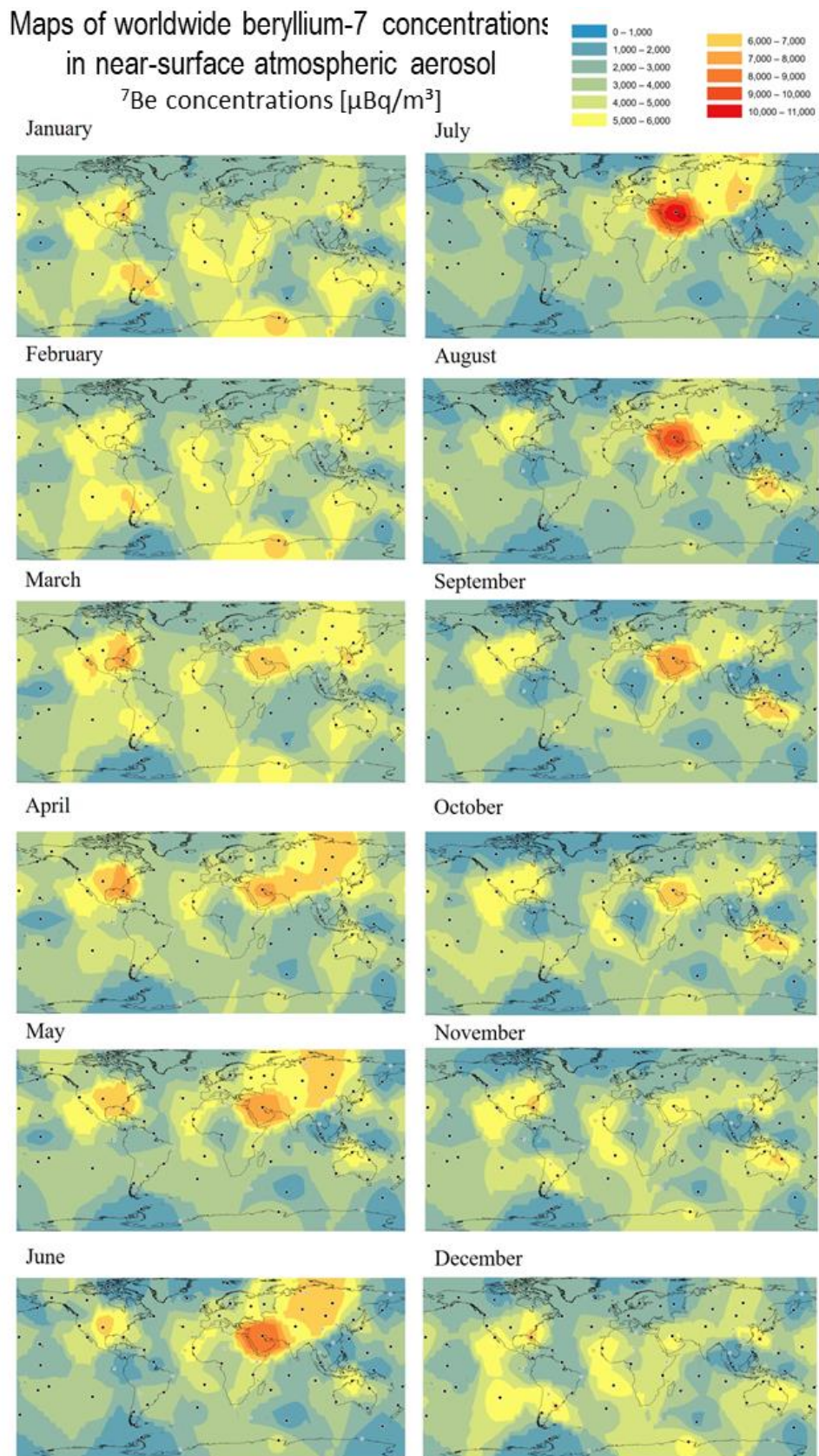
Figure 24. Global ⁷Be (µBq/m³) map grid with one plot per month. (Terzi and Kalinowski, 2017)
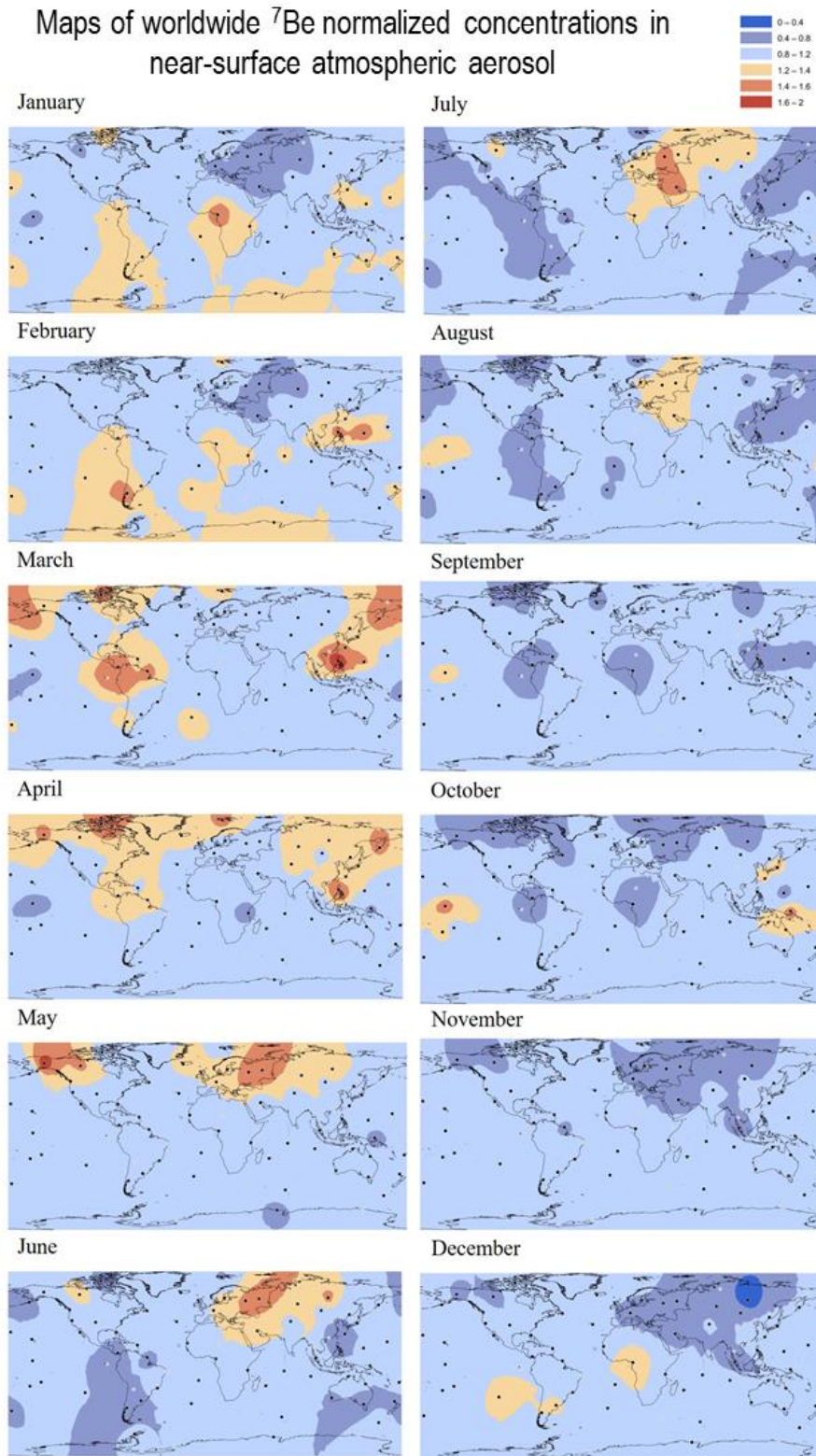
Figure 25. Global ⁷Be map grid with one plot per month using normalized concentration values. (Terzi and Kalinowski, 2017)
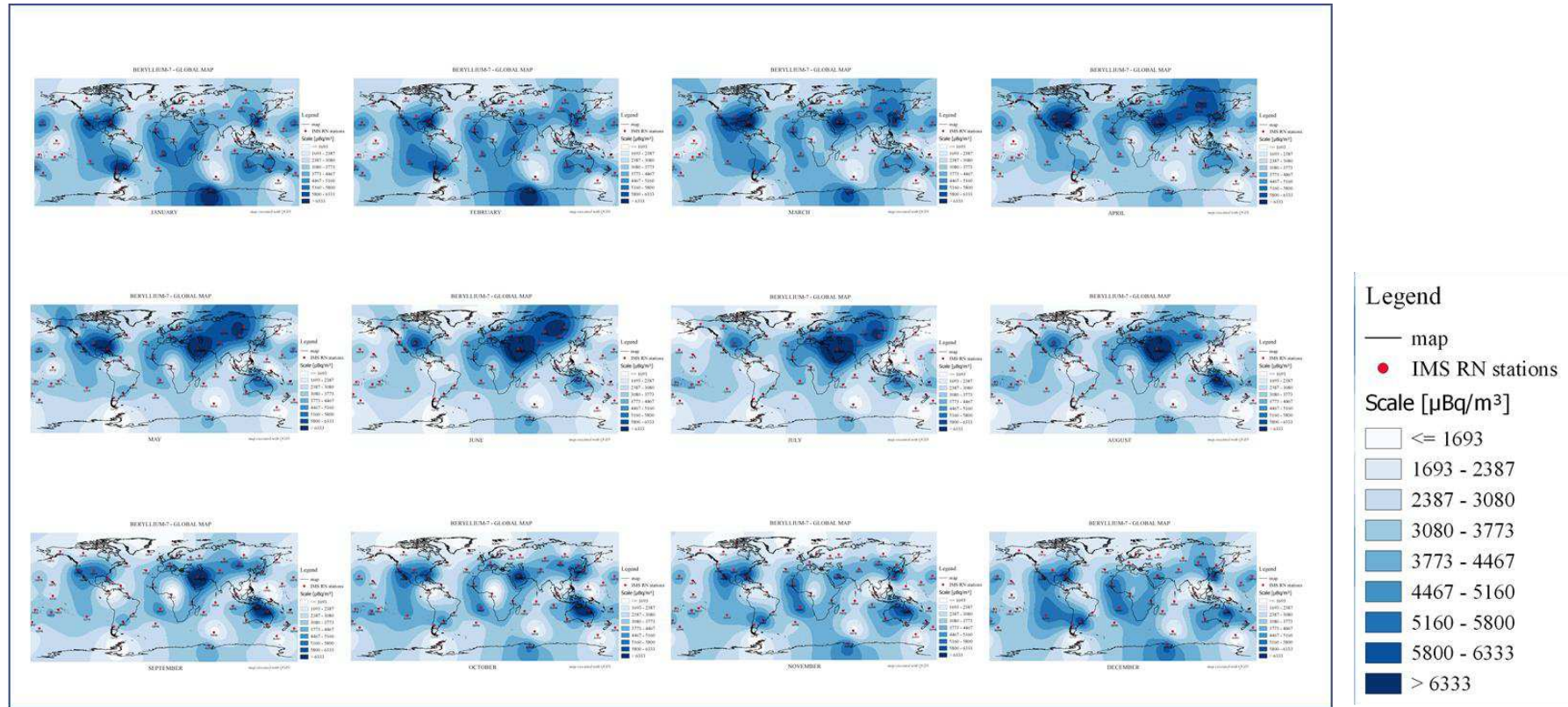
Figure 26. Global ^{7}Be (µBq/m³) map grid with one plot per month. The interpolation method used is multilevel b-spline which provides a smoother boundary effect compared to Figure 24. (Terzi and Kalinowski, 2017)
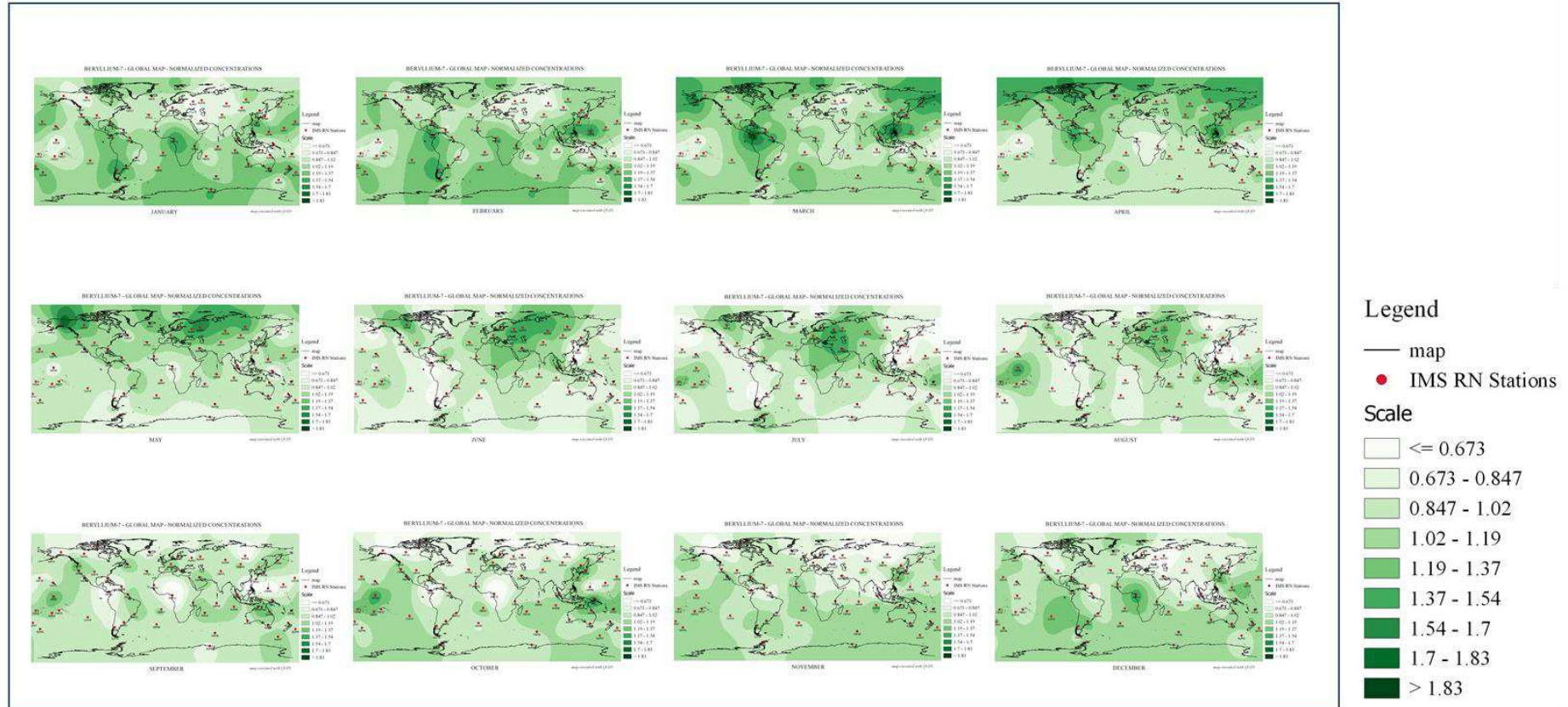
Figure 27. Global ⁷Be map grid with one plot per month using normalized concentration values. The interpolation method used is multilevel b-spline which provides a smoother boundary effect compared to Figure 25. (Terzi and Kalinowski, 2017).

3.2. Walker Circulation and El Niño Southern Oscillation (ENSO)

Figure 28 shows the ^{7}Be map for the equatorial band with structure visible at TZP64, AUP09, and PAP50.
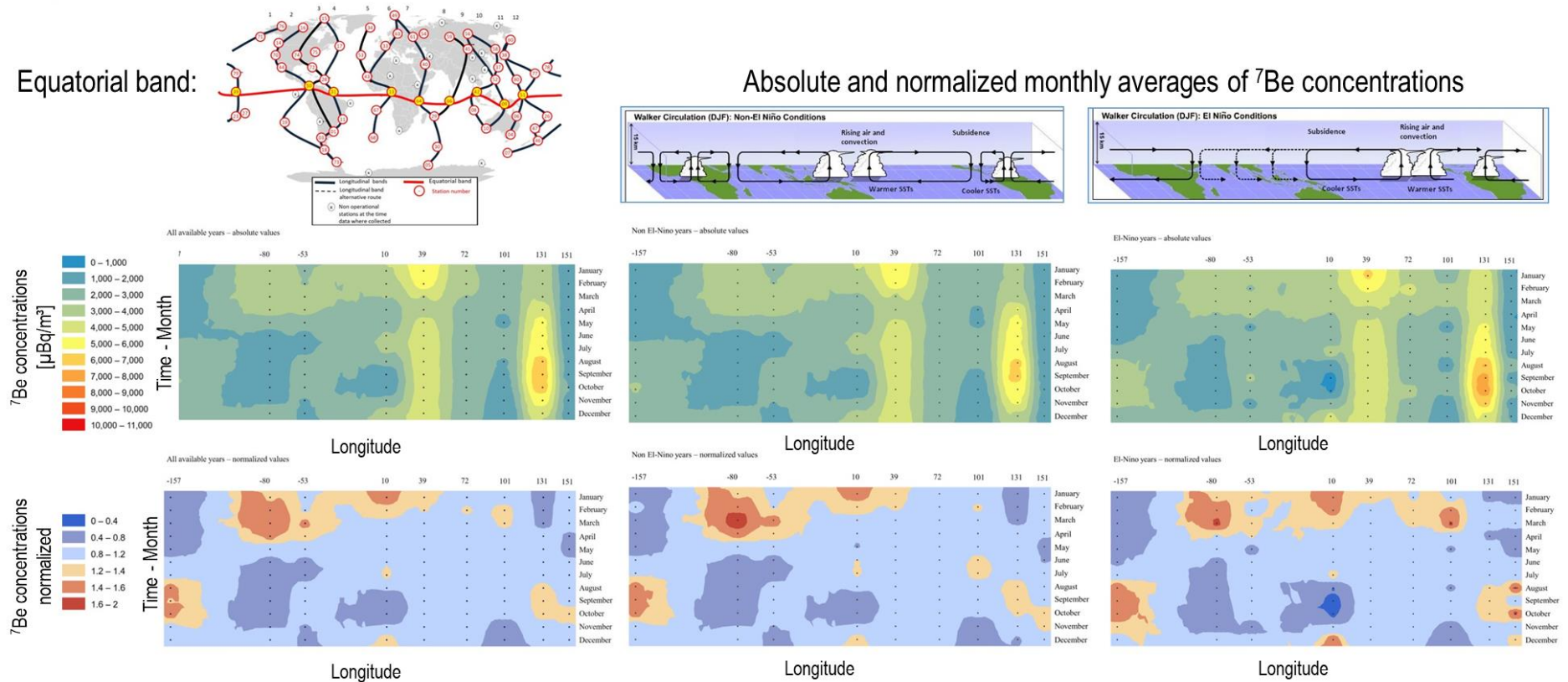
Figure 28. Equatorial band (top plot) quasi-3D concentration (µBq/m³) pattern (lower plot) averaged over all available years, over all El Niño years and over all non-El Niño years, compared with Walker circulation structures during El Niño and non-El Niño conditions (top right plots from ©forum.arctic-sea-ice.net, 2017). List of El Niño years from www.cpc.noaa.gov. (Terzi and Kalinowski, 2017).

The equatorial ^{7}Be map relates well with the circulation patterns during El Niño condition and highlights the increment of ^{7}Be concentrations during the ENSO periods. There is a correlation between higher ^{7}Be concentrations and downward atmospheric influx. Table 11 presents the data used to produce these equatorial band plots. To focus more on the El Niño area, one can look at Darwin (AUP09) and Tahiti (FRP27) stations.
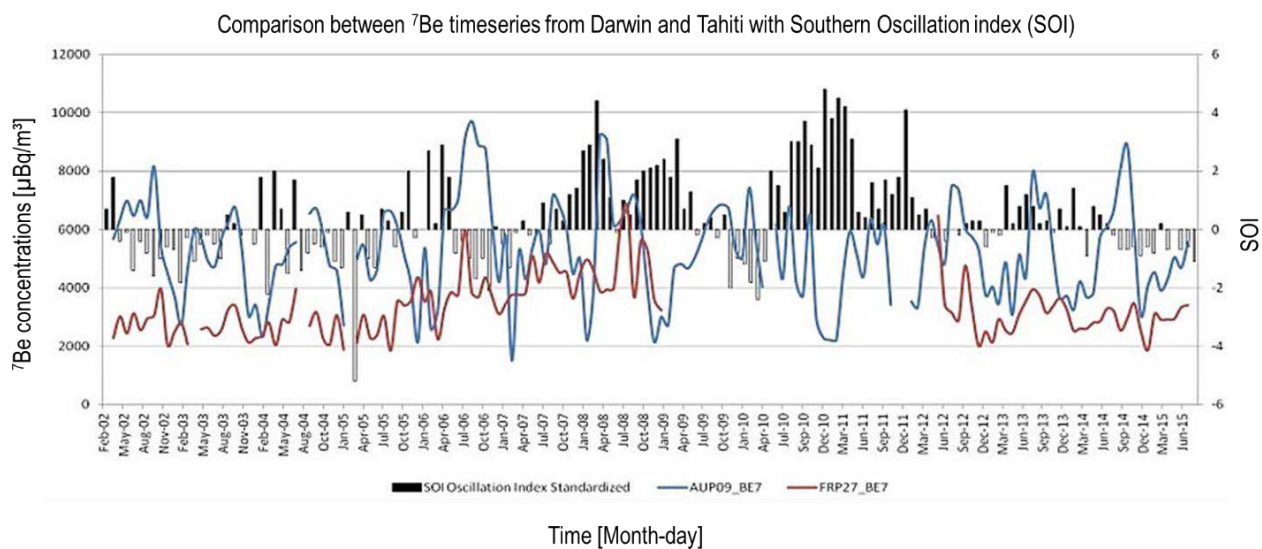
Figure 29. SOI compared with ^{7}Be time series (µBq/m^3) at AUP09 Darwin and FRP27 Tahiti. (Terzi and Kalinowski, 2017)

For ^{7}Be at FRP27 a weak correlation can only be seen with the longer periods of highest SOI values. During El Niño condition, the trade winds change direction on the central Pacific area and therefore decreasing the levels of ^{7}Be measured in Darwin. The pressure difference and the SOI follow a similar pattern (Figure 30).

SOI and ONI compared with ^{7}Be concentrations [µBq/m³] and pressure difference between Darwin and Tahiti
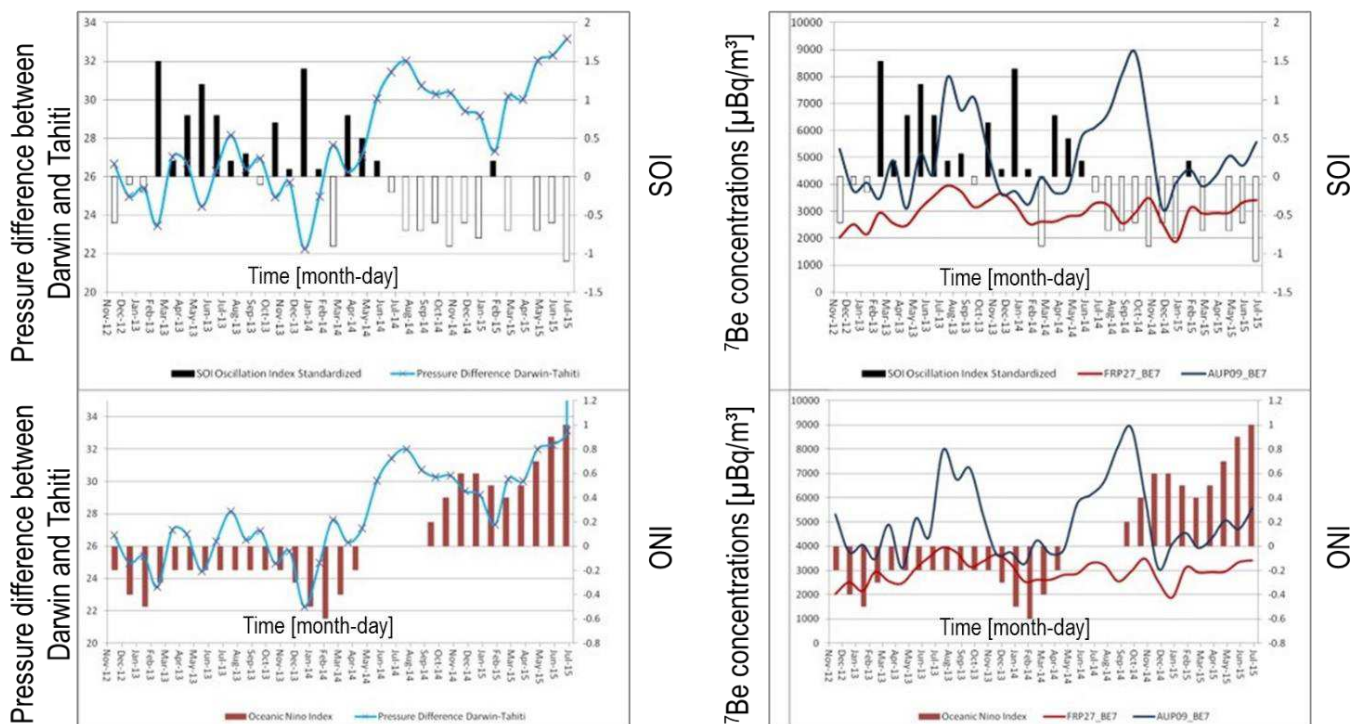
Figure 30. SOI and ONI compared with ^{7}Be concentrations (µBq/m³) and pressure difference between Darwin and Tahiti. (Terzi and Kalinowski, 2017)

Based on ^{7}Be concentrations, it may be possible to develop an early warning indicator for ENSO. The SOI follows later, after the El Niño has developed, because the difference in rain intensity it relies upon results from the El Niño. In contrast ^{7}Be is an indicator of the global circulation patterns that starts developing and being revealed by ^{7}Be concentrations with a certain lead-time before the El Niño develops and starts having impact.

3.3. Sudden Stratospheric Warmings (SSW)

SSW involve rapid stratospheric temperature increases and by propagating downward into the troposphere they impact wintertime surface climate causing cold outbreaks in north America and Eurasia and extreme warming over regions of rapid ice change such as Greenland[75].

Following an SSW the high-altitude winds reverse to flow eastward instead of their usual westward direction. The eastward winds progress down through the troposphere and weakens the jet streams giving easterly winds near the surface and resulting in dynamic reduction in temperature in Europe during wintertime.

The comparison of SSW events from 2002 to 2015 with northern hemispheric stations (CAP15, CAP17, ISP34, NOP49, RUP61, SEP63) reveals a very clear increase of ^{7}Be at two of the relevant RN stations at the time of some SSW events, but does not find any obvious correlations repeating for more than three SSW events (Table 3).

Table 3 List of Sudden Stratospheric Warming (SSW) events from 2001 to 2015 (left column) and possible correlated pattern in RN stations time series (right column).

SSW events from 2001-2015	Correlations with RN stations
31 December 2001	Not found
18 January 2003	ISP34
09 January 2004	ISP34
16 March 2005	Not found
25 January 2006	Not found
26 February 2007	Not found
24 February 2008	Not found
29 January 2009	Not found
30 January 2010	CAP17
17 January 2012	CAP17
17 January 2013	ISP34
31 March 2014	Not found
05 January 2015	Not found

For instance, for CAP17 the maximum yearly peak matches with SSW in 2010 (Figure 8, left plot) and 2012 but not in the other years. The reason why some years did not present sign of SSW was not found but only observed.
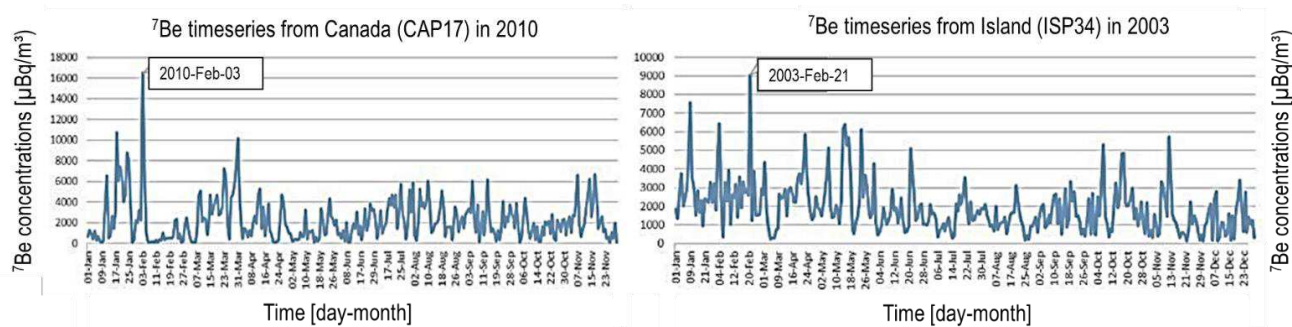
Figure 31. CAP17 and ISP34 ^{7}Be time series (µBq/m^3) 2010 and 2003. Data point marked in correlation to an SSW event. (Terzi and Kalinowski, 2017)

Same for ISP34 the maximum peak matches for the year 2003 (Figure 31, right plot), 2004 and 2013 only. These initial finding may benefit from further analysis as the SSW event may appear as less pronounced ^{7}Be peak or with a specific delay that is not investigated here. The delay may be days up to a couple of weeks, this depends on how the SSW develops and what kind of changes of the circulation patterns it generates and how long these last.

Pacini (2015)[58] refers in an SSW abstract to the correlation between ^{7}Be concentrations and an SSW event in Brazil in September 2002 but no significant correlation was found between ARP01 in Argentina time series and the cited event, see Figure 32.
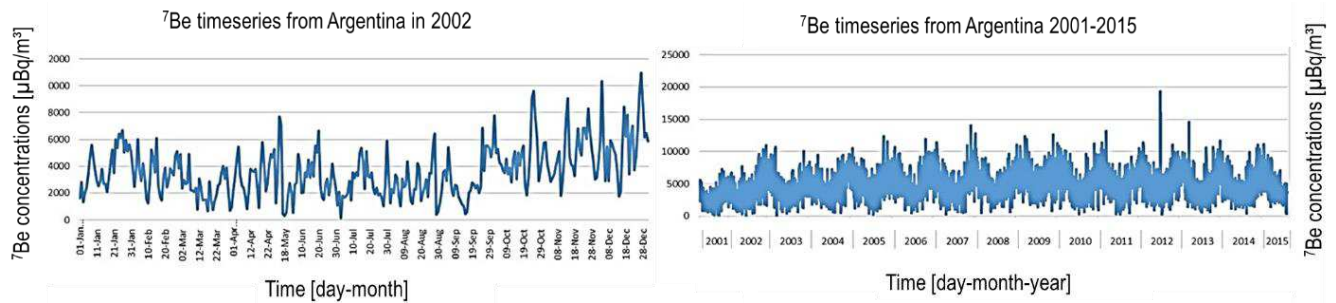
Figure 32. ARP01 ^{7}Be levels (µBq/m³) time series for 2002 (left), ^{7}Be levels (µBq/m³) time series from 2001 to 2015. (Terzi and Kalinowski, 2017)

Further study is required in order to confidently associate ^{7}Be patterns with SSW.

3.4. Solar Energy Particle (SEP) Events

Solar energetic particle events present short term ^{7}Be production and overall influences the effect on ^{7}Be surface concentration values[99]. Usoskin's paper[99] discusses the SEP event of January 20th 2005. They produce a worldwide variation in ^{7}Be production at stratospheric level, especially at high latitude, although only 2% of that injection is reaching down to the surface and this will be barely visible in ^{7}Be observations.

The concentrations at the polar station CAP15 may be studied to see any possible peek related to the SEP of 20th January 2005, see Figure 33.
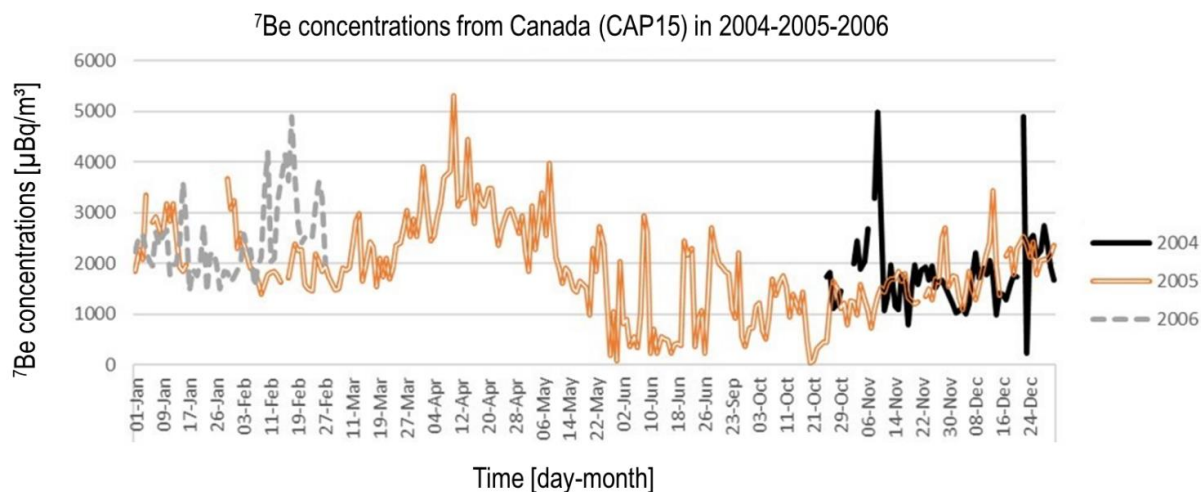
Figure 33. CAP15 ^{7}Be levels (µBq/m³) time series for 2004, 2005 and 2006 overlapped. (Terzi and Kalinowski, 2017)

No particular increment is noted after the SEP event therefore the effect is too small to be clearly detected at ground level, thus consistent with Usoskin's work[99].

3.5. Quasi-biennial Oscillation (QBO)

QBO is an oscillation of the zonal winds in the tropical stratosphere between easterlies and westerlies every 28-29 months. QBO is the most regular aspect of the circulation in the atmosphere that is not following the annual cycle. It is believed to be internally forced in the tropics via interaction of the prevailing flow with upward travelling waves dissipated in the stratosphere by radiative cooling. I studied if the QBO is accompanied by a visible phenomenon on surface ^{7}Be measurements along the stations in the equatorial band. For some stations, in particular KIP39, the oscillation seems to be present, with maxima peaks in 2007, 2009, 2011 and 2013 (Figure 34).
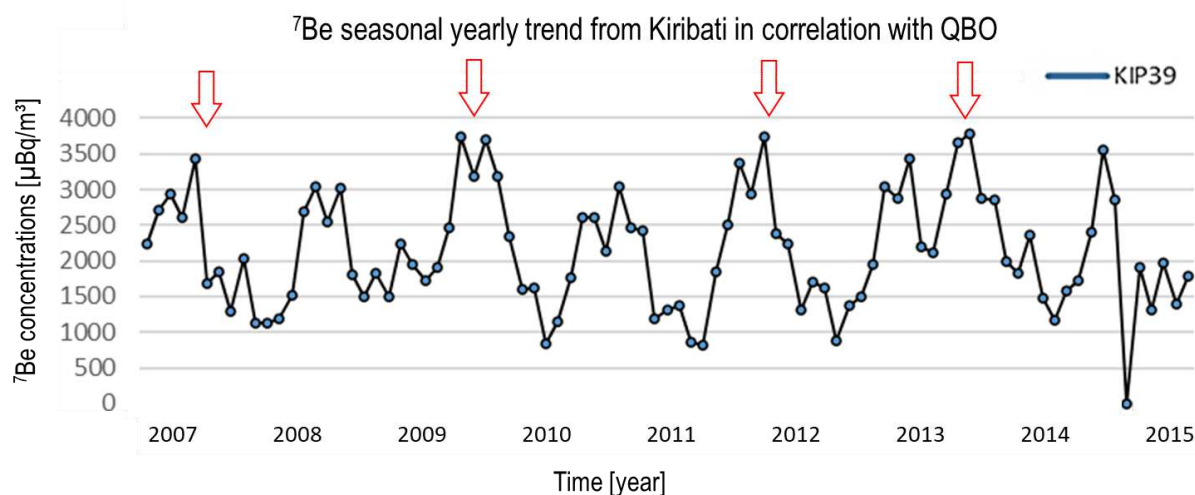
Figure 34. KIP39 monthly averaged (µBq/m³) from 2007 to 2015. Red arrows highlight position of highest peaks within maxima. (Terzi and Kalinowski, 2017)

The trend is a visible seasonal-yearly pattern with maxima and minima between September and January and a biannual oscillation between highest peaks. Studying the 11-year period we see within two groups of peaks, minors and majors, the last ones with a biannual pattern, which could be reconciled with QBOs. According to Baldwin et al. (2001)[5] the consensus has not been reached on the subtle relationship between stratospheric-tropospheric ^{7}Be exchange and QBOs. The Tropical troposphere in fact has a quasi-biennial oscillation of its own, uncorrelated with stratospheric QBOs[109] . Nevertheless, the equatorial QBO affects the extra-tropical circulation significantly during winter, in particular during mid-winter, because of the induced changes in wave propagation and meridional circulation (Brewer-Dobson circulation). The zonal mean of the Brewer Dobson circulation (BDC) is stronger during QBO-East (easterly) than QBO-West (westerly), therefore the downward branch of the BDC imposes a decrease in tropopause height at high latitudes during QBO-East compared to QBO-West[5].

Further analysis of KIP39 patterns may benefit from more detailed analysis. A recent work on QBO[57] states that unprecedented deviation from 1953 to today has been observed in QBO in 2015-2016. Westerlies upward displacement seems to cut off the normal downward propagation of easterlies. This abrupt change may be set by a steady forcing mechanism which could be further investigated using ^{7}Be data. Such anomaly should result in a significant decrease of ^{7}Be concentration for grid points with strong downward influx.

3.6. Monsoon prediction

Monsoon regions are located in Asia-Australia, West Africa, and to a lesser degree in North and South America[9]. The ^{7}Be trans-equatorial method as introduced in chapter 2 offers a simple and useful mechanism to predict the formation of monsoons triggered by HFDZ progression[122].

The link between ^{7}Be, Intertropical Convergence Zone and Indian monsoon onset and withdrawal is described in Figure 35.
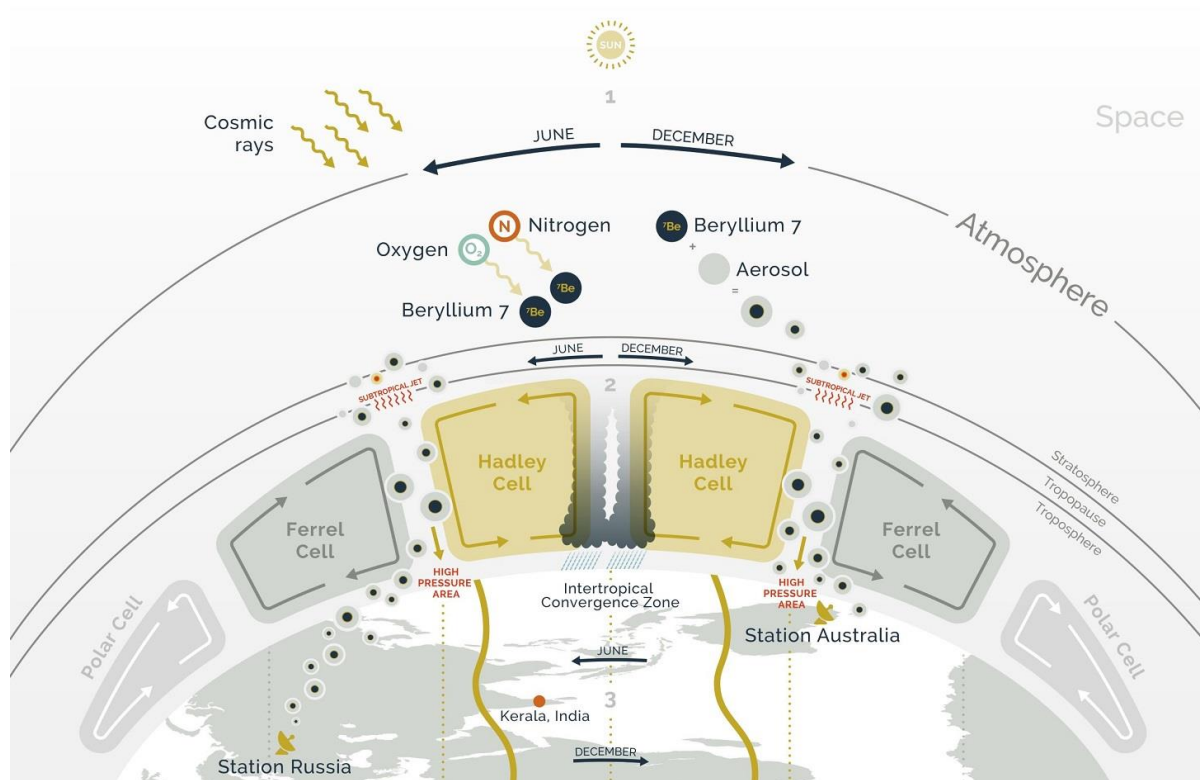
Figure 35. Points 1, 2, and 3 show the link between the heat produced by sunlight, earth rotation and Hadley cell progression with the monsoon pathway delimited by the intertropical convergence zone. (Terzi et al., 2019)

While in the upper part of Figure 35 we see production and transport of ^{7}Be, the lower part shows how the ITCZ follows the sun moving northward from January to June and southward from July to December. As the sun moves, the ITCZ moves and consequently also the Hadley-Ferrel and Polar cells. The red dot indicates the region of Kerala in India, used as reference point of the Indian monsoon. High-pressure areas (red marked) indicate the surface location of

high-pressure ridges formed simultaneously with the subtropical jet stream as a result of the Hadley circulation.

Unlike using statistics of local parameters where the Indian monsoon is expected, time series of ^{7}Be activity concentration from RUP61 and AUP04, north and south of the equator, are required. Their change-over time indicates the progression of atmospheric cells, which governs the monsoon circulation. The capability to measure the downward flux of an atmospheric cell allows to determine the approach of the monsoon onset (Figure 36).

The statistical significance and the methodology are limited to the length of the available dataset of ^{7}Be currently covering a ten-year period only. Long-term significance of the findings will be demonstrated with time and larger datasets which are currently not available.

Although the study presented here focuses on the Indian monsoon, the transferability of the trans-equatorial approach has been tested to other monsoon regions. As long as the monsoon is triggered by progression of atmospheric cells such as the Hadley cell for the monsoon over Kerala, the trans-equatorial method can be applied to other monsoon regions as well[54] (Figure 37).
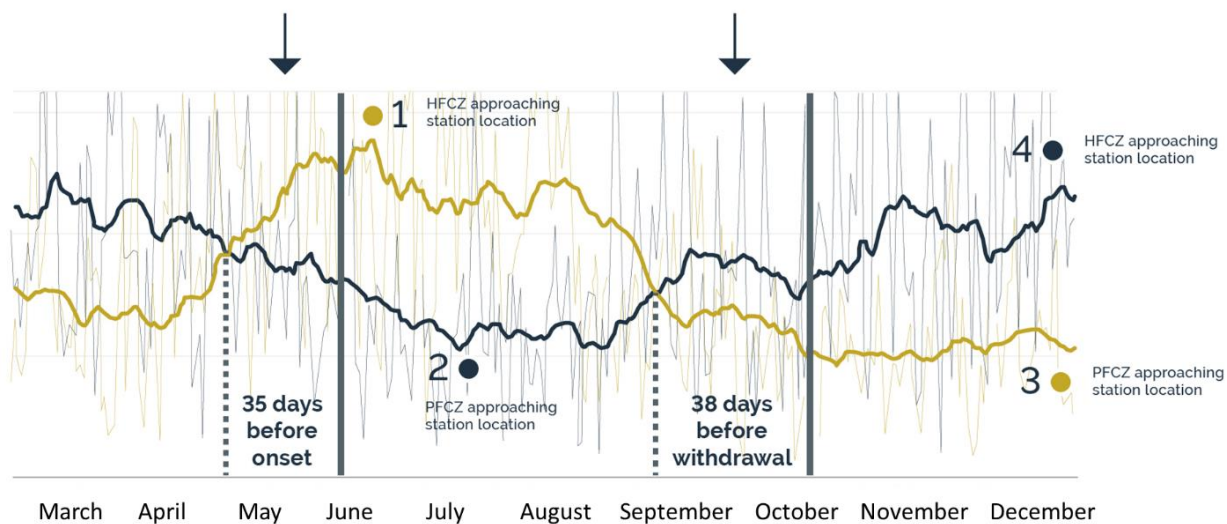
Figure 36. High correlation (PCC 0.72) between Monsoon over Kerala (MOK) and ⁷Be with an average warning time of 35 and 38 days for MOK onset and withdrawal respectively. (Terzi et al., 2018)
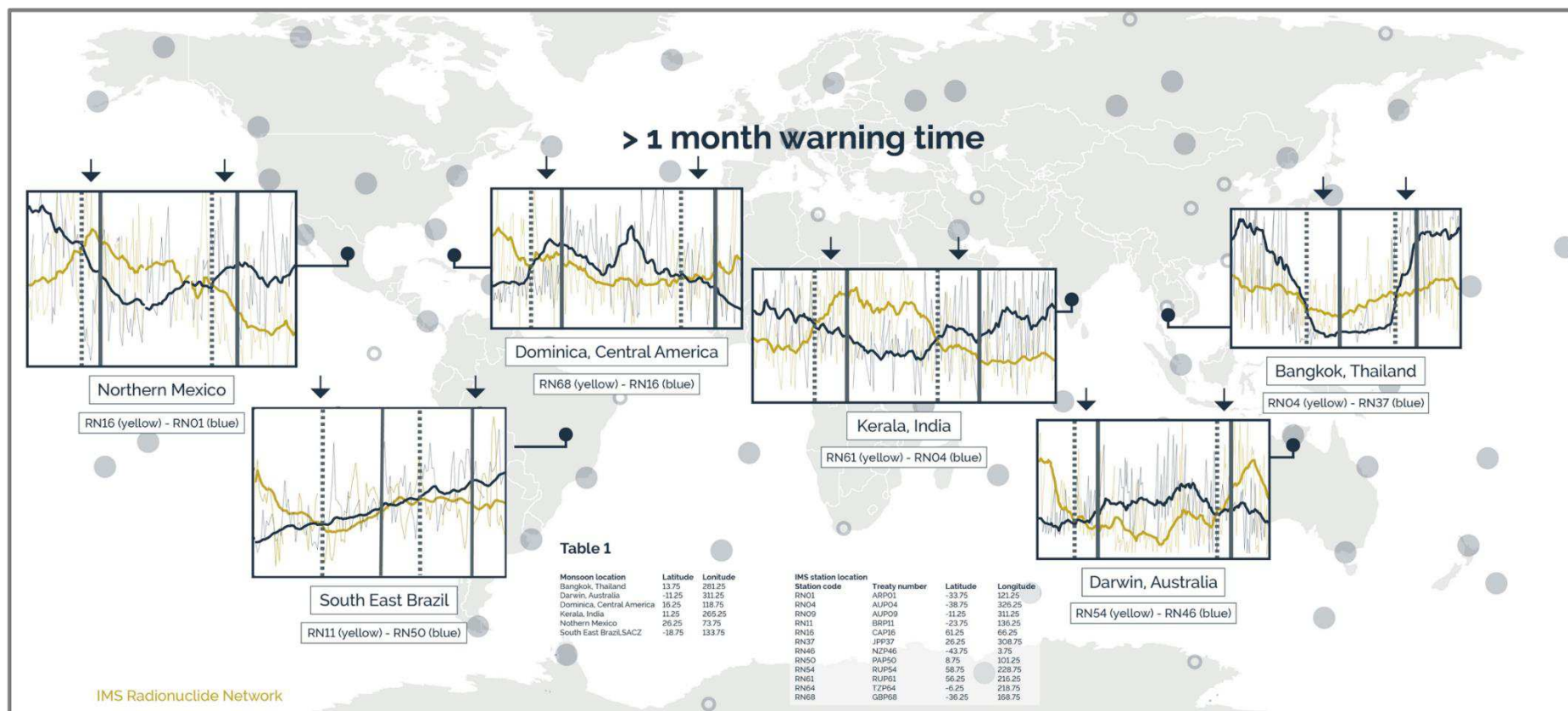
Figure 37. Examples of different locations around the world where the ^{7}Be trans-equatorial technique also applies. Precipitation data for Dominica, Bangkok, South East Brazil and Northern Mexico are based on monthly precipitation median from the CPC Merged Analysis of Precipitation (CMAP). The precipitation values are within 300 km radius from the given location. (Terzi et al., 2018)

3.6.1. Case study on the Indian monsoon

Based on RUP61 and AUP04 cross points, the presented empirical method describes the possibility to predict the onset of the monsoon over Kerala (MOK) eight months in advance with a ±6-day standard deviation, six weeks in advance with a ± 3-day error margin and one months in advance with an accuracy of ± 2 days. Applying this new method may enable better preparation for economic and natural hazard impacts of the monsoon season in India. The warning time currently provided by the Indian Meteorological Department is between 1 to 3 weeks with an error margin of ±5 days[54].

The map in Figure 35 and Figure 36 presents the two IMS stations (RUP61 in Dubna, Russia and AUP04 in Melbourne, Australia) selected to make seasonal predictions for the Kerala monsoon. In Figure 36, [7]Be cross points mark the intersection of 30 days running average of the daily [7]Be activity concentrations (shown in yellow and black). Left plot shows how the trend of the stations time series are an expression of HFDZ shift and because of their location the cross point is in accordance with the ITCZ progression towards Kerala region, right plot. By reducing the average time to 15 days (0/-15) the warning time can be sensibly improved to 52 days with CP1 (Figure 38 top chart). On the other hand a long term mean (0/-120) as shown in the lower part of Figure 38 cannot be used for onset prediction but becomes necessary to study long term circulation changes that are relevant in the domain of global warming as presented in the next paragraphs.

The sine-like curve with a period of one-year, as an expression of HFDZ progression, is visible in Figure 36, Figure 37 and Figure 38.
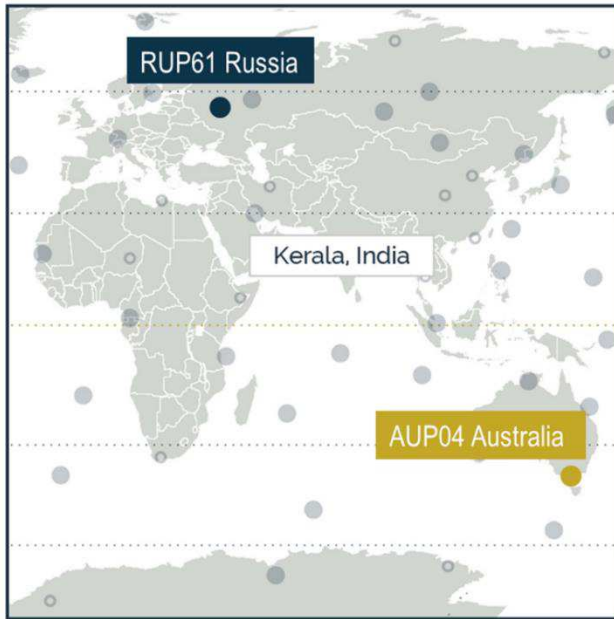
Figure 38 Multi-year time series (2003–2018) from Australian (orange line) and Russian Stations (blue line) based on normalized daily activity concentration of [7]Be averaged over 0/-15 days (left top) and 0/-120 days (left bottom) (Terzi et al., 2019)

As mentioned previously the primary purpose of moving averages is to smooth out short-term variations due to local processes such as wash-out by rain and cyclonic events. The type of statistical calculation such as moving average and normalized moving average are a standard approach to increase data accurac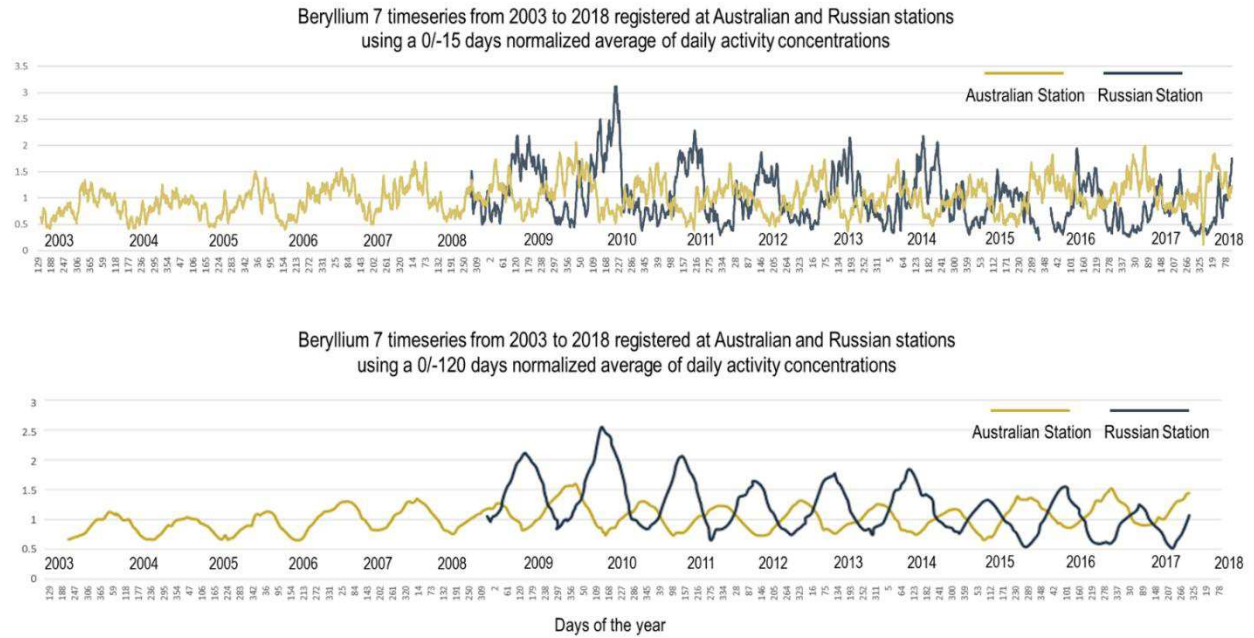y. Appropriate time series trend line calculations (normalization and period of moving averages) may differ based on station, monsoon region, and type of analysis needed.

As demonstrated in the past decade, there is a direct correlation between the monsoon length and the intensity of the monsoon. IMD defines monsoon intensity as percentage of Long Period Average (LPA) of the rainfall over the country as a whole during the monsoon season from June to September. Since the length of the monsoon can be determined with this method, conclusions about its intensity can also be made. The further apart CP1 and CP2 are, the longer and more intense the monsoon will be.

Based on the trans-equatorial approach, four methods have been developed to make monsoon onset predictions as early, reliable, and accurate as possible over time. Method (A) uses CP2 of a given year for monsoon onset of the following year. Methods (B) and (C) use CP1 for monsoon onset of the same year. Trend lines for methods (A) and (C) are built by moving average of past 30 days, while (B) is built as normalized moving average of past 15 days. These methods are shown in Figure 39 and results are summarised in Table 4.

Figure 39 illustrates the forecast for 2009–2017 monsoon onset over Kerala using all 3 approaches (A, B, and C) over time. The different methods (A, B, and C) help build up more accurate forecast over time. The standard deviation decreases from 6 to 2 days over a period of 7 months. In the lower right chart, one can see the predicted forecast for 2018. Method A: 266 days before onset of the following year, standard deviation of 6.1. Method B: 52 ± 3.7 days before onset, Method C: 31 ± 4.7 days before onset. The average predicted onset (method D) based on method A, B, and C is known 30 days ahead of monsoon onset and has a standard deviation of +/- 2 days (2018 example shown with red dotted line). In order to fill the gaps between points in time for method A and B, additional locations for cosmogenic radionuclide detection would be necessary or other statistical features than cross points of ^{7}Be time series could be utilized.

For method A, using the same dataset to predict monsoon withdrawal and the onset of the following year is based on a correlation between CP2 and both dates. Although the correlation

of method A is weak (PCC 0.37) it still indicates that any delay in the atmospheric cell progression to a certain extent also affects the arrival of the monsoon in the following year. That correlation is found in the past 10 years using ^{7}Be, it is also found using IMD monsoon withdrawal and onset dates from 2009 to 2017 (PCC 0.39) and in withdrawal and onset date from the Department of Hydrology and Meteorology of the Government of Nepal (PCC 0.54)[11]. The overall correlation from 1968 and 2017, however, is 0.05, which means that the correlation obtained in our time window may be a decadal effect or a new trend, possibly due to climate change.

One month before the monsoon onset occurs, all three predicted onsets are known, and an average prediction date can be calculated (method D). Compared to the actual monsoon onset, the averaged prediction date leads to a standard deviation of ± 2.1 days. Method D provides a first approach to the consideration of the annual cycle of cell movements. HFDZ may have different progression velocities and different delays throughout the year. The delay in cell progression accumulated between June and September (method A – CP2) is diminished and counterbalanced in March (method B – CP1) and May when the latest cross point occurs (method C – CP1). Different velocities of the cell progression throughout the year are blended in the averaging of method A, B and C, and that is why the best standard deviation is reached. Further research is required to demonstrate the significance of these results and to interpret them as the blending of different driving forces. Method A has high uncertainties and cannot be used alone for monsoon onset prediction, especially as it may be based on a decadal trend that can be reversed in the future. Method D shows the most robust and accurate results with ± 2 days standard deviation.

2009

IMD Onset day
#143

Days to Monsoon onset

2010

IMD Onset day
#151

Days to Monsoon onset

2011

IMD Onset day
#149

Days to Monsoon onset

2012

IMD Onset day
#157

Days to Monsoon onset

2013

IMD Onset day
#152

Days to Monsoon onset
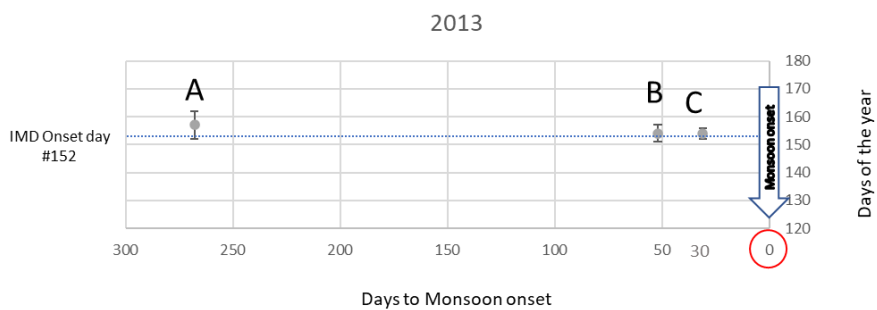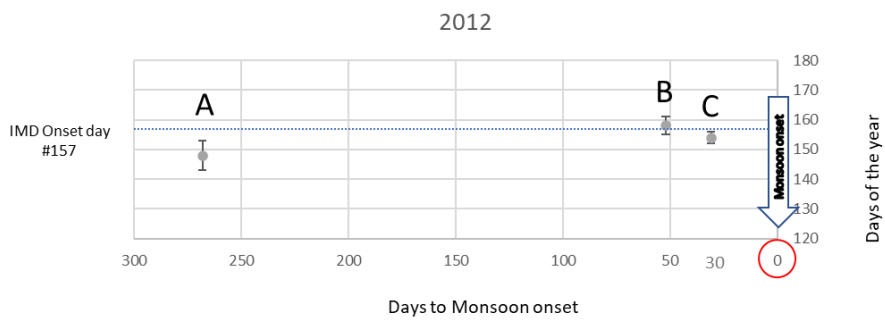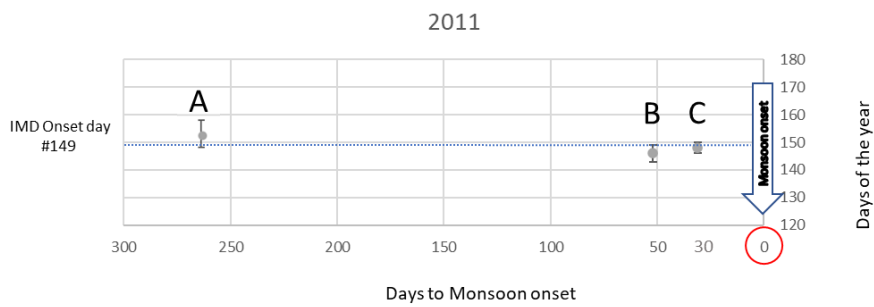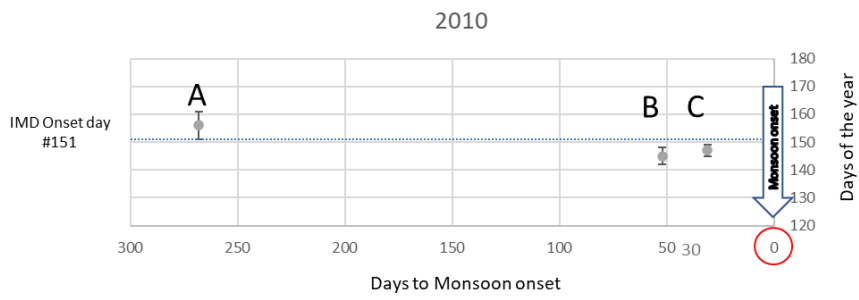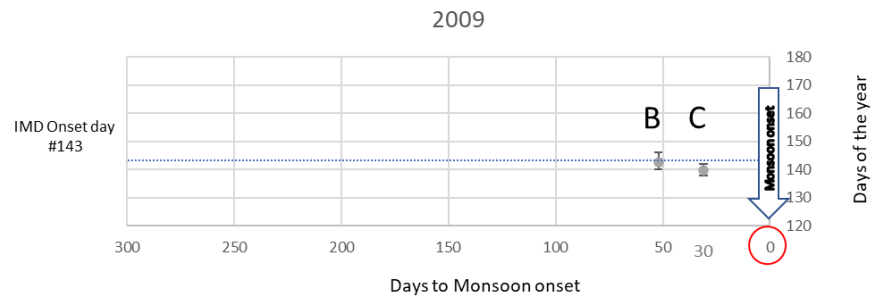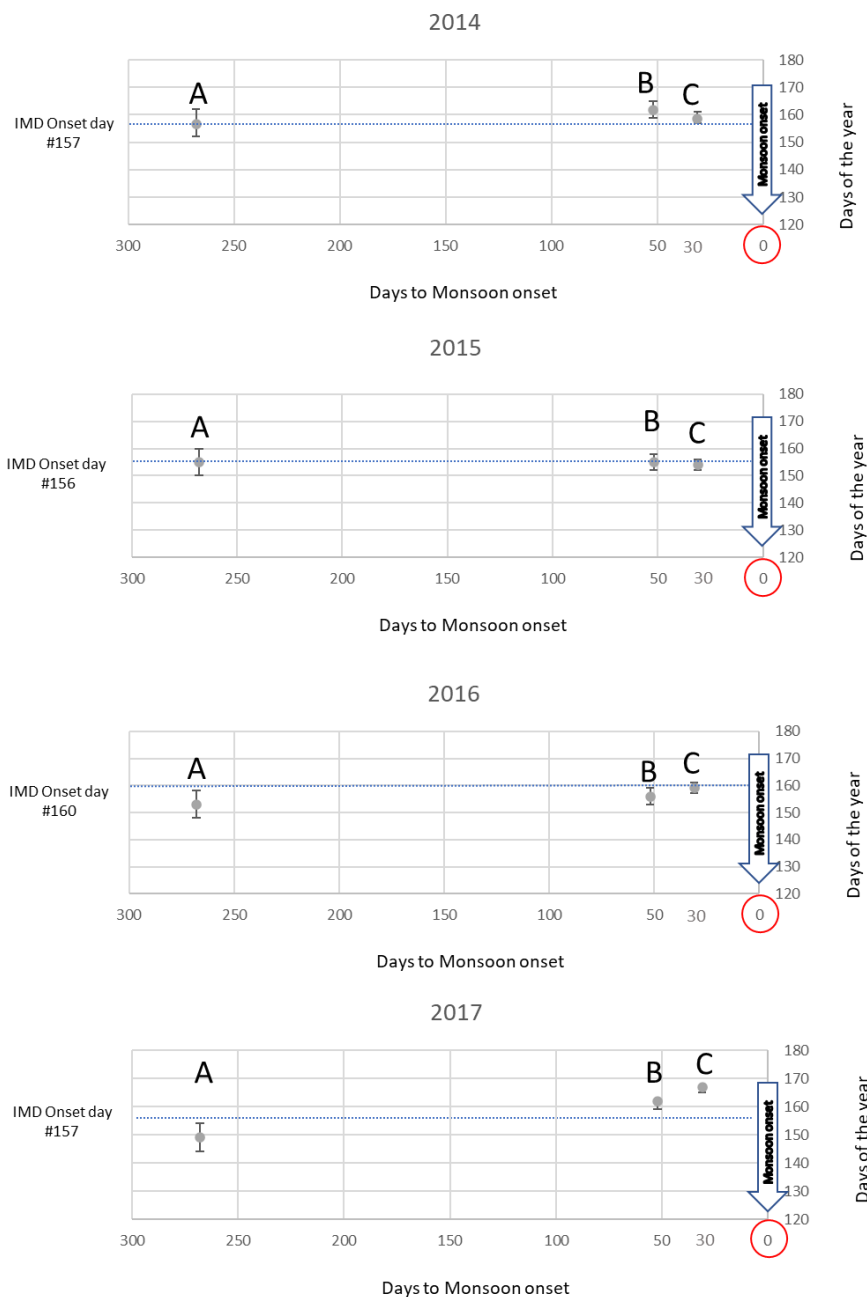
Figure 39. Methods A, B, and C help build up more accurate forecast over time. Dotted line in the resulting onset date built by averaging A, B and C data-points. (Terzi et al., 2019)

The value of any monsoon onset prediction method is determined by its reliability to forecast accurate dates and the length of its lead time. The correlation between onset and withdrawal versus their cross points (CP1 and CP2) is 0.89 and 0.73 respectively (Figure 40).

The ^{7}Be cross point technique has been compared with the change point (CHP) index method confirming improved accuracy and extended onset lead time for all available years[92,101].

Monsoon withdrawal dates are predicted with method E which uses CP2 obtained with 0/-15 days normalized average of [7]Be activity concentrations. The resulting lead time is 42 days with a standard deviation of ±7.2 (Table 5).
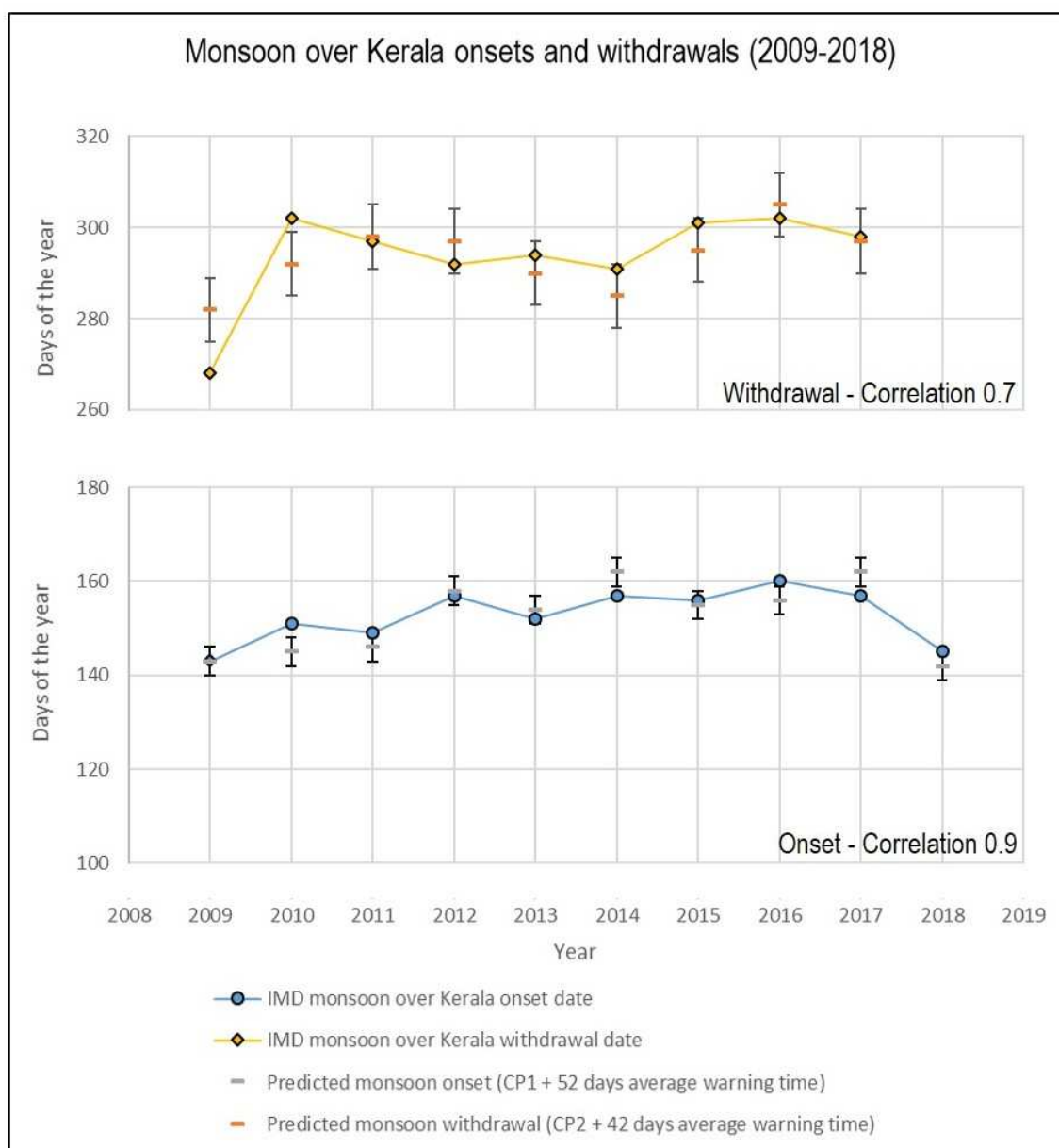
Figure 40. Correlation between onset and withdrawal dates of the monsoon over Kerala provided by the Indian Meteorological Department (IMD) and through the trans-equatorial approach. (Terzi et al., 2019)

Table 4 For each predicted monsoon onset provided using method A, B C and D the corresponding difference from Monsoon onset is given. Kerala is the reference region for monsoon onset. Accuracy (trueness and precision) is defined by ISO 5725-1

	Accuracy			
Year	Method A difference between IMD monsoon onset and predicted onset (n. of days)	Method B difference between IMD monsoon onset and predicted onset (n. of days)	Method C difference between IMD monsoon onset and predicted onset (n. of days)	Method D Averaged difference over method A, B and C (n. of days)
2009	n/a	0.1	-2	-1
2010	3	-6	-3	-2
2011	9	-3	0.1	2
2012	6	1	-2	1.7
2013	-6	2	3	-0.3
2014	-2	5	3	2
2015	-3	-1	-2	-2
2016	-7	-4	0.1	-3.6
2017	-8	5	10	2.3
2018	4	-3	-8	-2.3
-Trueness- Difference between IMD monsoon onset and predicted onset using method A, B, C and D averaged over all available years (2009-2018)	-0.44	-0.39	-0.08	-0.32
-Precision- Standard deviation of the difference between IMD monsoon onset and predicted onset using method A, B, C and D averaged over all available years (2009-2018)	6.1	3.7	4.7	2.2

Table 5 For each predicted monsoon withdrawal provided using method E (CP2 obtained with 0/-15 days normalized average of ^{7}Be activity concentrations) the corresponding difference from IMD monsoon withdrawal is given. Kerala is the reference region for monsoon onset. Correlation between IMD and ^{7}Be method for withdrawals dates is 0.73. Accuracy (trueness and precision) is defined by ISO 5725-1.

Year	IMD monsoon over Kerala withdrawal date	Method E cross point 2 (CP2)	Method E Predicted monsoon withdrawal	Method E difference between IMD monsoon withdrawal and predicted monsoon withdrawal (n. of days)
2009	268	240	281	-13
2010	302	250	291	11
2011	297	256	297	0
2012	292	255	296	-4
2013	294	248	289	5
2014	291	243	284	7
2015	301	253	294	7
2016	302	263	304	-2
2017	298	255	296	2
Correlation of cross point 2 (CP2 - method E) with IMD monsoon withdrawal			0.73	
Trueness: averaged difference from IMD withdrawal date over all available years (2009-2018) [n. of days]			1.4	
Precision: standard deviation of the difference between IMD withdrawal and prediction [n. of days]			7.2	

3.6.2. Data and predictions for 2018

For 2018, the predicted onset using the ^{7}Be trans-equatorial method is in accordance with the forecasted monsoon from IMD and the actual onset date: a monsoon of normal intensity with an earlier onset than the normal date, i.e. before June 1st. Later, after the monsoon has started, IMD reported the onset to have started in the south of Kerala by 25th May moving towards the northern border by the 28th of May. Methods A, B and C have been applied to determine the monsoon onset date for 2018 (Figure 41).

•Method A: with non-normalized moving average of past 30 days and a historical statistical average lead time of 266 days the onset warning time given by CP2 in 2017 indicates the 2018 onset on day #149 (29th May).

•Method B: with normalized moving average of past 15 days, CP1 2018 occurred on day #90 and the average monsoon lead time of 52 days, the forecasted onset date is day #142 (22nd May).

•Method C: with non-normalized moving average of past 30 days, the onset lead time given by CP1 in 2018 indicates the onset on day #137 (17th May).

•Method D: combined average onset date based on methods A, B, and C is day #143 (23rd May), only 2 days before from the actual onset date for 2018.

With an average monsoon withdrawal date on day #294 (21st of October), the monsoon is predicted to be more than a week longer and with higher intensity than last year. Eventually the monsoon in 2018 did withdraw on October 21st.
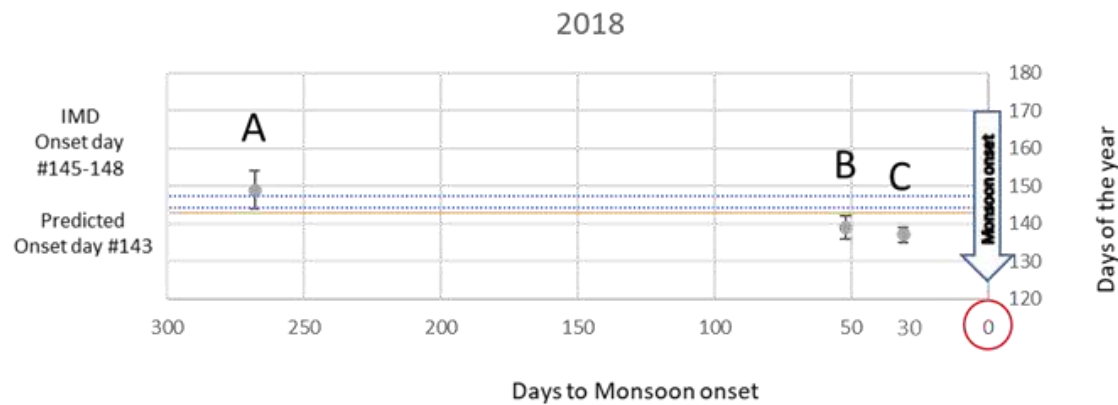
Figure 41. Method A, B and C results for the monsoon onset forecast of the year 2018. Orange dotted line indicate the resulting date (method B) built from A, B and C data points. (Terzi et al., 2019)

Further comparison with onset derived from objective and standardized indices such as OCI and HOW1 is necessary[2,105,107].

The current acquisition time for IMS radionuclide samples is three days. Therefore, in view of real time monsoon early warning, three additional days need to be considered for the calculation of ^{7}Be activity concentrations and included in warning time-lags.

Beryllium-7 timeseries from RUP61 and AUP04 for 2019 and 2020 validated the method and provided the monsoon onset prediction for the 11th of June 2019 and 28th of May 2020 respectively. CP1 occurred on 22nd of April (day #112) in 2019 and on the 6th of April (day #97) this year.

Although the arrival of the monsoon belongs to a small time-window (May-June) it is worth notice the difference an accurate prediction would make for the people affected. An example is presented in Figure 42. In dark grey the typical schedule for rice production. In light grey the current practice of the Indian Meteorology Department (IMD) based on local meteorological observations to announce their forecast of monsoon onset. In green the forecast based on the new trans-equatorial approach with radionuclide monitoring; as seen the forecast is improved over time with the approaching monsoon. For farmers an earlier warning may provide an important decision-making tool for rice management production. This is one example on how [7]Be monitoring data can be used to produce seasonal forecasts well in advance.
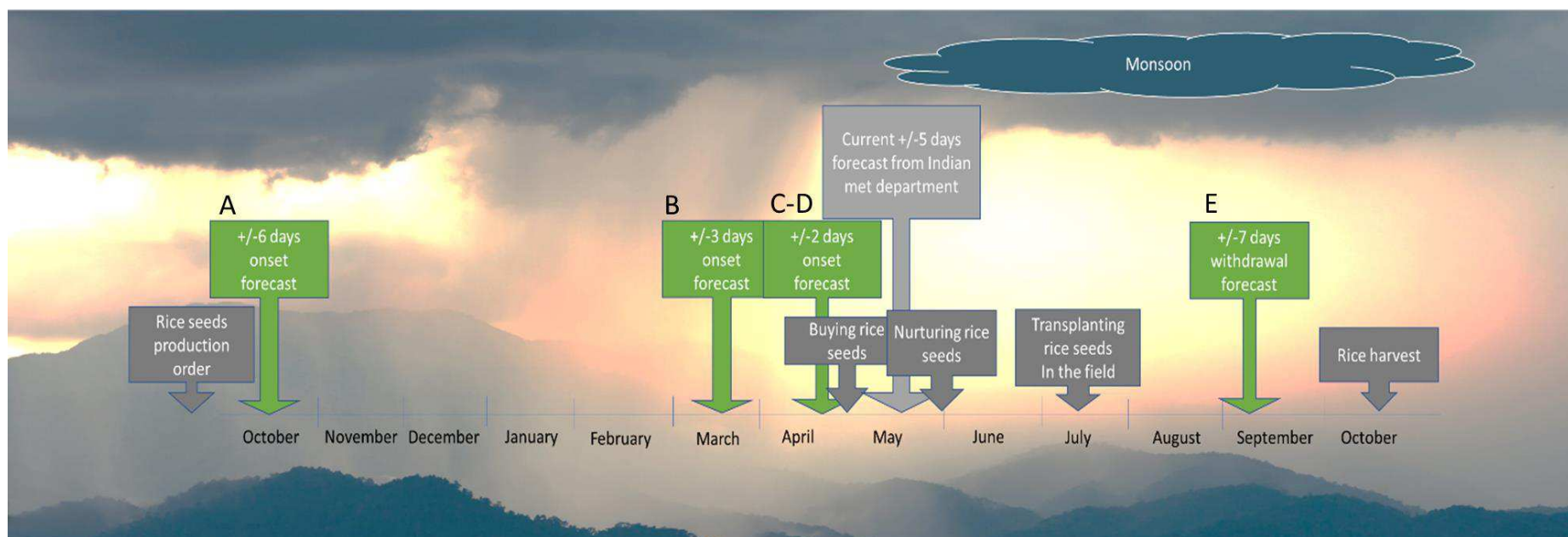
Figure 42. Timeline of Indian monsoon forecast using method A, B, C, D and E (green flowcharts) and timeline of rice production (dark grey flowcharts). Light grey flowchart shows when the Indian Meteorological Department release the monsoon forecast over Kerala. (Terzi et al., 2019)

3.7 Changes in atmospheric dynamics

This paragraph focuses on how some possible or likely effects of climate change such as heightening of tropopause, atmospheric blocking, slowing down of atmospheric circulation and extended summer periods can be indirectly monitored through [7]Be. According to the latest IPCC report[33], some of these effects can only be established with medium to low confidence.

Beryllium-7 concentration trends and changes during the last 10-20 years cannot be explained by variations of the Earth magnetic field or the solar irradiance. There is solid evidence that these modifications are rather related to changes in global atmospheric circulation patterns triggered by global warming. Expected effects of global warming are explained in Figure 43.
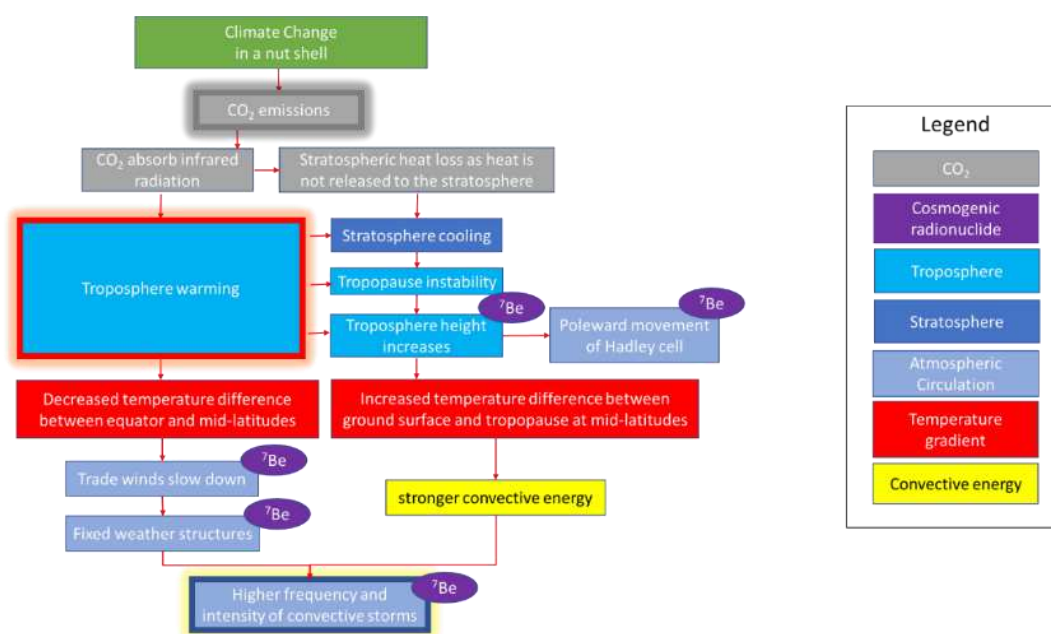
Figure 43 Flow chart illustrating the connection between CO_2 emissions to climate change patterns and the use of [7]Be as an indicator Terzi et al., 2020)

[7]Be and [22]Na concentrations at ground level depend on the tropopause height and prevailing atmospheric circulation[16,90,89,91] and are therefore a function of the measurement location, mostly the station latitude, and the time of the year. The activity concentrations are significantly influenced by systematic changes in the atmospheric circulation. Such ground-level concentration data can thus yield insights into key atmospheric processes.

Figure 44 presents the global surface temperature changes (red line) and the sun's energy that the Earth receives (yellow line) since 1880. The lighter/thinner lines indicate the yearly levels while the heavier/thicker lines show the 11-year average trends. Eleven-year averages are used to reduce the year-to-year natural noise in the data, making the underlying trends more obvious. The amount of solar energy that the earth receives has followed the sun's natural 11-year cycle of small increases and decreases with no net increase since the 1950's. Over the same period, global temperature has risen markedly. It is therefore unlikely that the solar activity has caused the observed global temperature trends over the past half-century.
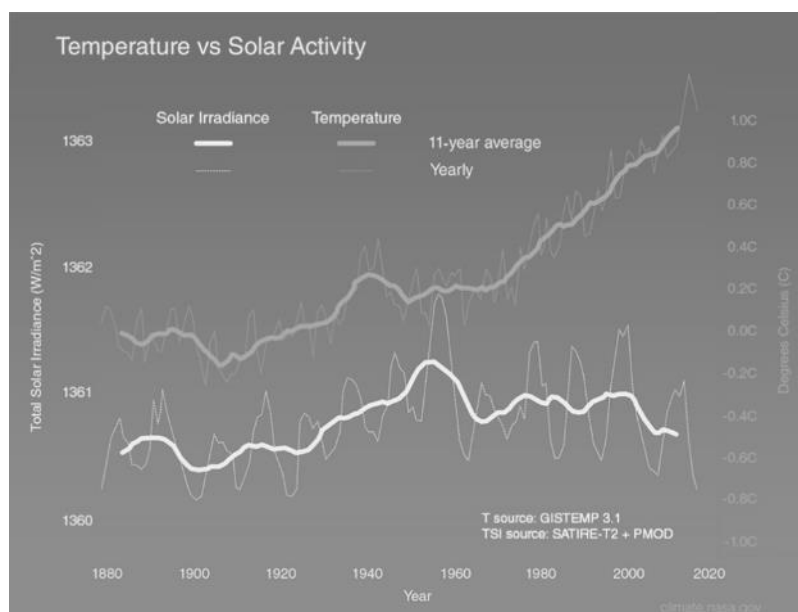
Figure 44. Global surface temperature changes (red line) and Sun's energy that Earth receives (yellow line) in watts (units of energy) per square meter from 1880. (NASA/JPL-Caltech, 2019)

Berylium-7 data measured over the last 20 years indicate that major changes in the atmospheric circulation are currently ongoing. Even though the time series are too short to make climatological assessments, there is strong evidence that these changes are influenced by progressive global warming on a decadal timescale. Natural causes to explain the observed [7]Be variations such as solar flux or the strength of the Earth's magnetic field act on either a different order of magnitude or at different time scales and thus cannot explain the observed trend.

This new monitoring method using [7]Be as an indicator for global atmospheric circulation may support topics marked as "known with lower confidence" in the latest IPCC report[33]. Although the data sets in this thesis cover less than two decades, this method provides some indication on how strongly global warming may influence the atmospheric circulation worldwide already

today. This may also indicate that the warming trend is more severe and rapid than many climate projections show, and that one cannot exclude that weather extremes predicted to occur between 2050 and 2100 already materialize during the next few decades.

The increase of global average temperatures and of the frequency of severe weather conditions such as floods, storms and droughts are directly attributable to the anthropogenic emissions of greenhouse gases[12,13,14,36,49,55,60,63,86]. The rapid growth of greenhouse gas concentrations in the atmosphere is leading to significant changes in global atmospheric circulation patterns, from poleward movements of atmospheric circulation cells, enhanced atmospheric blocking events, to troposphere breathing and global tropopause heightening at mid-latitudes[23,24,46,49,68,69,70,71,73,74,99,103,107,109].

Global atmospheric processes which are expected to change due to global warming can be indirectly observed by monitoring cosmogenic radionuclides. In this study, measurements of the ^{7}Be ground-level activity concentrations are used as indicator of vertical exchange and circulation patterns[16,26,31,66,67,89,90,91,98]. The analyses presented below, demonstrates how the time series of ^{7}Be activity concentrations at ground level are modified by five processes, namely:

a) Cosmic rays
b) Variations of troposphere heights
c) Poleward shift of the seasonal turning point of the Hadley cell (HFDZ)
d) Slowing down of atmospheric cell movements, and
e) Tendency towards static weather conditions.
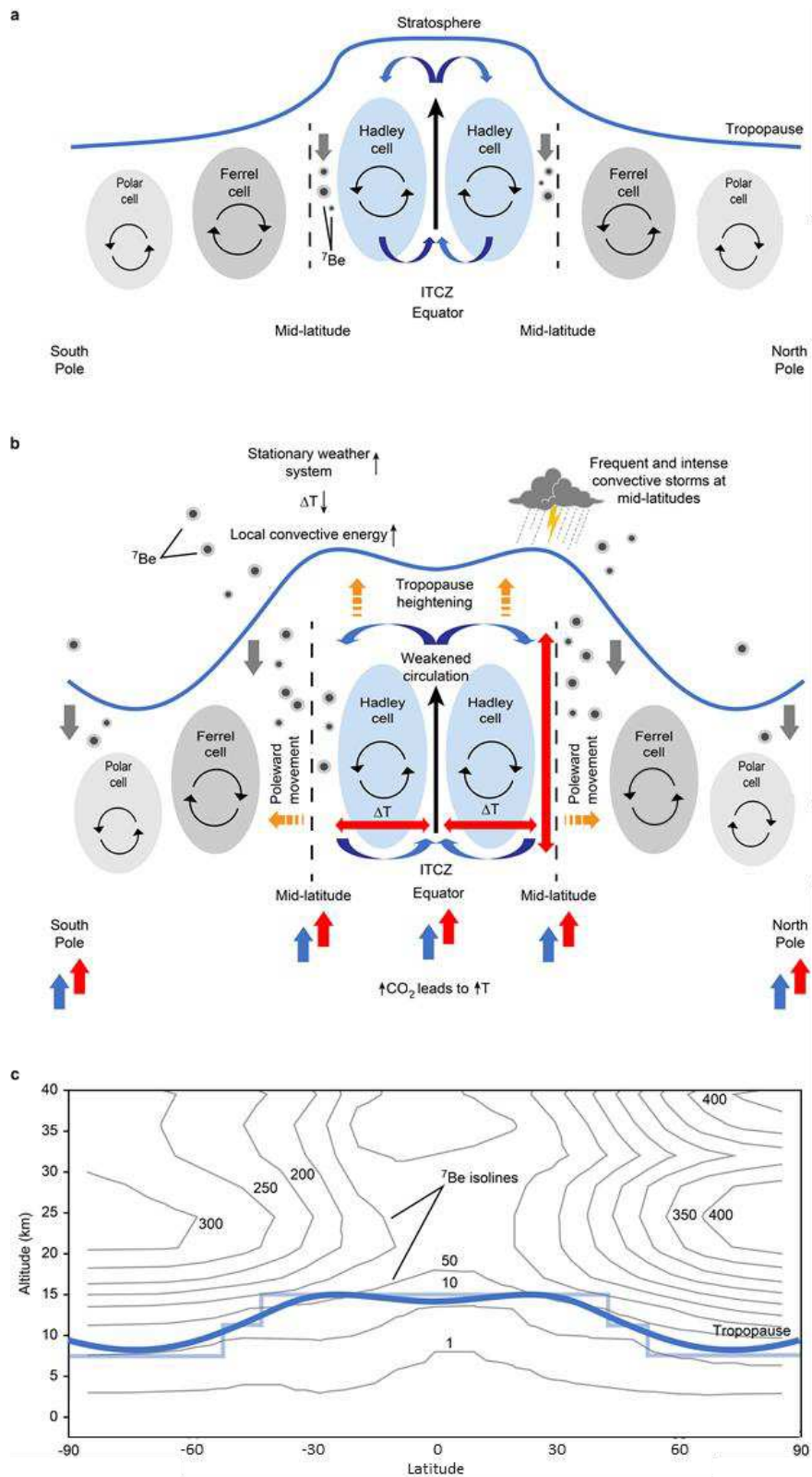
Figure 45. (a) Basic atmospheric cell circulation diagram of [7]Be being transported to the surface through STE in the mid-latitudes (HFDZ) and polar latitudes (PFCZ). (b) Global circulation changes linked to increase of CO_2. (c) Dependency between tropopause height (blue line) and [7]Be concentrations (Terzi et al., 2020)

Poleward shift not only refers to the northward movement of the Hadley cell in the northern hemisphere (or southward in the southern Hemisphere) but also the poleward movement of tropical and polar jet streams and the global Rossby wave circulation that governs the weather[36,49,60].

Figure 45 presents (a) basic atmospheric cell circulation diagram of [7]Be being transported to the surface through STE in the mid-latitudes (HFDZ) and polar latitudes[98]. (b) Global warming caused by increasing CO_2 concentrations[12,13,14,36,49] is expected to trigger the following changes in the global circulation: (1) tropopause height increase[69,70,71], (2) poleward extension of the Hadley cell[36,49,60], and (3) weakening of the atmospheric pressure difference between polar region and the subtropics and the related atmospheric circulation in the mid-latitudes due to the decreasing temperature difference [23,24,46,49,68,69,70,71,73,74,99,103,107,109]. Poleward extension and weakened circulation extend the area where cosmogenic radionuclides are detected and increase the period of radionuclide detection during summer months. In the mid-latitudes, weaker circulation and increased vertical temperature differences due to the rising of the tropopause have two effects: stationary weather system[74] and increased convective energy[55], resulting in more frequent and stronger convective storms[13,55]. Figure 35(a) and (b) are simplified with respect to the STE, as tropopause folding (or duplication) is not represented in spring (northern hemisphere) and its role in the STE[45]. See Figure 34 for flowchart representing step-by-step the process shown in Figure 35 (a) and (b). (c) The [7]Be concentration profile from Delaygue et al. (2015)[16] is showing the dependency between tropopause height (blue line) and [7]Be concentrations[16].

The analysis of the [7]Be time series provides important information on all four (b, c, d, e) aspects of global atmospheric circulations mentioned above. With this simple but previously unconsidered method, it is possible to track the atmospheric processes that are predicted to be modified as a consequence of global warming trends.

In a comparison of the annual averages of [7]Be concentrations with the annual average of cosmic rays, only 18 out of the 62 stations studied in this paper reveal a significant positive correlation ($\alpha=0.05$) for the years 2004 to 2018. The other stations indicate weak positive (37 stations) or even negative (7 stations) correlations not significant at the $\alpha=0.05$ level. At these stations the correlation is overprinted by atmospheric processes and due to the mixing of old and fresh air masses during transport[66,67]. After linear correction for the cosmic ray variations, the remaining variability reflects the influence of atmospheric processes and

decadal trends thereof, see Figure 46. Thirteen out of 62 stations confirm a significant (α=0.05) linear correlation between ^{7}Be and calendar year (Figure 48b). Eleven of these stations indicate a positive correlation with the steepest increases of ^{7}Be being observed at Okinawa, Azores, and Midway Islands. Two stations (Cocos Island and Zalesovo) show a significant negative correlation. Studying the corrected time series in Figure 46, two effects are highlighted: the troposphere breathing (up and down movement of grey dotted line) and the overall trend towards a heightening or lowering of the tropopause (continuous black line).

Figure 46 presents measurement stations with different trends. The first plot on the left displays all ^{7}Be normalized yearly average concentrations (blue line) which is the result of all 62 stations records. The global analysis clearly indicates the influence of cosmic rays; therefore, data needed to be corrected (grey line, secondary axis) to assess the weight of atmospheric circulation processes such as tropopause breathing, tropopause height variation etc. which are visible at each location.

Tropopause instability or breathing expose different frequencies and patterns depending on the station location. As mentioned by Hakuba et al (2019)[24] the troposphere breathing is influenced by seasonal, inter-annual, multi-annual variations associated with Brewer Dobson Circulation, Quasi Biannual Oscillation (QBO), El Niño Southern Oscillation (ENSO), etc.
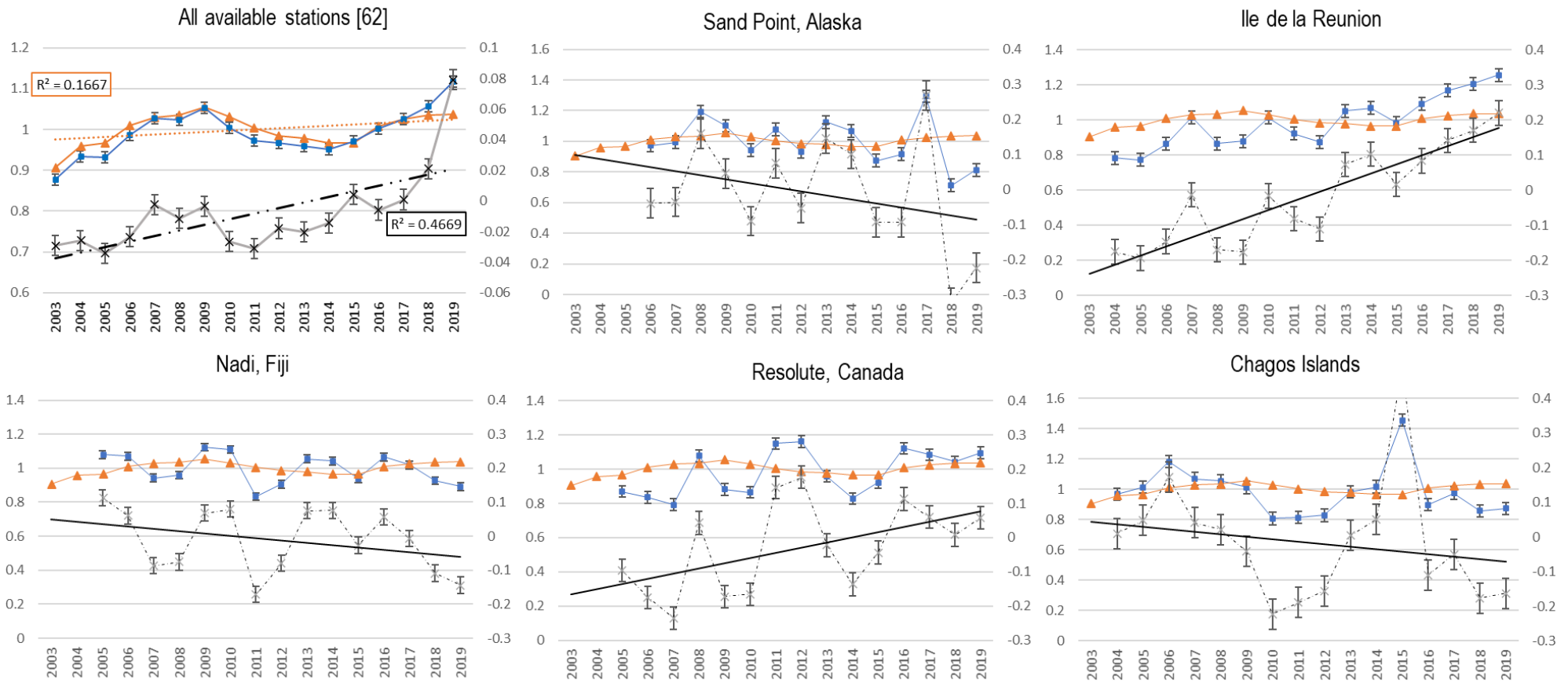
Figure 46. Examples of the correlation between yearly averages of ⁷Be and cosmic rays (orange line). Cosmic rays cycle dataset (IGY detector) is taken from http://cosray.unibe.ch/ (2019) (Terzi et al., 2020)

Besides the 11-year solar activity cycle, a systematic decrease of the Earth's magnetic field strength and a corresponding increase in cosmogenic radiation is being observed over the last 150 years. This effect accounts for a systematic increase of only +0.4 % in the [7]Be production over a decade[51,52] which is taken into account by the above described correction for the measured cosmic ray flux.

As mentioned initially if one takes all dependencies and variations into account, the observed trends in the cosmogenic radionuclide concentrations measured at ground level can be used as proxies to investigate changes in the global tropospheric circulation possibly triggered by climate change effects[33].

Figure 47 presents the development of the averaged and normalised concentration data for the selected stations, with the orange and darker bandwidths indicating above-average [7]Be activity concentrations. Stations exhibit phases of above-average concentrations followed by phases of below-average concentrations, resulting in a sinusoidal time series with a period of one year. The time series from stations in opposing hemispheres are phase-shifted by six months due to the simultaneous extension and contraction of the northern and southern hemisphere Hadley cells[89,90].This annual variation pattern is particularly visible in mid-latitudes where the stations are strongly affected by the HFDZ movement. For a given monitoring location in the mid-latitudes, the concentration rises when the HFDZ approaches from the equator and falls when the HFDZ retreats towards the equator. Such effect was even visible at monitoring locations not directly below the HFDZ pathway. This may be due to the horizontal transport of air masses at lower altitudes.
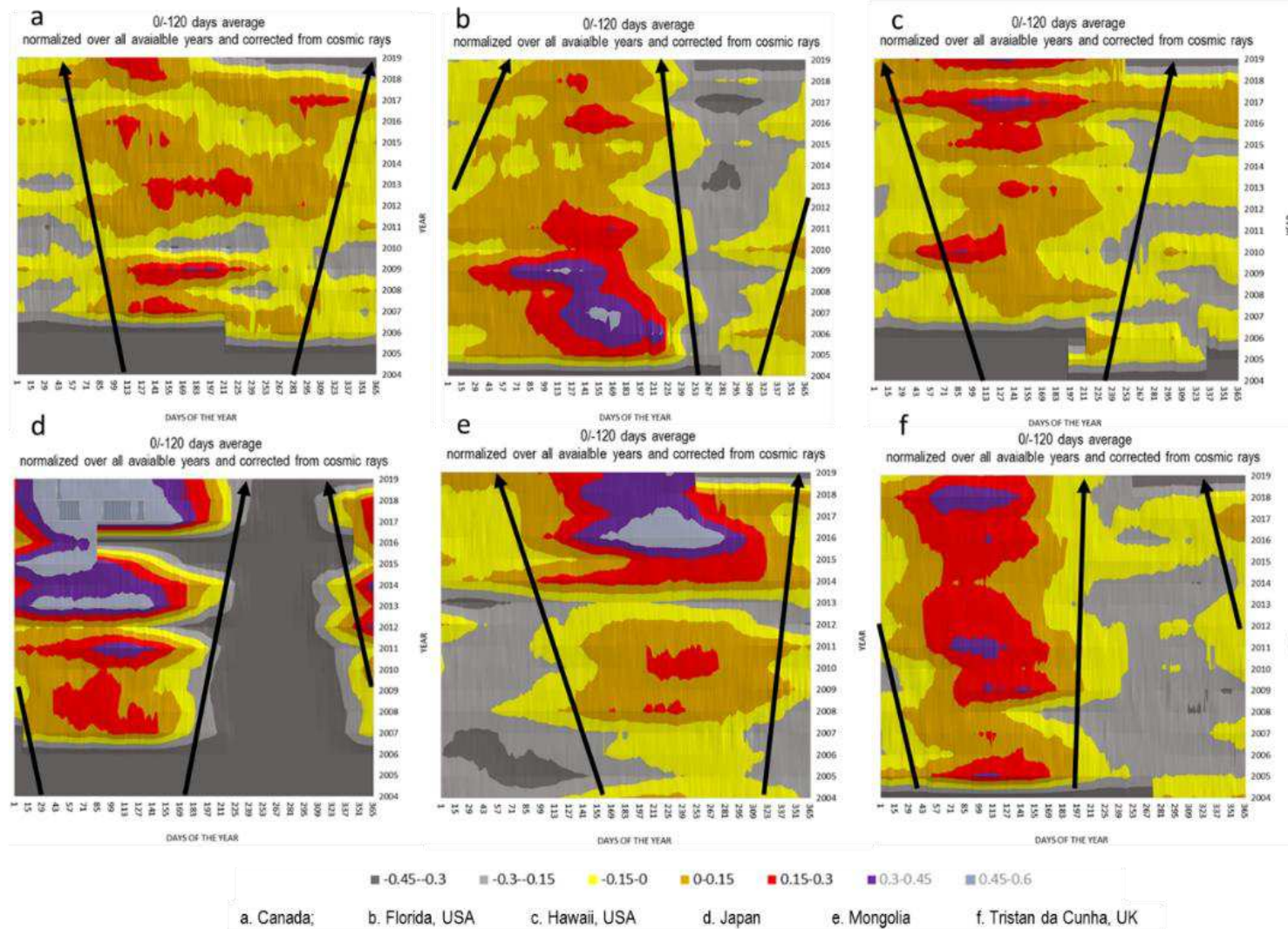
Figure 47. The development of the annual ^{7}Be concentration time series over the years at selected monitoring stations. (Terzi et al., 2020)

Figure 47 shows most long-term data sets of ^{7}Be concentration, like a, c, d, e, and f (Canada, Hawaii, Japan, Mongolia, Tristan da Cunha respectively), exhibited over the last two decades an extension of the high ^{7}Be season; i.e., the time period in which the ^{7}Be concentrations were above average. Some stations, like b in Florida and others in Zalesovo, Russia, and Rio de Janeiro, Brazil (not shown here), describe an opposing trend. Others like Cook Island and Guam (Pacific Islands located at low latitudes below 20 degrees) did not present much of a significant change over the past 16 years with a standard deviation of 5 to 6% for the whole time series (see Annex B). The black arrows indicate the trends; they are only for visual guidance. Stations located in mid-latitudes, e.g. Canada and Japan, illustrated a clear pattern, namely a gradual extension of the high ^{7}Be season (Figure 47); i.e., the annual period with above-average concentrations starts earlier and ends later in the season. Similar patterns were found especially along the sub-tropical zones in both hemispheres.

The station in Resolute, Canada, showed lower levels of ^{7}Be and the transit time to reach the yearly maxima increased over the years, which indicates that the general atmospheric circulation is weakening. Another example, the station in Stockholm, Sweden, demonstrated a 40% net increase over the past three years as well as 54 additional days with concentrations above average. In general, in most stations a similar increase in the ^{7}Be concentrations was measured.

3.7.1. Tropopause heightening

The tropopause is the thermally stable boundary layer between the troposphere and the stratosphere. The stable stratification inhibits air mass exchange between these two atmospheric layers. The tropopause height decreases from about 15 km in the equator region to about 7 km in the polar region. Observations have indicated that the tropopause height has been changing over the recent years, probably due to climate change processes[46,69,74]. Between 2001 and 2007, a height increase of 20–50 m/year has been measured at around 30–40 degrees latitude and at the poles, while a decline of 10–30 m/year has been measured around the equator and 60 degrees latitude[69,70,71,72]. However, these observations, obtained using radiosondes ascents, were not evenly distributed globally, were conducted for a limited time and are therefore subject to significant uncertainty.

The ^{7}Be concentrations increase with altitude in the troposphere and lower stratosphere[16,31]. Therefore, an increase in the tropopause height integrates areas of enhanced ^{7}Be concentrations

due to increased production into the troposphere. As vertical mixing within the troposphere is much stronger compared with STE, this causes an increase of the amount of ^{7}Be being transported to the surface, see Figure 45c.

Figure 48a displays the tropopause height trends directly measured with radiosondes re-analysis[71] in comparison with the growth rate of the ^{7}Be concentrations at the ground level for different latitudes. The relative growth and decline of a latitudinal profile for ^{7}Be (2017) and radiosonde re-analysis (2001-2007) datasets shows a correlation of 0.8, indicating a causal relationship between the ^{7}Be trends and the observed tropopause height changes. Tropopause trends presented here are in agreement with the work of Santer et al (2004)[69]. A global interpolation of ^{7}Be concentration from 2003 to 2019 as troposphere breathing or tropopause instability is available in Annex B.

The datasets from radiosonde re-analysis and ^{7}Be are from different periods as data from 2001 to 2007 are not available for all the stations needed to build the latitudinal profile shown in Figure 48a.
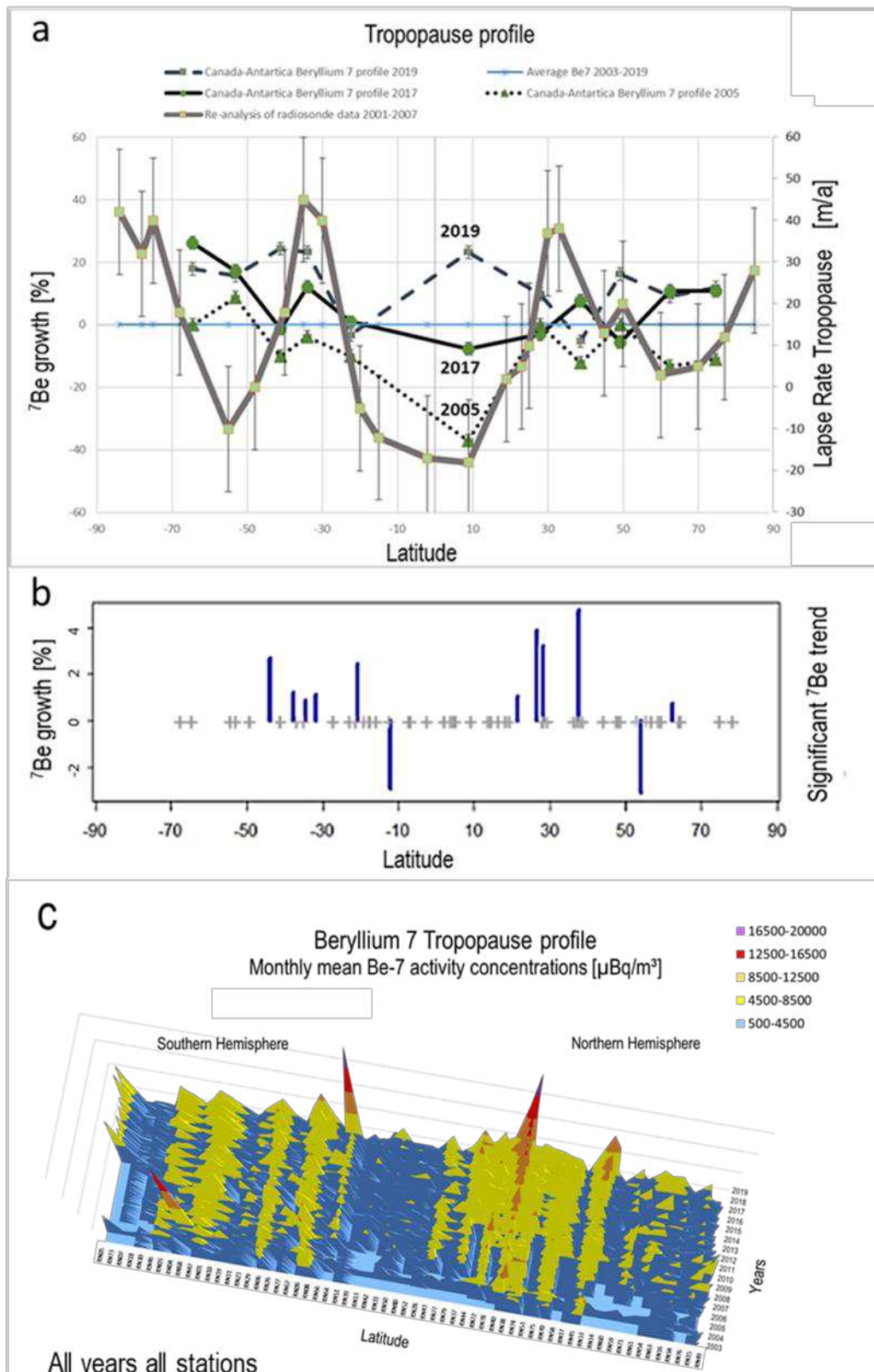
Figure 48. a) relative increase/decrease of ^{7}Be concentrations trend versus the radiosonde data. b) Annual ^{7}Be growth for stations with significant (α=0.05) trends (2004-2018). c) ^{7}Be monthly mean from all stations for all available years. (Terzi et al., 2020)

Figure 48 presents (a) the relative increase/decrease of ^{7}Be concentrations for varying latitudes correlate with radiosonde measurements of the tropopause height trends. The ^{7}Be data was based on measurements from 2003 to 2019; the radiosonde data was based on aggregated measurements from 2001 to 2007 (Schmidt et al., 2008)[71]. The applied error margin was 2% based on data uncertainties for the ^{7}Be concentration; for the re-analysis of the radiosonde data, it was ±15 m/a based on the aggregation of data in different latitudinal resolutions of 5°–10° (Schmidt et al., 2008). The 2019 ^{7}Be profile is especially interesting because of its uncommon increase at the equator, possibly indicating a change in the tropopause profile. This may also explain why hurricane Dorian (August 2019) was so powerful and slow at the same time.

Figure 48b displays the ^{7}Be growth rate of all stations with a significant (α=0.05) linear trend over the past 7-14 years compared to radiosonde reanalysis data. Plus-signs indicate the position of all stations included in this study. The highest increases are found at mid-latitudes corresponding with the locations of tropopause heightening.

Figure 48c displays ^{7}Be monthly mean for all station for all available years showing the correlation with tropopause trend presented by Schmidt et al (2008)[71] and reproduced in Figure 48a (grey line).
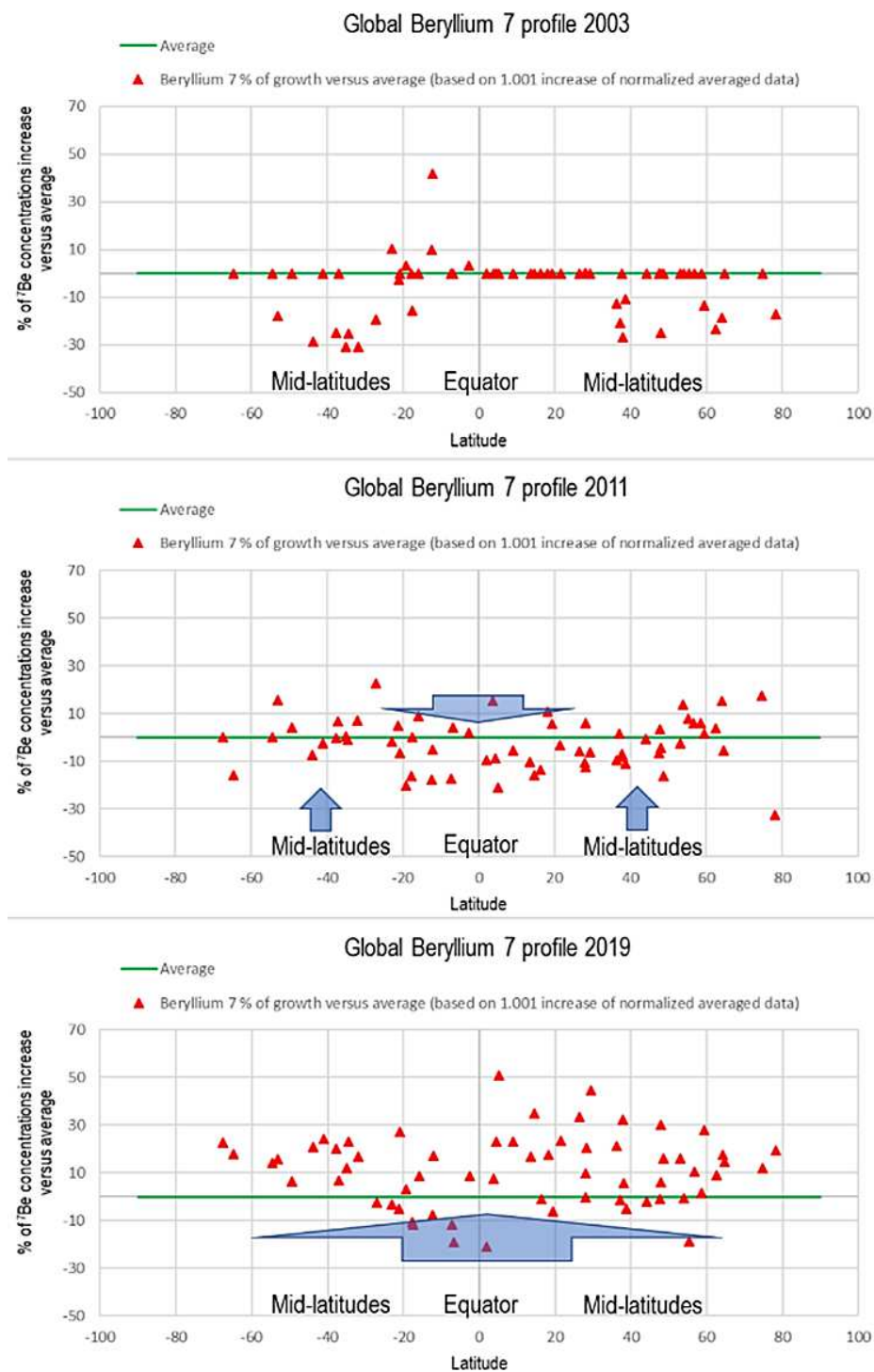
Figure 49. [7]Be growth trend at all 62 stations in 2003, 2011 and 2019. Supplementary information related to Figure 48. (Terzi et al., 2020)

Figure 49 displays the [7]Be growth trend at all stations in 2003, 2011 and 2019. The displayed dataset has not been corrected from cosmic rays. In 2003 the concentration at mid-latitude is below average, in 2011 mid-latitude concentrations rise above average while concentrations

decrease at the equator. These results are consistent with re-analysis of radiosonde measurements, which show tropopause increase at the mid latitudes while a decrease along the ITCZ. In 2019 the ^{7}Be growth rate is increasing globally with the exception of a few locations.

Global warming is also associated with decreasing lower-tropospheric temperature differences between the equator and the polar region (enhanced polar warming), which may cause a weakening of the related geostrophic (westerly) circulation. Furthermore, it affects the poleward movement of the HFDZ. While the former may lead to more stable weather patterns, such as the blocking situations discussed below, the latter extends the time period as well as geographical area where high ^{7}Be concentrations are observed. The growth is greater in the southern hemisphere and lesser in the northern hemisphere, as indicated by the data. In general, the global ^{7}Be data correlated with the results from the radiosonde network. Therefore, global ^{7}Be monitoring provides an opportunity to support the tropopause height monitoring efforts. More information on the role of intensified STE associated with this process can be expected from ^{22}Na /^{7}Be ratios described in the following paragraph.

Figure 50 shows tropopause height calculated from gridded monthly global positioning system radio occultation (GPS-RO) data versus the ^{7}Be concentrations at the same location (equal coordinates). The tropopause profile is built on monthly average records of GPS-RO [m] (left plot) and ^{7}Be [µBq/m³] (right plot). GPS-RO data have the same GPS coordinates as IMS stations locations. GPS-RO are retrieved temperature profiles generated by satellites. All available years are plotted. The coloured scale is based on normalised data obtained by dividing absolute values with the overall time series average. Stations location correspond to: ARP01 Argentina, PAP50 Panama, PHP52 Philippines, USP72 Florida USA. white areas indicate periods of not-available data.

In both cases GPS-RO and ^{7}Be data are not smoothed additionally. Each location indicates a high degree of correlation (PCC between 0.6 and 0.9) between the 2 parameters confirming connections between tropopause and ^{7}Be. The standard deviation is low at the mid latitudes and increases at the equator and at the very high latitudes, those areas where ^{7}Be is most affected by wash out. Years with lower correlation values (PCC <0.3) need to be further investigated as possibly associated to additional drivers such as advection or stratospheric-tropospheric exchange.
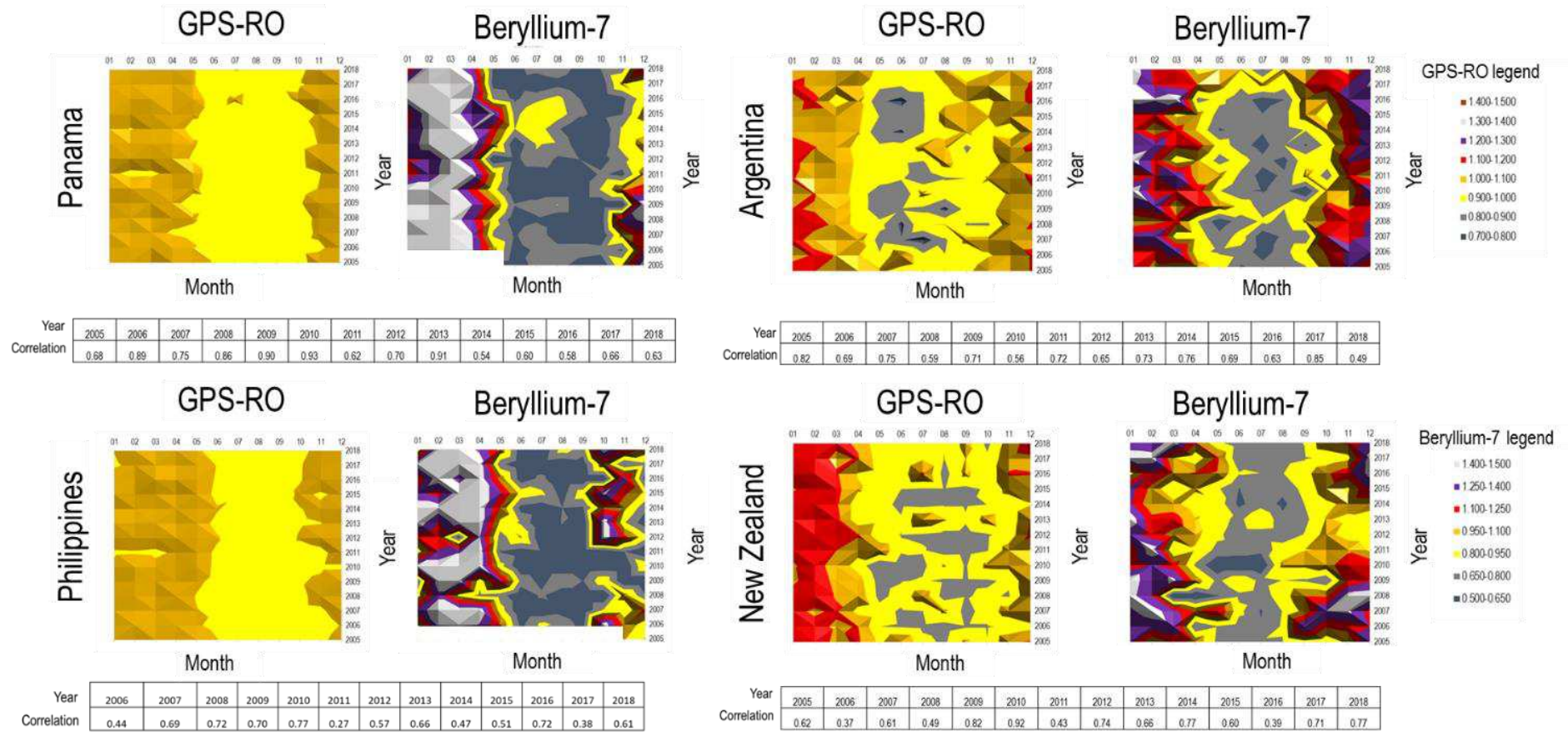
Figure 50. Examples of IMS station locations from different regions worldwide where tropopause profile based on GPS-RO data is compared with [7]**Be time series. Tropopause profile is built on monthly average records of GPS-RO [m] (left) and** [7]**Be [µBq/m³] (right). GPS-RO data have the same GPS coordinates as IMS station locations. GPS-RO are retrieved temperature profile generated by satellites. All available years are plotted. The coloured scale is based on normalised data obtained by dividing absolute values with the overall timeseries average. White areas indicate periods of n/a data. (Terzi et al., 2020)**

3.7.2. Slowdown and poleward movement of the HFDZ

Changes of atmospheric cell progression, in term of speed and latitudinal extension are visible though isotopic ratios (^{22}Na/^{7}Be) and single ^{7}Be timeseries as presented in Figure 51 and Figure 52. As seasons have characteristic isotopic ratios due to the associated position of the circulation zones, isotopic ratios of ^{22}Na and ^{7}Be can also indicate the circulation trends.

The 19-year time series from Switzerland shows an overall positive trend (i.e. increasing contribution of stratospheric air), however, with relatively high year to year variability (Figure 51).
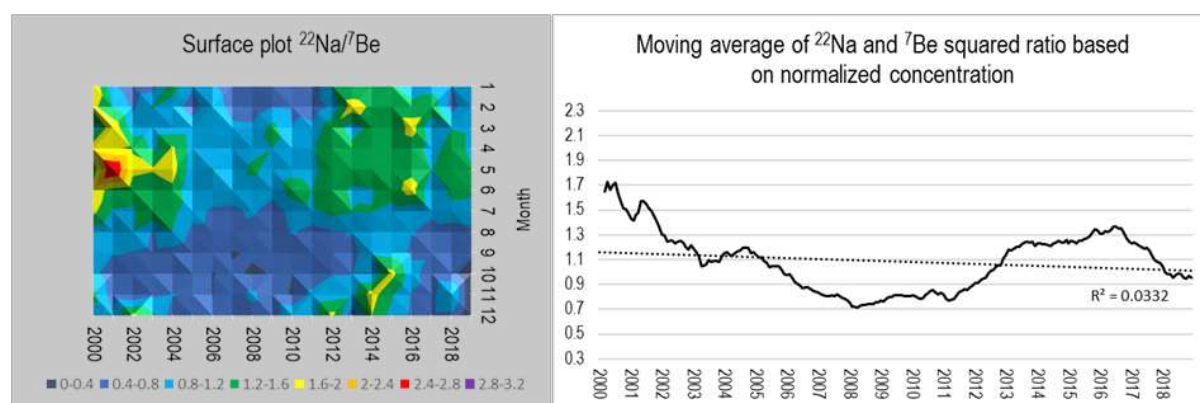
Figure 51 Change of atmospheric cells progression is also visible through isotopic ratio change of ^{22}Na and ^{7}Be over time. Data from Swiss stations have been provided by P. Steinmann from BAG Bern, Switzerland. (Terzi et al., 2020).

The surface charts show the change of atmospheric cells progression visible through isotopic ratio change over time. What the figure displays is how much the radioisotope ratio seasonal gradient (^{22}Na versus ^{7}Be) varies over time, meaning that a seasonal peak is the expression of a fast transition of the atmospheric cell interface zone over the point of measurement (IMS Station). In Switzerland, where the plotted data come from, that typically happens during the pre-summer season, end of April until beginning of June. A plane like feature of the seasonal profile indicate a slowing down of Hadley cell progression, meaning more time is needed to transit to a different ratio value. Between 2000 and 2018 a gradual transition from peak to plane is observed, possibly indicating a lower speed of cell progression over Switzerland. The right graph displays the same dataset where decreasing speed trend (linear trend line) is indicated by

the dotted black line. Looking at the ^{22}Na/^{7}Be ratio provides a better indicator for the origin of air masses, since the ratio is very sensitive to the height of production with much lower values in the lower stratosphere than in the upper troposphere. Unfortunately, due to the much lower abundance of ^{22}Na (activity ratio of ^{22}Na/^{7}Be ratio is approximately 10 to 4) no global ^{22}Na dataset is available comparable to the here discussed ^{7}Be data.

Although timeseries would need to be at least 30 or 40 years long before any climatological assessment can be made, the seasonal gradient of the isotopic ratio has decreased over time possibly suggesting a weakening of the circulation on a decadal time scale.

The time series of the ^{7}Be concentrations in Figure 52 (and ^{22}Na for Figure 51) indicate to be affected by the changing seasonal movement of the HFDZ. Along with the increasing height of the tropopause, the Hadley cell expands not only vertically but also in the latitudinal direction, accompanied by a slowing down of the HFDZ[112]. Over the years, this effect was reflected in the time series by a prolongation of the periods with high isotope concentrations (Table 14). Most of the locations followed this pattern, as indicated by the black continuous lines in Figure 47.

The ongoing extension of the high ^{7}Be season is, therefore, likely directly associated with longer and warmer summers. The Hadley cell is susceptible to temperature effects as it is driven, like the polar cells, by the thermal circulation of warm and cold air and the creation of high- and low-pressure areas. The poleward extension of the HFDZ movement, (together with a widening of the tropical circulation, poleward shift of the tropospheric jet streams) can be linked to global temperature increase issues.[12,13,14,73,83,100,110]

3.7.3. Static weather patterns

Comparing the annual curves of ^{7}Be at a given station indicated that the observed shape of the curves has been significantly changing over the years. While in the early years of the available data sets—i.e., the 2000s—the curves showed rather smooth and steady increases and decreases, closely resembling an idealized sine curve, the more recent data showed plateaus where the ^{7}Be concentration stayed roughly constant for a few days or weeks per year (see Figure 52).
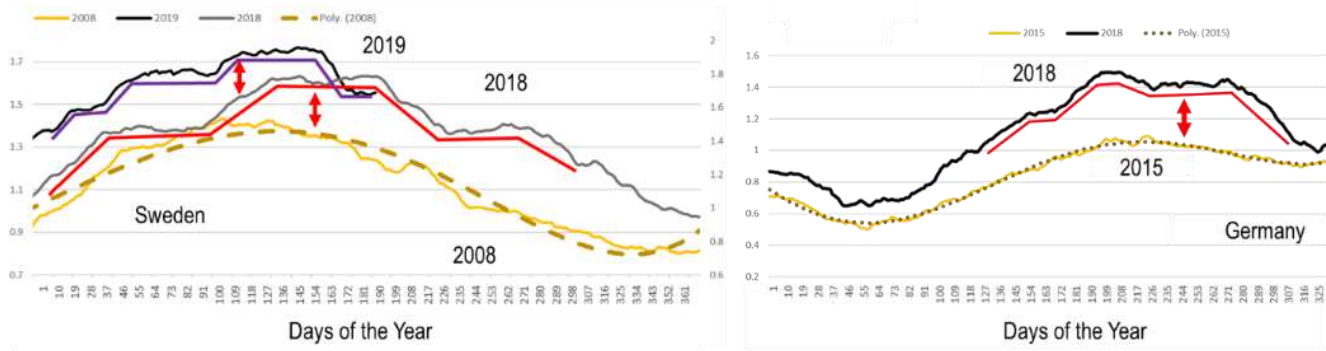
Figure 52. Plateau features present in ⁷Be data recorded at SEP63, Sweden (left) and DEP33 Germany (right). Red arrows indicate the increasing levels of ⁷Be concentrations over the years. (Terzi et al., 2020)

Figure 52 presents two important effects: heightening of the tropopause with higher concentrations in 2018 and 2019 with respect to previous years (Year 2008-Sweden, Year 2015-Germany), and change in the sinusoidal progression of the HFDZ. The tilting of the Earth axis makes the progression of the HFDZ follow a sinusoidal function (year 2008, Figure 52). With decreasing temperature differences between the equator and mid-latitudes, the circulation slows down, and one sees higher frequencies of stalling situations, plateaus, or step features where the interface zone seems to pause its latitudinal movement [46,49,110].

The station in Stockholm, Sweden is a good example for ⁷Be growth, extension of the warmer period, and plateau features, with a transition from a rather smooth, sinusoidal curve (2008, continuous yellow line with dotted sine trend line) to steps and plateaus (2018, continuous grey line and 2019, continuous black line). Right plot: Freiburg, Germany, indicated similar patterns (red continuous line). The weather in Stockholm during May and June 2018 which correspond to the middle plateau feature (left plot) was persistently hot and sunny with peaks of 29 degrees Celsius.

These stalling conditions facilitate static weather patterns which correlate with the deceleration of the general circulation [23,33,60] and the increase of convective storms at mid-latitudes over the past few years[36,48,63,110].

Static weather patterns refer to the Rossby waves in the mid-latitudes: as one sees the tropical cell progressing more and more towards the Pole in summer time, larger and larger areas in the mid-latitudes get sub-tropical in summer time. Atmospheric blocking on the other hand is a

feature of the jet stream that enhances the meandering of the Rossby wave which eventually gets in a stable position over weeks.

A warmer and higher tropopause along with a weaker westerly circulation would cause more tropical weather during summertime as associated with more steady weather situations. Longer episodes of large-scale atmospheric blocking and high-pressure areas with low pressure gradients have been frequently observed globally over the last few years.

Although severe weather and economic losses are not directly linked to ^{7}Be we can make use of cosmogenic radionuclides to improve efficiency in determining overall trends of extended summers and static weather for each single location. Static weather patterns are connected to higher frequency of convective storms and have a financial impact. The fraction of economic losses caused by severe convective storms in Europe with respect to all natural hazards combined went from 26% between 1989 and 2017 to almost 40% between 2003 and 2017[55]. The trend towards persistent static weather patterns is in agreement with the observations (plateau features) at the German and Swedish stations (Figure 52).

A majority of the stations show an extended high-^{7}Be season in recent years, especially from 2015 onwards, as shown by examples in Figure 52. By calculating how much time it takes to reach its yearly maximum at each station (which is the peak of ^{7}Be concentration per year when HFDZ is closest), it is possible to check whether the progression speed of the convergence zone has changed. Between 2003 and 2019, the progression clearly slowed down. The average of the ^{7}Be growth and extension period of growth for the past three years in all the stations indicated a prolongation of the summer season by around 1 month and a generalised deceleration (slower transit time) of circulation, producing a delay of 3 weeks to reach the ^{7}Be maximum worldwide (Figure 53).
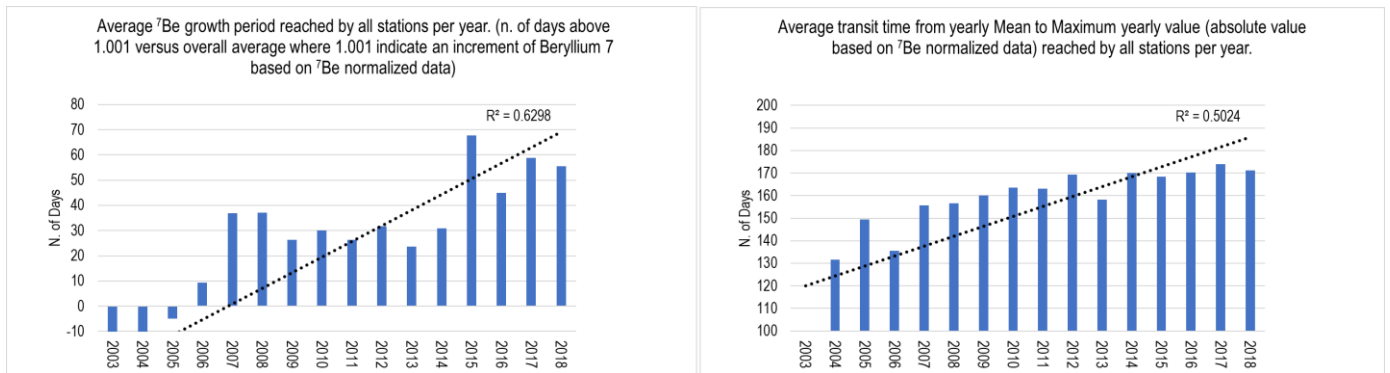
Figure 53 ⁷Be growth versus average (left) the increase in the n. of days required per year to reach the maximum ⁷Be threshold from the yearly mean baseline (right) (Terzi et al., 2020)

In Figure 42 the left chart shows the global ⁷Be growth versus average with a clear positive linear trend marked with a black dotted line (62 IMS stations considered, for details please see

Table **1**). The right chart shows, based on the same 62 stations, the increase in the number of days required per year to reach the maximum threshold from a baseline of the yearly mean. The trend is positive which suggests a weakening of cell progression and therefore suggests a slowing down of the general circulation. The presented dataset has been corrected from cosmic rays.

As discussed above, the trends of increasing ⁷Be concentrations (Figure 54) extended periods of high concentrations and growing transit times can be best explained by changes in large-scale atmospheric circulation patterns, possibly associated with the continued increase in greenhouse gas concentrations[30].

In Figure 54 the interpolation does not contain meteorological information and is only to help visualize the global increase of ⁷Be concentration in the last 10 years. Interpolation is based on multilevel b-spline with cell grid size of 1 degree using ⁷Be values from 62 IMS stations (green stars). The black and white plot presents the difference between 2019 and 2009: the darker the bandwidth, the stronger the increase (higher ⁷Be concentrations).

Further analysis is needed to build a comparative scale between the temperature and increase of ⁷Be as indicator. In fact, if ⁷Be observation data would be assimilated, weather models with integrated simulation of ⁷Be production could assess the precision of this monitoring method. Furthermore, longer time series are needed to better distinguish between decadal-scale and longer-time cyclic circulation variations and the systematic effect of global warming.
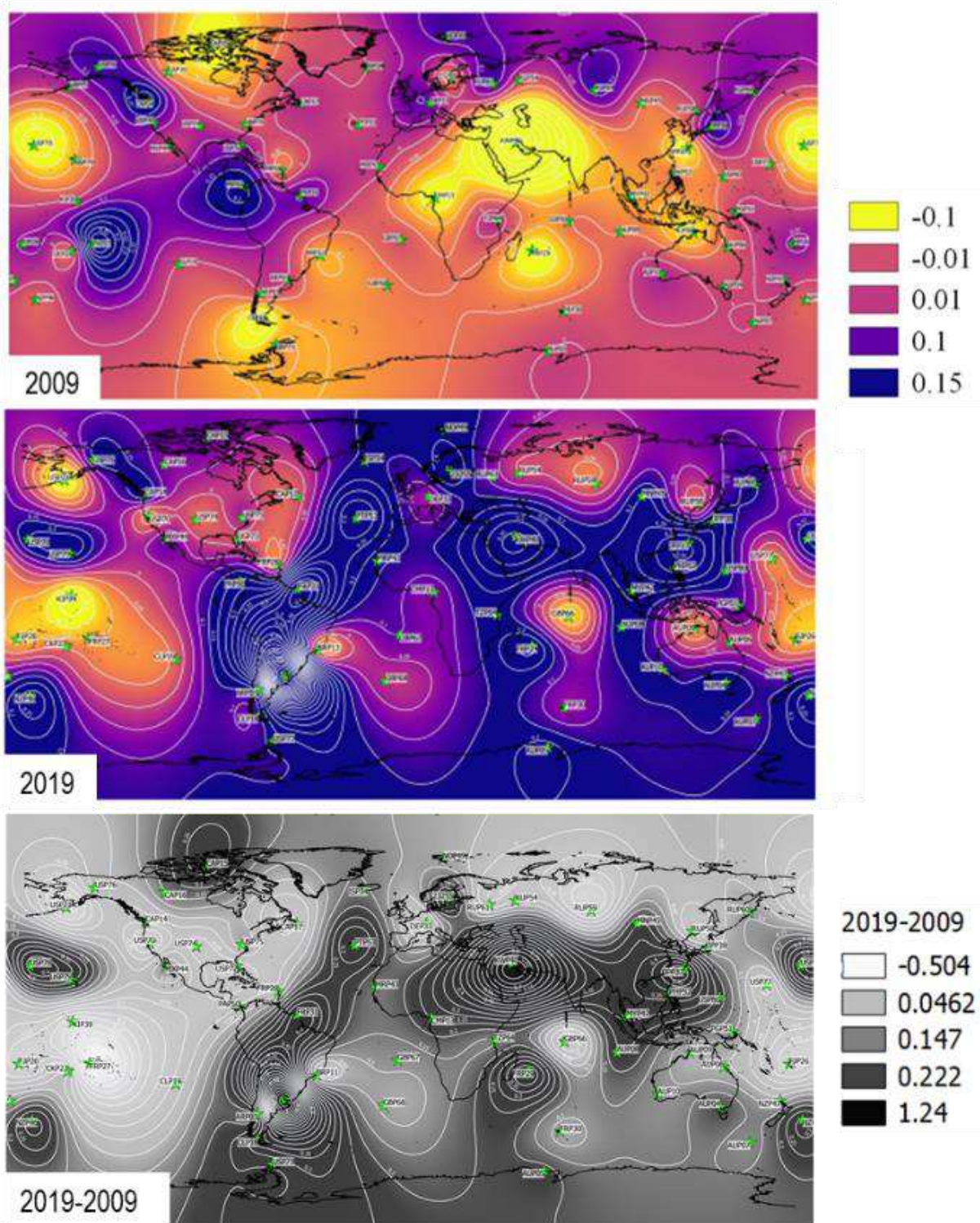
Figure 54. Yearly normalized averages of ^{7}Be data for 2009 and 2019 corrected from cosmic rays. (Terzi et al., 2020)

Summary and Conclusions

Meteorological transport mechanisms can be observed and derived using ^{7}Be as an atmospheric tracer. ^{7}Be is one of the sampled particle-bound natural radionuclides. It decays with a 53.2 days half-life and is largely produced in the UTLS region as a result of spallation of nuclei of atmospheric gases, mainly oxygen and nitrogen. Production rates are approximately twice as high in the stratosphere as in the troposphere. Once produced, atoms of this element attach to aerosol particles and are transported by them. Aerosols are transported by winds and redistributed vertically by gravitational sedimentation and are ultimately removed by wet and dry deposition in the lower troposphere.

^{7}Be is removed from the atmosphere by these mechanisms in addition to its radioactive decay. Concentrations of ^{7}Be vary from the order of hundreds mBq/m³ to tens mBq/m³ between lower stratosphere and upper troposphere, surface air measurements are a few mBq/m³ worldwide. With the coverage of ^{7}Be in surface air all around the globe, its unique source and sink characteristics, ^{7}Be is a suitable tracer for atmospheric dynamics.

It has been shown that ^{7}Be is generated steadily and its production increases as it approaches the poles, while maximum concentration levels are found at mid-latitudes of the troposphere which makes its transport a good indicator of STE. ^{7}Be production rate is not only dependent on the altitude in the atmosphere but undergoes temporal variation over the 11-year solar cycle and exhibits latitudinal variation due to the deflection of incoming cosmic-rays as the earth magnetic field is stronger above the equator.

Worldwide ^{7}Be concentrations on ground level follow an annual cycle because its transport in the atmosphere is regulated as any aerosol by the seasonal atmospheric processes.

The database of global ^{7}Be observations presented in this thesis may contribute to reduce these uncertainties. Especially ground based, worldwide observations of ^{7}Be over a long period can be analysed as a time series and cross-correlated with large-scale atmospheric circulation dynamics. The radionuclide network of the International Monitoring System collects the

environmental activity concentration of selected tracers for over 15 years and built up a unique and powerful dataset that can be analysed for global patterns such as spatial and seasonal variations.

Maps of observed ^{7}Be variations presents indications of atmospheric cell migration such as Hadley, Ferrel and Polar cells. Previous studies used data from IMS stations to correlate ^{7}Be trends to atmospheric patterns but on a local or regional scale. The work presented in this thesis describe how, for the first time, a map of worldwide ^{7}Be near-surface concentrations is reconstructed using data from IMS radionuclide stations.

To study the global dataset in a systematic way, the average values of each station are redistributed into a global grid. Each grid displays the position of convergence zones based on ^{7}Be concentrations worldwide during a specific month, a rather constant pattern that repeats each month with small modulations. Normalized values highlight the difference between each modulation at a given month.

As ^{7}Be is mainly created in the UTLS region, its time series indicate atmospheric cell shifts. Findings can be presented on correlation between ^{7}Be global patterns with intertropical convergence zone, sunspots, tropopause folds, El Niño Southern Oscillation, sudden stratospheric warmings, solar flares, Quasi Biannual Oscillation and monsoons worldwide. ^{7}Be is a vertical downward influx tracer that has potential to be used as a new parameter for seasonal weather forecast and climate change monitoring.

The close relationship between Hadley-Ferrel cell convergence zone and Monsoons makes ^{7}Be a reliable indicator for monsoon onset and withdrawal forecast. Time-series analysis of ^{7}Be activity concentrations at different monitoring stations could serve as an early warning index for monsoon regions worldwide with 2 months warning-time prior to the monsoon onset. Focus of this research is on monsoon forecast accuracy versus early warning time and how much deviation improves from a multi-year fit, how precision changes as a function of warning time and what are these shifts produced by.

The method allows longer forecast lead times and improved accuracy compared with traditional methods currently utilized based on the statistical analysis of wind, precipitation, pressure, temperature and humidity data. This provides significantly improved planning opportunities for agriculture, water management, emergency management, public health

management, and logistics. In India, where rice production is an important part of the economy and food supply, the monsoon is a driving force for the harvest. Bad water management is the main cause for low crop yields. Rice fields need huge amounts of water for flooding to remove weeds and to let the rice grow. The preparations for rice cultivation and flooding would also benefit from this capability to forecast the monsoon onset and duration.

An accurate monsoon forecast of eight months helps seed producers to plan the right amount of rice seeds to produce for the following monsoon year. An accurate forecast of two months or one month helps farmers decide how much to invest in quality and quantity of seeds to ensure higher yields and income.

Finally, further analysis also suggests that patterns frequently being associated with global warming, such as weakening of the general circulation, tropopause height changes and poleward movement of the Hadley cell can also be monitored trough tracers like [7]Be. In fact, this radionuclide indicates that climate change phenomena cannot be mainly driven by solar flux or earth magnetic field. The main driver for extended summer periods, static weather patterns, weakening of westerly winds at the mid latitudes is global warming due to rising CO_2 concentrations.

Near-surface measurement of cosmogenic radionuclide can shed light into large-scale global circulation modifications discussed in the most recent IPCC assessment report as having occurred with low to medium confidence and can help addressing outstanding challenges in atmospheric circulation research by integrating a new perspective across the disciplines of environmental radiation monitoring and meteorology. Beryllium-7 methods here presented find their strength not as substitute but in the combination to other techniques already in use.

List of Figures

List of Tables

Bibliography

1. Akritidis D., Pozzer A., Zanis P., Tyrlis E., Škerlak B., Sprenger M. and Lelieveld J. Tropopause Folds Over the Eastern Mediterranean and the Middle East in EMAC Simulations: Implications for Summertime Tropospheric Ozone. Springer Atmospheric Sciences, DOI 10.1007/978-3-319-35095-0_139 (2017)

2. Alessandri A., Borrelli A., Cherchi A., Materia S., Navarra A., Lee J., and Wang, B. Prediction of Indian Summer Monsoon Onset Using Dynamical Subseasonal Forecasts: Effects of Realistic Initialization of the Atmosphere. Mon. Wea. Rev. 143, 778–793 (2015)

3. Ananthakrishnan, R., and M. K. Soman. The onset of the southwest monsoon in 1990. Curr. Sci. 61, 447–453 (1991)

4. Arkian F., Meshkatee A., Bidokhti A. A. The effects of large-scale atmospheric flows on berylium-7 activity concentration in surface air, Environ Monit Assess 168:429-439. DOI 10.1007/s10661-009-1124-1(2010)

5. Baldwin, M.P., Gray L. J., Dunkerton J., Hamilton K., Haynes P.H., Randel W.J., Holton J.R., Alexander M.J., Hirota I., Horinouchi T., Jones D.B.A., Kinnersley J.S., Marquardt C., Sato K., Takahashi M.. The quasi-biennial oscillation, Reviews of Geophysics, vol. 39. (2001)

6. Baroni M., Bard E., Petit J. R., Magand O. and Bourle`s D., Volcanic and solar activity, and atmospheric circulation influences on cosmogenic 10Be fallout at Vostok and Concordia (Antarctica) over the last 60 years. Geochim. Cosmochim. Acta. 75(22), 71327145. DOI: 10.1016/j.gca.2011.09.002 (2011)

7. Błażej S. and Mietelski J. W., Cosmogenic Na-22, Be-7 and terrestrial 137Cs, 40K radionuclides in ground level air samples collected weekly in Kraków (Poland) over years 2003–2006. J Radioanal Nucl Chem. 300(2): 747–756. (2014)

8. Bollhöfer, A., Schlosser C., Variability of atmospheric Krypton-85 activity concentrations observed close to ITCZ in the southern hemisphere, Journal of Environmental Radioactivity 127, 111-118 (2014)

9. Boos W.R. Where Monsoons Are Found. World Monsoons. at http://worldmonsoons.org (2018)

10. Burnett J.L., Davies A.V., Beryllium activity at Comprehensive Nuclear-Test-Ban-Treaty stations hosted by the United Kingdom. DOI: 10.1007/s10967-014-3122-1 (2014)

11. Climate file 2: Monsoon Onset and Withdrawal, Monsoon dates. Department of Hydrology and Meteorology at http://www.dhm.gov.np/climate/ (2018)

12. Cohen J., Screen J. A., Furtado J. C., Barlow M., Whittleston D., Coumou D., Francis J., Dethloff K., Entekhabi D., Overland J. Jones J., Recent Arctic amplification and extreme mid-latitude weather. Nature Geoscience. Vol 7- 627 https://doi.org/10.1038/ngeo2234 (2014)

13. Coumou, D. and Rahmstorf, S. A decade of weather extremes. Nature Clim. Change 2, 491–496 (2012)

14. Coumou, D. Di Capua, G. Vavrus, S. Wang, L. Wang, S., The influence of Arctic amplification on mid-latitude summer circulation. Nature Communications. Vol 9 - 1 2041–1723 https://doi.org/10.1038/s41467-018-05256-8 (2018)

15. Davies T.D., Schuepbach E. Episodes oh high ozone concentrations at the Earth's surface resulting from transport down from the upper troposphere/lower stratosphere: a review and case studies. Atmos.Environ., 28 (1994), pp. 53–68 (1994)

16. Delaygue G., Bekki S., and Bard E., Modelling the stratospheric budget of beryllium isotopes. Tellus B, 67, 28582, http://dx.doi.org/10.3402/tellusb.v67.28582 (2015)

17. Dhomse, S. S., Chipperfield, M. P., Damadeo, R. P., Zawodny, J. M., Ball, W. T., Feng, W., Haigh, J. D. On the ambiguous nature of the 11-year solar cycle signal in upper stratospheric ozone. Geophysical Research Letters. (2016)

18. Doering C., Saey P., Hadley cell influence on Be-7 activity concentrations at Australian mainland IMS radionuclide particulate stations. J. Environ. Radioact., 127, pp. 88–94 (2014)

19. Dutkiewicz, Vincent A., and Liaquat Husain. Determination of stratospheric ozone at ground level using Be-7/ozone ratios. Geophysical Research Letters 6.3, 171-174 (1979)

20. Fasullo, J. and Webster, P.J. A hydrological definition of Indian Monsoon onset and withdrawal. J. Clim. 16, 3200–3211 (2003).

21. Feely, H.W., Larsen, R.J., Sanderson, C.G., Factors that cause seasonal variation in Be-7 concentrations in surface air. Journal of Environmental Radioactivity 9,223-249 (1989)

22. Forbush, S.E. World-wide cosmic-ray variations, 1937-1952 J. Geophys. Res. Volume 59, Issue 4 (1954)

23. Francis J. and Skific N., Evidence linking rapid Arctic warming to mid-latitude weather patterns. Philosophical Transactions of The Royal Society A Mathematical Physical and Engineering Sciences 373(2045) DOI: 10.1098/rsta.2014.0170 (2015)

24. Hakuba M, Stephens G., Vergados P., Ao C., Mannucci A. On the Breathing of the Tropical Troposphere and its relation to the Tropical energy balance. Geophysical Research Abstracts Vol. 21, EGU2019-12148 (2019)

25. Hays, J. D., Imbrie, J. & Shackleton, N. J. Science 194, 1121–1132 (1976)

26. Hernandez-Ceballos M. A., Cinelli G., Marín Ferrer M., Tollefsen T., De Felice L., Nweke E., Tognoli P. V., Vanzo S., De Cort M. A., climatology of Be-7 in surface air in European

Union. Journal of Environmental Radioactivity 141, 62–70
http://dx.doi.org/10.1016/j.jenvrad.2014.12.003 (2015)

27. Hernandez-Ceballos M.A., Cinelli G. , Tollefsen T., Marin-Ferrer M. , 2016.
    Identification of airborne radioactivity special patterns in Europe – Feasibility study using
    Be-7. Journal of Environmental Radioactivity 155-156 55-62.
    http://dx.doi.org/10.1016/j.jenvrad.2016.02.006 (2016)

28. https://climate.nasa.gov/climate_resources/189/graphic-temperature-vs-solar-activity/
    (2019)

29. https://cpo.noaa.gov/sites/cpo/Projects/COD/2014/Seidel_CM_FY14_Abstract.pdf (2019)

30. https://science2017.globalchange.gov/chapter/2/#fig-2-3 (2019)

31. Ioannidou A., Vasileiadis D. M., Time lag between the tropopause height and Be-7 activity
    concentrations on surface air. Journal of Environmental Radioactivity, 129, pp. 80–85
    (2014)

32. Ioannidou, A., Manolopoulou, M. and Papastefanou, C.. Temporal changes of Be-7 and
    210Pb concentrations in surface air at temperate latitudes (40 degrees N). Appl. Radiat.
    Isot. 63, 277–284 (2005)

33. IPCC ARA5 chapter 2
    https://www.ipcc.ch/site/assets/uploads/2017/09/WG1AR5_Chapter02_FINAL.pdf (2019)

34. Jasiulionisa R. and Wershofen H., A study of the vertical diffusion of the cosmogenic
    radionuclides, Be-7 and Na-22 in the atmosphere. Journal of Environmental Radioactivity,
    79, 157–169 (2005)

35. Koch, D. and Rind, D. Beryllium 10/beryllium 7 as a tracer of stratospheric transport. J.
    Geophys. Res. 103(D4), 3907[1]3917. DOI: 10.1029/97JD03117. (1998)

36. Kornhuber K., Osprey S., Coumou D., Petri S., Petoukhov V., Rahmstorf S., and Gray L., Extreme weather events in early summer 2018 connected by a recurrent hemispheric wave-7 pattern. Environmental Research Letters, 14(5), 1–7. [054002]. https://doi.org/10.1088/1748-9326/ab13bf (2019)

37. Kusmierczyk-Michulec J., Gheddou A., Nikkinen M., Influence of precipitation on Be-7 concentrations in air as measured by CTBTO global monitoring system. Journal of Environmental Radioactivity, 144, pp. 140-151 (2015)

38. Kusmierczyk-Michulec J., Tedeschi G., Van Eijk AMJ, and Piazzola J. Influence of atmospheric parameters on vertical profiles and horizontal transport of aerosols generated in the surf zone. Atmos. Environ. 77, 664–673 (2013).

39. Lal D. and Peters B., Cosmic Ray Produced Radioactivity on the Earth. Kosmische Strahlung II/Cosmic Rays II. Handbuch der Physik/Encyclopedia of Physics 9, 551–612 (1962)

40. Larin AE, Malyshevskii VS, Fomin GV. Altitude and Latitude Distribution of the Production Rate of 7Be in the Earth's Atmosphere in the PARMA Model. Russian Physics Journal, 57(6):1-6 (2014)

41. Lau K-M, Yang S.. Walker Circulation, doi:10.1006/rwas.2002.0450 (2002)

42. Lee, H. N., Tositti, L., Zheng, X., & Bonasoni, P.. Analyses and comparisons of variations of Be-7, 210Pb, and Be-7/210Pb with ozone observations at two Global Atmosphere Watch stations from high mountains. Journal of Geophysical Research: Atmospheres, 112(D5) (2007)

43. Lederer G.G. Modeling of Deep-Convective Transport of Forest Fire Smoke into the Upper Troposphere and Lower Stratosphere. PhD dissertation. https://www.pik-potsdam.de/members/luderer/publications/diss_luderer.pdf (2007)

44. Lenton T.M, Held H, Kriegler E, Hall J, Lucht W, Rahmstorf S, Schellnhuber H.J,. Tipping elements in the Earth's climate system. Proc. Natl Acad. Sci. USA. 105, 1786–1793. doi:10.1073/pnas.0705414105 (2008)

45. Leppänen P. and Usoskin L.G. Cosmogenic Be-7 and Na-22 in Finland: Production, observed periodicities and the connection to climatic phenomena. J. Atmos. Sol.-Terr. Phy. 74, 164–180 (2012)

46. Lorenz D. J. and DeWeaver E. T., Tropopause height and zonal wind response to global warming in the IPCC scenario integrations, J. of Geophys. Res., 112, D10119, https://doi.org/10.1029/2006JD008087 (2007)

47. Ma J., Chadwick R., Seo K. H., Dong C., Huang G., Foltz G. R., Jiang J. H. Responses of the Tropical Atmospheric Circulation to Climate Change and Connection to the Hydrological Cycle. Annual Review of Earth and Planetary Sciences, Vol. 46:549–580. https://doi.org/10.1146/annurev-earth-082517010102 (2018)

48. Mann M. E., Rahmstorf S., Kornhuber K., Steinman B. A., K. Miller S. K., and Coumou D., Influence of Anthropogenic Climate Change on Planetary Wave Resonance and Extreme Weather Events. Scientific Reports, Vol 7, pp 45242. https://doi.org/10.1038/srep45242 (2017)

49. Mann M. E., Rahmstorf S., Kornhuber K., Steinman B. A., K. Miller S. K., Petri S., and Coumou D., Projected changes in persistent extreme summer weather events: The role of quasi-resonant amplification. Science Advances, Vol. 4, no. 10. DOI: 10.1126/sciadv.aat3272 (2018)

50. Martin P. and McBride J. L. Radionuclide Behavior and Transport in the Tropical Atmospheric Environment. Radioactivity in the Environment 18, 59–91 (2012).

51. Masarik J., and Beer J., An updated simulation of particle fluxes and cosmogenic nuclide production in the Earth's atmosphere, J. Geophys. Res., 114, D11103, doi:10.1029/2008JD010557 (2009)

52. Masarik J., Beer J., Simulation of particle fluxes and cosmogenic nuclide production in the Earth' S atmosphere. J. Geophys. Res.: Atmospheres. 104, 99–111. (1999)

53. Maslin M., Forty years of linking orbits to ice ages. Nature, Vol 540, pp 208, https://doi.org/10.1038/540208a (2016)

54. Monsoon. India Meteorological Department, at http://www.imd.gov.in/(2018)

55. MunichRe https://www.munichre.com (2019)

56. Neroda, A. S., Goncharova, A. A., Goryachev, V. A., Mishukov, V. F., & Shlyk, N. V.. Long-range atmospheric transport Be-7 to region the Sea of Japan. Journal of environmental radioactivity, 160, 102-111 (2016)

57. Newman P.A., Coy L., Pawson S. and Lait L. R.. The anomalous change in the QBO in 2015-2016. American Geophysical Union. DOI 10.1002/2016GL070373 (2016)

58. Pacini A., 2015. Signature of Sudden Stratospheric Warming in the near ground Be-7 flux. https://doi.org/10.1016/j.atmosenv.2015.04.065.

59. Paliwal A. Why India Struggles to Predict the Weather Over Its Lands. The Wire (2018). at <https://thewire.in/180850/imd-weather-prediction-forecast-monsoons-drought-agrometeorology-kharif>

60. Petoukhov V., Rahmstorf S., Petri S., Schelln H. J., Huber H., Schellnhuber J., Quasiresonant amplification of planetary waves and recent Northern Hemisphere weather extremes. Proceedings of the National Academy of Sciences 110(14) DOI: 10.1073/pnas.1222000110 (2013)

61. Poletti W., Biggin A. J., Trindad R. I. F., Hartmann G. A., Terra-Nova F., Continuous millennial decrease of the Earth's magnetic axial dipole. Physics of the Earth and Planetary Interiors journal, Vol 274, pp 72–86. https://doi.org/10.1016/j.pepi.2017.11.005 (2018)

62. Pradhan M., Rao A. S., Srivastava A., Dakate A., Salunke K. & Shameera K. S. Prediction of Indian Summer-Monsoon Onset Variability: A Season in Advance. Sci. Rep. 7, 14229 (2017)

63. Prein A. F., Liu C.I., Kyoko T., Rasmussen S. B., Holland R. M., Clark G. J., Martyn P., Increased rainfall volume from future convective storms in the US. Nature Climate Change, Vol 7, Issue 12, pp 1758–6798 https://doi.org/10.1038/s41558-017-0007-7 (2017)

64. Pulakkat H. The odds of foretelling rains: Why monsoon prediction is hard, and why it could soon improve. The Economic Times at https://economictimes.indiatimes.com/news/politics-and-nation/the-odds-of-foretelling-rains-why-monsoon-prediction-is-hard-and-why-it-could-soon-improve/articleshow/52876823.cms (2016)

65. Radionuclide Monitoring. Comprehensive Nuclear-Test-Ban Treaty Organization at https://www.ctbto.org/verification-regime/monitoring-technologies-how-they-work/radionuclide-monitoring (2018)

66. Rajačić M. M., Todorović D. J., Janković M. M., Nikolić J. D., Sarap N. B., Pantelić G. K., Be-7 in atmospheric deposition: determination of seasonal indices. J. Radioanal. Nucl. Chem. 303 (3), 2535–2538. http://dx.doi.org/10.1007/s10967-014-3733-6 (2015)

67. Rajačić M. M., Todorović D. J., Krneta Nikolica J. D., Puzovicb J. M., The impact of the Solar magnetic field on Be-7 activity concentration in aerosols. Applied Radiation and Isotopes 125 27–29. http://dx.doi.org/10.1016/j.apradiso.2017.04.008 (2017)

68. Randel W. J., Jensen E. J., Physical processes in the tropical tropopause layer and their roles in a changing climate. Nature Geoscience Vol 6, pp 169 https://doi.org/10.1038/ngeo1733 (2013)

69. Santer B. D., Identification of anthropogenic climate change using a second-generation reanalysis, J. Geophys. Res., 109, D21104, doi:10.1029/2004JD005075. (2004)

70. Schmidt T., Cammas J. P., Smit H., Heise S., Wickert J., and Haser A., Observational characteristics of the tropopause inversion layer derived from CHAMP/GRACE radio occultations and MOZAIC aircraft data. J. Geophys. Res., 115, D24304, doi:10.1029/2010JD014284 (2010)

71. Schmidt T., Wickert J., Beyerle G., and Heise S., Global tropopause height trends estimated from GPS radio occultation data. Geophys. Res. Lett., Vol. 35, 11806. doi:10.1029/2008GL034012 (2008)

72. Schmidt, T., Wickert J., and Haser A., Variability of the upper troposphere and lower stratosphere observed with GPS radio occultation bending angles and temperatures. Adv. Space. Res., 46, 150–161, doi:10.1016/j.asr.2010.01.021 (2010)

73. Seidel D. J., and Randel W. J., Variability and trends in the global tropopause estimated from radisonde data, J. Geophys. Res. 111, D21101, doi:10.1029/2006JD007363 (2006)

74. Seidel D. J., Fu Q., Randel W. J., and Reichler T. J., Widening of the tropical belt in a changing climate. Nature Geoscience, Vol 1(1), pp 21-24, DOI: 10.1038/ngeo.2007.38 (2007)

75. Seidel D., Butler A.. A comprehensive Atlas of Mid-Winter Sudden Stratospheric Warmings and Associated Surface Climate Extremes. (2016)

76. Sikka, D.R. and Gadgil, S. On the Maximum Cloud Zone and the ITCZ over Indian, Longitudes during the Southwest Monsoon. Mon. Wea. Rev. 108, 1840–1853 (1980).

77. Škerlak B., Sprenger M. and Wernli H., A global climatology of stratosphere–troposphere exchange using the ERA-Interim data set from 1979 to 2011. Atmospheric Chemistry and Physics, 14, pp. 913–937 (2014)

78. Soman, M.K. and Kumar, K.K. Space-Time Evolution of Meteorological Features Associated with the Onset of Indian Summer Monsoon. Mon. Wea. Rev. 121, 1177–1194 (1993)

79. Steinmann P., Zeller M., Beuret P., Ferreri G. and Estier S., Cosmogenic Be-7 and Na-22 in ground level air in Switzerland (1994–2011). Journal of Environmental Radioactivity, 124, pp. 68-73 (2013)

80. Stohl A, Bonasoni P, Cristofanelli P, Collins W, Feichter J, Frank A, Forster C, Gerasopoulos E, Gäggeler H, and James P. Stratosphere-troposphere exchange: a review, and what we have learned from staccato. J. Geophys. Res. Atmos. 108, 8516 (2003)

81. Stohl A., Bonasoni P., Cristofanelli P., Collins W., Feichter J., Stratosphere-troposphere exchange: a review, and what we have learned from STACCATO. J. Geophys. Res. 108(D12), 8516. DOI: 10.1029/2002JD002490 (2003)

82. Stolbova V., Surovyatkina E., Bookhagen B., and Kurths J. Tipping elements of the Indian monsoon: prediction of onset and withdrawal. Geophys. Res. Lett. 43, 1-9 (2016)

83. Stuecker, M.F., Bitz, C.M., Armour, K.C. et al. Polar amplification dominated by local forcing and feedbacks. Nature Clim Change 8, 1076–1081 doi:10.1038/s41558-018-0339-y (2018)

84. Su C., Huh C., Lin F..Factors controlling fluxes of Be-7 and 210Pb in northern Taiwan, Geophysical Research Letters, Vol 30, No 19, 2018, doi: 10.1029/2003GL018221. (2003)

85. Syroka, J. and Toumi, R. On the withdrawal of the Indian summer monsoon. Q. J. R. Meteorol. Soc. 130, 989–1008 (2004)

86. Tang Q., Zhang, X., Francis J. A., Extreme summer weather in northern mid-latitudes linked to a vanishing cryosphere. Nature Climate Change Vol 4, pp 45 https://doi.org/10.1038/nclimate2065 (2013)

87. Taniguchi, K. and Koike, T. Comparison of definitions of Indian summer monsoon onset: Better representation of rapid transitions of atmospheric conditions. Geophys. Res. Lett. 33, 1–5 (2006)

88. Taylor, A., Keith-Roach, M. J., Iurian, A. R., Mabit, L., & Blake, W. H. Temporal variability of Be-7 fallout in southwest UK. Journal of environmental radioactivity, 160, 80-86. (2016)

89. Terzi L., and Kalinowski M., World-wide seasonal variation of Be-7 related to large-scale atmospheric circulation dynamics. J. Environ. Radioact. 178–179, 1–15 (2017)

90. Terzi L., Kalinowski M., Schoeppner M. and Wotawa G. How to predict seasonal weather and monsoons with radionuclide monitoring. Scientific Reports 9, Article number: 2729 https://doi.org/10.1038/s41598-019-39664-7 (2019)

91. Terzi L., Kalinowski M., Schoeppner M. and Wotawa G., Using Be-7 to predict monsoons. Research square, video abstract DOI: 10.21203/rs.2.15005/v1 (2019)

92. Terzi L., Kalinowski. M., Schoeppner M., and Kusmierczyk-Michulec J. Atmospheric Be-7 concentration changes as a possible new indicator for early warning on Indian Monsoon onset. (2017)

93. Terzi L., Wotawa G., Kalinowski M., Schoeppner M., Saey P., Steinmann P., Luan L. and Staten P.W..Radioisotopes demonstrate changes in global atmospheric circulation possibly caused by global warming. Under review process at *Scientific Reports (2020)*.

94. Tilley D.R., Cheves C.M., Godwin J.L., Hale G.M., Hofmann H.M., Kelley J.H., Sheu C.G., and Weller H.R. Energy levels of light nuclei A = 5, 6, 7. Nuclear Physics A 708, 3–163 (2002)

95. Tilley D.R., Cheves C.M., Godwin J.L., Hale G.M., Hofmann H.M., Kelley J.H., Sheu C.G., Weller H.R., Energy levels of light nuclei A=5, 6, 7, Nuclear Physics A, Volume 708, Issue 1, Pages 3-163, ISSN 0375-9474, http://dx.doi.org/10.1016/S0375-9474(02)00597-3 (2002,)

96. Tilley, D. R. et al. Energy levels of light nuclei A = 5, 6, 7. Nuclear Physics A 708, 3–163 (2002)

97. Usoskin I. G., Bazilevskaya G. A. and Kovaltsov G. A., Solar modulation parameter for cosmic rays since 1936 reconstructed from ground-based neutron monitors and ionization chambers. J. Geophys. Res. 116(A2), A02104. DOI: 10.1029/ 2010JA016105 (2011)

98. Usoskin I. G., Field C. V., Schmidt G. A., Leppanen A. P., Aldahan A., Short-term production and synoptic influences on atmospheric Be-7 concentrations. J. Geophys. Res. 114, D06108. DOI: 10.1029/2008JD011333 (2009)

99. Usoskin, I. G. and Kovaltsov, G. A., Production of cosmogenic Be-7 isotope in the atmosphere: full 3-D modeling. J. Geophys. Res. 113, D12107. DOI: 10.1029/2007JD009725 (2008)

100. Vecchi G. A., Soden B. J., Wittenberg A. T., Held I. M., Leetmaa A., Harrison M. J., Weakening of tropical Pacific atmospheric circulation due to anthropogenic forcing. Nature, Vol 441, Issue 7089, pp 1476–4687 https://doi.org/10.1038/nature04744 (2006)

101. Walker J. and Bodoni S. Onset and withdrawal of the large-scale South Asian monsoon: A dynamical definition using change point detection. Geophys. Res. Lett. 43, 11,815–11,822 (2016)

102. Wang, B., Ding, Q. and Joseph, P.V. Objective definition of the Indian summer monsoon onset. J. Clim. 22, 3303–3316 (2009)

103. Wang, B., Wu, R. and Lau, K.M. Interannual Variability of the Asian Summer Monsoon: Contrasts between the Indian and the Western North Pacific – East Asian Monsoons. J. Clim. 14, 4073–4090 (2001)

104. Wang, J. S., Seidel D. J., and Free M., How well do we know recent climate trends at the tropical tropopause? J. Geophys. Res., 117, D09118, doi:10.1029/2012JD017444 (2012)

105. Wang, B. and Fan Z. Choice of South Asian summer monsoon indices. Bull. Amer. Meteor. Soc. 80, 629–638 (1999)

106. Webster, P.J. Mechanisms of monsoon low-frequency variability: Surface hydrological effects. J. Atmospheric Sci. 40, 2110–2124 (1983)

107. Webster, P. Improve weather forecasts for the developing world. Nature 493, 17–19 (2013)

108. Xian T. and Homeyer C. R. Global tropopause altitudes in radiosondes and reanalyses. Atmos. Chem. Phys., Vol 19, pp 5661–5678 https://doi.org/10.5194/acp-19-5661-2019 (2019)

109. Yasunari T., Zonally propagating modes of the global east-west circulation associated with the Southern Oscillation. J. Met. Soc. Japan, 63, 1013 1029. http://doi.org/10.2151/jmsj1965.63.6_1013 (1985)

110. Yin J., Gentine P., Zhou S., Sullivan S. C., Wang R., Zhang Y., Guo S., Large increase in global storm runoff extremes driven by climate and anthropogenic changes. Nature Communications, Vol 9, Issue 1, pp 2041–1723 https://doi.org/10.1038/s41467-018-06765-2 (2018)

111. Yoshimori M., Hirayama H., Mori S., Sasaki K., Sakurai H., Be-7 nuclei produced by galactic cosmic rays and solar energetic particles in the earth's atmosphere. Advances in Space Research, Vol 32, Issue 12, pp. 2691–2696 (2003)

112. Zhang M. and Song H. Evidence of deceleration of atmospheric vertical overturning circulation over the tropical Pacific. Geophysical Research Letters, Vol 33, Issue 12. https://doi.org/10.1029/2006GL025942 (2006)

Acknowledgments

Annex A Supplementary Tables

Table 6 IMS RN Stations grouped by Northern and Southern Hemisphere, Western and Eastern Quarter.

Northern Hemisphere	Southern Hemisphere	Lat 0,90 Lon 0, -180	Lat 0,90 Lon 0, +180	Lat 0, -90 Lon 0, +180	Lat 0, -90 Lon y0, -180
RN14	RN01	RN14	RN13*	RN04	RN01
RN15	RN03	RN15	RN33	RN05	RN03
RN16	RN04	RN16	RN37	RN06	RN11
RN17	RN05	RN17	RN38	RN07	RN23
RN13*	RN06	RN28	RN40	RN08*	RN18
RN33	RN07	RN31*	RN45	RN09*	RN19
RN28	RN08*	RN34	RN42*	RN10	RN27
RN31*	RN09*	RN39*	RN49	RN26	RN67
RN34	RN10	RN43	RN52	RN29	RN68
RN37	RN11	RN44	RN54	RN30	RN46
RN38	RN23	RN50*	RN56	RN66*	RN73
RN39*	RN18	RN53	RN58	RN47	Total 11
RN40	RN19	RN70	RN59	RN51*	
RN45	RN26	RN71	RN60	RN64*	
RN43	RN27	RN72	RN61	Total 14	
RN44	RN29	RN74	RN63		
RN42*	RN30	RN75	RN77		
RN49	RN66*	RN76	RN80		
RN50*	RN67	RN78	Total 18		
RN52	RN68	RN79			
RN53	RN46	Total 20			
RN54	RN47				
RN56	RN51*				
RN58	RN64*				
RN59	RN73				
RN60	Total 25				
RN61					
RN63					
RN70					
RN71					
RN72					
RN74					
RN75					
RN76					
RN77					
RN78					
RN79					
RN80					
Total 38					

Table 7 List of IMS radionuclide stations belonging to each band.

Band 1	Band 2	Band 3	Band 4	Band 5	Band 6	Band 7	Band 8	Band 9	Band 10	Band 11	Band 12	Equatorial Band
RN07	RN14	RN01	RN01	RN13*	RN13*	RN05	RN05	RN08*	RN09*	RN04	RN07	RN08
RN23	RN16	RN03	RN03	RN67	RN33	RN29	RN08*	RN10	RN10	RN06	RN26	RN09
RN27	RN18	RN15	RN11	RN68	RN67	RN30	RN29	RN45	RN37	RN38	RN38	RN13
RN39*	RN19	RN18	RN15	RN34	RN68	RN40	RN30	RN42*	RN52	RN51*	RN47	RN31
RN46	RN44	RN28	RN17	RN43	RN43	RN49	RN66*	RN52	RN56	RN60	RN51*	RN66
RN71	RN50*	RN50*	RN18	RN53	RN49	RN54	RN45	RN56	RN58	RN80	RN60	RN39
RN76	RN70	RN72	RN28		RN63	RN61	RN59				RN77	RN42
RN78	RN73	RN73	RN31*			RN64*						RN50
RN79		RN74	RN73									RN51
		RN75										RN64

Table 8 ^{7}Be concentrations used to produce each longitudinal band plot (see figure 4).

BAND_1	USP76 (65,-147)	USP71 (55,-160)	USP78 (28,-177)	USP79 (22,-158)	KIP39 (2,-157)	FRP27 (-18,-150)	CKP23 (-21,-160)	NZP46 (-44,-176)	AUP07 (-55,159)
Jan	2357.73	2604.41	5431.19	3544.98	1514.46	3020.86	3019.29	4004.14	1374.95
Feb	3182.65	2652.11	5030.50	3689.02	1753.56	2989.87	3133.42	3990.75	1467.98
Mar	4056.91	3449.52	4995.29	3483.57	1533.91	3135.45	2994.51	3735.34	1616.87
Apr	4437.61	2934.19	5130.01	3525.92	1223.55	2857.09	3411.51	3086.04	1461.07
May	5307.92	1815.00	4629.16	3539.88	1483.37	3291.91	3701.41	2613.18	1417.53
Jun	3827.01	1220.09	3704.91	2799.79	1787.51	3473.12	3623.47	2235.33	1448.47
Jul	3082.07	888.55	3051.53	2647.57	2449.64	3443.36	3938.65	2143.54	1453.62
Aug	2595.43	1449.53	3341.17	2910.82	3215.40	3700.38	4318.95	2139.04	1289.27
Sep	2423.57	1885.64	3644.99	2773.95	2969.98	3228.89	4042.94	2710.81	1699.24
Oct	1731.79	2043.37	4456.92	2867.31	3223.09	3677.31	4650.48	2885.71	1659.81
Nov	1873.67	2436.15	4395.73	2762.70	2376.90	3571.58	3974.12	3185.48	1662.76
Dec	2197.37	2517.87	4557.28	2953.82	2073.67	2820.35	3640.03	3479.65	1324.74
BAND_2	CAP16 (62,-114)	CAP14 (49,-123)	USP70 (39,-121)	MXP44 (28,-114)	PAP50 (9,-80)	CLP19 (-27,-109)	CLP18 (-53,-71)	USP73 (-65,-64)	
Jan	2085.80	2114.39	4628.29	6282.37	3218.08	4598.18	2230.20	1720.50	
Feb	2401.26	2360.85	5007.20	5464.28	3608.43	5336.77	2498.09	1702.45	
Mar	3062.19	2585.78	5377.73	6102.49	4248.16	4654.36	2105.95	1492.12	
Apr	3686.39	2558.21	5256.44	5140.71	3487.77	4296.61	1842.02	1580.25	
May	4101.25	2937.07	5689.19	5298.07	2471.71	3772.33	1587.91	1269.11	
Jun	4205.93	1901.18	4438.14	4230.25	1372.74	3432.69	1320.18	1468.84	
Jul	3897.20	1698.29	4214.75	3429.23	1602.91	3442.94	1532.21	1738.56	
Aug	3008.97	2298.73	4481.83	4154.08	1440.29	3483.52	1662.98	1549.95	
Sep	2162.60	3014.60	5898.39	5069.13	1148.89	3805.15	1666.79	1405.43	

Oct	1542.08	2513.82	5532.60	5882.94	1185.30	4514.15	1827.33	1590.88
Nov	1681.68	2406.61	4728.29	5960.26	1862.71	4154.82	1709.37	1551.69
Dec	1905.14	2351.45	4205.56	5804.25	2717.95	5509.40	1694.21	1762.50

BAND_3	CAP15 (75, -95)	USP75 (78, 38)	USP74 (37,-100)	USP72 (28,-81)	FRP28 (16,-62)	PAP50 (9,-80)	ARP01 (-35,-58)	ARP03 (-41,-71)	CLP18 (-53,-71)
Jan	2633.64	4372.26	4923.26	6545.96	2515.16	3218.08	6499.59	6235.89	2230.20
Feb	2312.41	5006.42	5004.24	6686.32	2439.33	3608.43	5786.91	6184.62	2498.09
Mar	2865.28	5672.30	5798.25	7567.17	3401.44	4248.16	5508.38	5156.93	2105.95
Apr	3040.26	6358.87	6627.51	7736.43	3263.27	3487.77	5039.02	3961.07	1842.02
May	2173.75	5993.93	6333.14	7178.47	3312.16	2471.71	3925.12	3226.30	1587.91
Jun	1212.04	5840.84	6469.83	4986.99	3409.75	1372.74	3555.90	2231.35	1320.18
Jul	1771.17	5631.61	5756.50	4540.62	3193.79	1602.91	3334.73	2193.55	1532.21
Aug	1046.58	5385.30	5925.84	4297.34	2773.79	1440.29	3534.15	2691.80	1662.98
Sep	1137.76	4903.20	5684.79	4947.11	2128.73	1148.89	4127.09	3291.05	1666.79
Oct	1357.99	4495.74	5318.30	6140.74	2396.24	1185.30	4778.87	3907.37	1827.33
Nov	1860.42	4502.09	5020.11	6346.14	2604.83	1862.71	5615.66	4511.51	1709.37
Dec	2045.76	4275.53	4431.33	6266.94	2644.41	2717.95	6142.53	5001.55	1694.21

BAND_4	CAP15 (75,-95)	CAP17 (48,-53)	FRP28 (16,-62)	FRP31 (5,-53)	BRP11 (-23,-43)	ARP01 (-35,-58)	ARP03 (-41,-71)	CLP18 (-53,-71)	USP73 (-65,-64)
Jan	2633.64	2353.31	2515.16	2946.49	2986.74	6499.59	6235.89	2230.20	1720.50
Feb	2312.41	2617.10	2439.33	2922.83	3089.71	5786.91	6184.62	2498.09	1702.45
Mar	2865.28	3119.37	3401.44	3701.82	3124.07	5508.38	5156.93	2105.95	1492.12
Apr	3040.26	3275.78	3263.27	3330.92	3266.79	5039.02	3961.07	1842.02	1580.25
May	2173.75	2540.12	3312.16	2506.54	3664.05	3925.12	3226.30	1587.91	1269.11
Jun	1212.04	2253.83	3409.75	1713.40	3202.68	3555.90	2231.35	1320.18	1468.84
Jul	1771.17	2889.07	3193.79	1793.51	3255.42	3334.73	2193.55	1532.21	1738.56
Aug	1046.58	2645.58	2773.79	2179.95	3429.02	3534.15	2691.80	1662.98	1549.95
Sep	1137.76	2928.15	2128.73	2809.79	3474.43	4127.09	3291.05	1666.79	1405.43
Oct	1357.99	1974.31	2396.24	2446.63	3197.25	4778.87	3907.37	1827.33	1590.88
Nov	1860.42	2258.37	2604.83	1919.06	3215.45	5615.66	4511.51	1709.37	1551.69
Dec	2045.76	2453.13	2644.41	1919.69	2898.60	6142.53	5001.55	1694.21	1762.50

BAND_5	ISP34 (64,-22)	PTP53 (38,-26)	MRP43 (18,-16)	CMP13 (4,10)	GBP67 (-16,-6)	GBP68 (-37,-12)
Jan	1955.48	3528.52	5275.30	3995.16	5884.30	3895.33
Feb	2164.71	3930.38	5655.51	3646.63	5214.27	4200.23
Mar	2295.59	3935.81	5377.57	3021.81	4738.23	4313.73
Apr	2464.01	4375.39	5285.59	2145.73	4481.31	3490.78
May	2405.05	4282.34	5217.61	2096.94	4500.98	2941.68
Jun	1881.47	4332.39	5182.02	3204.95	4369.42	2740.05
Jul	1613.57	4317.24	4980.75	3431.30	3945.86	2765.04
Aug	1584.65	3819.10	4656.42	2290.87	3800.80	2595.33

Sep	1439.52	3598.04	4242.89	912.63	5014.97	2869.52
Oct	1646.29	3326.08	5072.01	921.23	5450.15	2797.81
Nov	1547.95	3728.05	5725.57	2284.18	5724.29	3212.31
Dec	1961.45	3511.41	5640.70	3818.35	5731.34	3542.49

BAND_6	NOP49 (78,15)	SEP63 (59,18)	DEP33 (48,8)	MRP43 (18,-16)	CMP13 (4,10)	GBP67 (-16,-6)	GBP68 (-37,-12)
Jan	2172.66	2276.00	3194.16	5275.30	3995.16	5884.30	3895.33
Feb	2272.92	2372.06	3247.49	5655.51	3646.63	5214.27	4200.23
Mar	2526.83	2654.25	3952.90	5377.57	3021.81	4738.23	4313.73
Apr	2657.36	3165.75	4665.08	5285.59	2145.73	4481.31	3490.78
May	2003.86	3552.15	5035.82	5217.61	2096.94	4500.98	2941.68
Jun	1325.83	3535.04	5039.49	5182.02	3204.95	4369.42	2740.05
Jul	1139.94	3432.31	5164.00	4980.75	3431.30	3945.86	2765.04
Aug	1191.99	3530.58	4724.73	4656.42	2290.87	3800.80	2595.33
Sep	1399.96	2635.60	4613.18	4242.89	912.63	5014.97	2869.52
Oct	1126.26	2270.87	4379.95	5072.01	921.23	5450.15	2797.81
Nov	1503.28	1920.30	3312.33	5725.57	2284.18	5724.29	3212.31
Dec	1957.89	2123.58	2872.84	5640.70	3818.35	5731.34	3542.49

BAND_7	NOP49 (78,15)	RUP54 (49, 59)	RUP61 (57,37)	KWP40 (29,48)	TZP64 (-7,39)	FRP29 (-21,56)	FRP30 (-49,70)	AUP05 (-68,63)
Jan	2172.66	2400.35	2084.88	4977.96	5829.26	2960.13	1766.29	6910.83
Feb	2272.92	2409.08	2881.24	5562.25	5647.72	2897.81	1809.21	6902.20
Mar	2526.83	2550.60	3018.24	7142.84	3850.91	2738.02	1826.75	5975.87
Apr	2657.36	3536.22	4179.89	7240.30	3443.16	2963.40	1614.90	4538.17
May	2003.86	5179.34	5490.10	7981.94	4286.13	3016.94	1404.17	3894.09
Jun	1325.83	4865.40	5199.63	9580.85	4572.52	3147.98	1284.37	4399.94
Jul	1139.94	4309.24	5592.49	10667.89	4501.36	3161.99	1346.91	4042.82
Aug	1191.99	4462.26	4734.93	9546.35	4376.59	3275.31	1578.16	4268.57
Sep	1399.96	2810.46	3029.30	8216.10	4610.74	3484.09	1508.65	4215.08
Oct	1126.26	2118.66	2596.88	6651.92	4341.54	3457.96	1623.67	4992.57
Nov	1503.28	2116.56	2310.72	5347.17	4222.72	3560.93	1656.23	5286.74
Dec	1957.89	1806.81	2246.99	5062.68	4776.14	3541.94	1762.82	5619.61

BAND_8	RUP59 (54,85)	MNP45 (48,106)	GBP66 (-7,72)	AUP08 (97 -12)	FRP29 (-21,56)	FRP30 (-49,70)	AUP05 (-68,63)
Jan	3014.77	4637.34	2971.75	4149.89	2960.13	1766.29	6910.83
Feb	2843.73	5141.34	3549.76	3155.70	2897.81	1809.21	6902.20
Mar	3932.58	5475.07	2959.27	2882.85	2738.02	1826.75	5975.87
Apr	5714.48	6331.39	2690.87	3025.12	2963.40	1614.90	4538.17
May	5945.43	6396.36	2996.12	3076.86	3016.94	1404.17	3894.09
Jun	6363.60	6299.55	2615.82	3066.71	3147.98	1284.37	4399.94
Jul	5685.39	6437.19	2609.03	3178.63	3161.99	1346.91	4042.82

Aug	4801.68	5905.78	2623.81	3710.61	3275.31	1578.16	4268.57
Sep	4323.45	5694.25	2734.13	3901.75	3484.09	1508.65	4215.08
Oct	3863.37	5137.79	2873.41	4097.23	3457.96	1623.67	4992.57
Nov	3046.06	4793.65	2645.14	4163.72	3560.93	1656.23	5286.74
Dec	3196.26	4717.52	2493.23	3730.10	3541.94	1762.82	5619.61
BAND_9	RUP56 (60,113)	MNP45 (48,106)	PHP52 (15,121)	MYP42 (4,101)	AUP08 (-12,97)	AUP10 (-32,116)	
Jan	3959.53	4637.34	2473.40	2082.17	4149.89	5473.78	
Feb	4676.61	5141.34	3024.17	2513.01	3155.70	5542.74	
Mar	5080.34	5475.07	3702.74	2530.97	2882.85	5174.26	
Apr	6277.82	6331.39	3434.20	2015.90	3025.12	4426.34	
May	6313.14	6396.36	1941.00	1612.33	3076.86	3956.33	
Jun	6412.94	6299.55	1403.96	2419.01	3066.71	3344.53	
Jul	5834.16	6437.19	1129.12	2404.07	3178.63	3315.51	
Aug	3260.00	5905.78	1285.08	1859.23	3710.61	3486.37	
Sep	2275.64	5694.25	1044.26	1900.67	3901.75	3730.03	
Oct	2231.76	5137.79	2301.31	1833.09	4097.23	4061.95	
Nov	1964.19	4793.65	1697.81	1130.16	4163.72	4644.56	
Dec		4717.52	1651.04	1097.36	3730.10	5111.61	
BAND_10	RUP56 (60,113)	RUP58 (44,132)	JPP37 (27,128)	PHP52 (15,121)	AUP09 (-12,131)	AUP10 (-32,116)	
Jan	3959.53	4334.77	6454.76	2473.40	3730.51	5473.78	
Feb	4676.61	4655.57	5885.61	3024.17	3825.44	5542.74	
Mar	5080.34	5626.19	6314.93	3702.74	3647.40	5174.26	
Apr	6277.82	5842.95	5454.11	3434.20	5035.43	4426.34	
May	6313.14	4213.58	3811.98	1941.00	5517.01	3956.33	
Jun	6412.94	3769.36	1771.27	1403.96	5533.37	3344.53	
Jul	5834.16	3208.09	1429.55	1129.12	5441.42	3315.51	
Aug	3260.00	4004.16	1414.98	1285.08	6768.98	3486.37	
Sep	2275.64	4851.15	3479.30	1044.26	6774.19	3730.03	
Oct	2231.76	5245.55	5507.50	2301.31	6827.85	4061.95	
Nov	1964.19	4118.02	5860.74	1697.81	5747.12	4644.56	
Dec		3727.62	6282.33	1651.04	4083.92	5111.61	
BAND_11	RUP60 (53,159)	JPP38 (36,139)	USP80 (14,145)	PGP51 (-3,151)	AUP06 (-19,147)	AUP04 (-38,145)	
Jan	2094.30	3314.93	3133.46	1072.41	4970.94	5239.04	
Feb	2145.10	4506.75	3902.83	1378.02	4562.98	4760.59	
Mar	3132.51	5108.17	3569.20	1203.85	5157.14	4575.97	
Apr	2912.90	5751.39	2958.88	974.16	4891.46	3838.00	
May	1543.64	5435.87	2608.91	856.95	5168.34	3251.62	
Jun	1692.41	4327.52	2450.95	1081.75	4404.44	2599.51	

Jul	1344.09	2771.69	1734.70	1232.80	4633.13	2607.77
Aug	1642.15	2930.19	1327.10	1595.67	5823.94	3161.61
Sep	2266.76	4399.47	1230.66	1279.12	6764.47	3734.94
Oct	1923.97	5494.41	1555.59	1960.01	6896.16	3707.97
Nov	1971.87	4467.91	2338.88	1466.27	6369.57	4295.07
Dec	1702.11	3344.54	2950.49	1492.73	6093.32	4370.12

BAND_12	RUP60 (53,159)	JPP38 (36,139)	USP77 (19,167)	PGP51 (-3,151)	FJP26 (-18,177)	NZP47 (-35,173)	NZP46 (-44,-176)	AUP07 (-55,159)
Jan	2094.30	3314.93	4438.66	1072.41	2852.16	5154.44	4004.14	1374.95
Feb	2145.10	4506.75	4202.98	1378.02	2503.36	4778.15	3990.75	1467.98
Mar	3132.51	5108.17	4047.37	1203.85	2219.24	4375.69	3735.34	1616.87
Apr	2912.90	5751.39	3806.54	974.16	2621.18	3734.21	3086.04	1461.07
May	1543.64	5435.87	3807.34	856.95	3110.01	3195.82	2613.18	1417.53
Jun	1692.41	4327.52	3062.28	1081.75	2896.95	2794.69	2235.33	1448.47
Jul	1344.09	2771.69	2960.37	1232.80	4037.48	2773.06	2143.54	1453.62
Aug	1642.15	2930.19	2901.42	1595.67	3984.38	2935.98	2139.04	1289.27
Sep	2266.76	4399.47	2631.80	1279.12	3434.71	3553.42	2710.81	1699.24
Oct	1923.97	5494.41	2993.84	1960.01	3923.58	3783.03	2885.71	1659.81
Nov	1971.87	4467.91	3302.66	1466.27	3342.75	4112.83	3185.48	1662.76
Dec	1702.11	3344.54	4232.63	1492.73	3656.63	4547.06	3479.65	1324.74

Table 9 Monthly averages of [7]Be concentrations used to produce global [7]Be map plot for each month (see *Figure 24* and *Figure 26*). Total average CONC per station column list [7]Be averages over all months used to normalize [7]Be concentrations.

STATION CODE	LAT	LON	January CONC	February CONC	March CONC	April CONC	May CONC	June CONC	July CONC	August CONC	September CONC	October CONC	November CONC	December CONC	TOTAL Average CONC
ARP01	-34.54	-58.47	6499.59	5786.91	5508.38	5039.02	3925.12	3555.90	3334.73	3534.15	4127.09	4778.87	5615.66	6142.53	4820.66
ARP03	-41.15	-71.16	6235.89	6184.62	5156.93	3961.07	3226.30	2231.35	2193.55	2691.80	3291.05	3907.37	4511.51	5001.55	4049.41
AUP04	-37.73	145.10	5239.04	4760.59	4575.97	3838.00	3251.62	2599.51	2607.77	3161.61	3734.94	3707.97	4295.07	4370.12	3845.18
AUP05	-67.60	62.87	6910.83	6902.20	5975.87	4538.17	3894.09	4399.94	4042.82	4268.57	4215.08	4992.57	5286.74	5619.61	5087.21
AUP06	-19.25	146.77	4970.94	4562.98	5157.14	4891.46	5168.34	4404.44	4633.13	5823.94	6764.47	6896.16	6369.57	6093.32	5477.99
AUP07	-54.50	158.95	1374.95	1467.98	1616.87	1461.07	1417.53	1448.47	1453.62	1289.27	1699.24	1659.81	1662.76	1324.74	1489.69
AUP08	-12.19	96.83	4149.89	3155.70	2882.85	3025.12	3076.86	3066.71	3178.63	3710.61	3901.75	4097.23	4163.72	3730.10	3511.60
AUP09	-12.43	130.89	3730.51	3825.44	3647.40	5035.43	5517.01	5533.37	5441.42	6768.98	6774.19	6827.85	5747.12	4083.92	5244.39
AUP10	-31.93	115.98	5473.78	5542.74	5174.26	4426.34	3956.33	3344.53	3315.51	3486.37	3730.03	4061.95	4644.56	5111.61	4355.67
BRP11	-22.99	-43.42	2986.74	3089.71	3124.07	3266.79	3664.05	3202.68	3255.42	3429.02	3474.43	3197.25	3215.45	2898.60	3233.69

CMP13	3.78	10.15	3995.16	3646.63	3021.81	2145.73	2096.94	3204.95	3431.30	2290.87	912.63	921.23	2284.18	3818.35	2647.48
CAP14	48.65	-123.45	2114.39	2360.85	2585.78	2558.21	2937.07	1901.18	1698.29	2298.73	3014.60	2513.82	2406.61	2351.45	2395.08
CAP15	74.71	-94.97	2633.64	2312.41	2865.28	3040.26	2173.75	1212.04	1771.17	1046.58	1137.76	1357.99	1860.42	2045.76	1954.75
CAP16	62.48	-114.47	2085.80	2401.26	3062.19	3686.39	4101.25	4205.93	3897.20	3008.97	2162.60	1542.08	1681.68	1905.14	2811.71
CAP17	47.59	-52.74	2353.31	2617.10	3119.37	3275.78	2540.12	2253.83	2889.07	2645.58	2928.15	1974.31	2258.37	2453.13	2609.01
CLP18	-53.14	-70.88	2230.20	2498.09	2105.95	1842.02	1587.91	1320.18	1532.21	1662.98	1666.79	1827.33	1709.37	1694.21	1806.44
CLP19	-27.13	-109.35	4598.18	5336.77	4654.36	4296.61	3772.33	3432.69	3442.94	3483.52	3805.15	4514.15	4154.82	5509.40	4250.08
CKP23	-21.20	-159.81	3019.29	3133.42	2994.51	3411.51	3701.41	3623.47	3938.65	4318.95	4042.94	4650.48	3974.12	3640.03	3704.07
FJP26	-17.76	177.45	2852.16	2503.36	2219.24	2621.18	3110.01	2896.95	4037.48	3984.38	3434.71	3923.58	3342.75	3656.63	3215.20
FRP27	-17.57	-149.57	3020.86	2989.87	3135.45	2857.09	3291.91	3473.12	3443.36	3700.38	3228.89	3677.31	3571.58	2820.35	3267.51
FRP28	16.26	-61.53	2515.16	2439.33	3401.44	3263.27	3312.16	3409.75	3193.79	2773.79	2128.73	2396.24	2604.83	2644.41	2840.24
FRP29	-20.91	55.59	2960.13	2897.81	2738.02	2963.40	3016.94	3147.98	3161.99	3275.31	3484.09	3457.96	3560.93	3541.94	3183.88
FRP30	-49.35	70.26	1766.29	1809.21	1826.75	1614.90	1404.17	1284.37	1346.91	1578.16	1508.65	1623.67	1656.23	1762.82	1598.51
FRP31	5.17	-52.69	2946.49	2922.83	3701.82	3330.92	2506.54	1713.40	1793.51	2179.95	2809.79	2446.63	1919.06	1919.69	2515.89
DEP33	47.92	7.91	3194.16	3247.49	3952.90	4665.08	5035.82	5039.49	5164.00	4724.73	4613.18	4379.95	3312.33	2872.84	4183.50
ISP34	64.13	-21.90	1955.48	2164.71	2295.59	2464.01	2405.05	1881.47	1613.57	1584.65	1439.52	1646.29	1547.95	1961.45	1913.31
JPP37	26.50	127.90	6454.76	5885.61	6314.93	5454.11	3811.98	1771.27	1429.55	1414.98	3479.30	5507.50	5860.74	6282.33	4472.25
JPP38	36.30	139.08	3314.93	4506.75	5108.17	5751.39	5435.87	4327.52	2771.69	2930.19	4399.47	5494.41	4467.91	3344.54	4321.07
KIP39	2.01	-157.39	1514.46	1753.56	1533.91	1223.55	1483.37	1787.51	2449.64	3215.40	2969.98	3223.09	2376.90	2073.67	2133.75
KWP40	29.34	47.91	4977.96	5562.25	7142.84	7240.30	7981.94	9580.85	10667.89	9546.35	8216.10	6651.92	5347.17	5062.68	7331.52
MYP42	4.48	101.37	2082.17	2513.01	2530.97	2015.90	1612.33	2419.01	2404.07	1859.23	1900.67	1833.09	1130.16	1097.36	1949.83
MRP43	18.14	-15.92	5275.30	5655.51	5377.57	5285.59	5217.61	5182.02	4980.75	4656.42	4242.89	5072.01	5725.57	5640.70	5192.66
MXP44	27.96	-114.06	6282.37	5464.28	6102.49	5140.71	5298.07	4230.25	3429.23	4154.08	5069.13	5882.94	5960.26	5804.25	5234.84
MNP45	47.89	106.33	4637.34	5141.34	5475.07	6331.39	6396.36	6299.55	6437.19	5905.78	5694.25	5137.79	4793.65	4717.52	5580.60
NZP46	-43.82	-176.48	4004.14	3990.75	3735.34	3086.04	2613.18	2235.33	2143.54	2139.04	2710.81	2885.71	3185.48	3479.65	3017.42
NZP47	-35.07	173.29	5154.44	4778.15	4375.69	3734.21	3195.82	2794.69	2773.06	2935.98	3553.42	3783.03	4112.83	4547.06	3811.53
NOP49	78.23	15.39	2172.66	2272.92	2526.83	2657.36	2003.86	1325.83	1139.94	1191.99	1399.96	1126.26	1503.28	1957.89	1773.23
PAP50	8.98	-79.53	3218.08	3608.43	4248.16	3487.77	2471.71	1372.74	1602.91	1440.29	1148.89	1185.30	1862.71	2717.95	2363.75
PGP51	-2.58	150.81	1072.41	1378.02	1203.85	974.16	856.95	1081.75	1232.80	1595.67	1279.12	1960.01	1466.27	1492.73	1299.48
PHP52	14.58	121.37	2473.40	3024.17	3702.74	3434.20	1941.00	1403.96	1129.12	1285.08	1044.26	2301.31	1697.81	1651.04	2090.67

PTP53	37.74	-25.70	3528.52	3930.38	3935.81	4375.39	4282.34	4332.39	4317.24	3819.10	3598.04	3326.08	3728.05	3511.41	3890.40
RUP54	58.59	49.41	2400.35	2409.08	2550.60	3536.22	5179.34	4865.40	4309.24	4462.26	2810.46	2118.66	2116.56	1806.81	3213.75
RUP56	59.62	112.64	3959.53	4676.61	5080.34	6277.82	6313.14	6412.94	5834.16	3260.00	2275.64	2231.76	1964.19		4389.65
RUP58	44.15	132.00	4334.77	4655.57	5626.19	5842.95	4213.58	3769.36	3208.09	4004.16	4851.15	5245.55	4118.02	3727.62	4466.42
RUP59	53.94	84.79	3014.77	2843.73	3932.58	5714.48	5945.43	6363.60	5685.39	4801.68	4323.45	3863.37	3046.06	3196.26	4394.23
RUP60	53.05	158.78	2094.30	2145.10	3132.51	2912.90	1543.64	1692.41	1344.09	1642.15	2266.76	1923.97	1971.87	1702.11	2030.98
RUP61	56.74	37.25	2084.88	2881.24	3018.24	4179.89	5490.10	5199.63	5592.49	4734.93	3029.30	2596.88	2310.72	2246.99	3613.77
23255	59.41	17.95	2276.00	2372.06	2654.25	3165.75	3552.15	3535.04	3432.31	3530.58	2635.60	2270.87	1920.30	2123.58	2789.04
TZP64	-6.78	39.20	5829.26	5647.72	3850.91	3443.16	4286.13	4572.52	4501.36	4376.59	4610.74	4341.54	4222.72	4776.14	4538.23
GBP66	-7.30	72.40	2971.75	3549.76	2959.27	2690.87	2996.12	2615.82	2609.03	2623.81	2734.13	2873.41	2645.14	2493.23	2813.53
GBP67	-15.94	-5.67	5884.30	5214.27	4738.23	4481.31	4500.98	4369.42	3945.86	3800.80	5014.97	5450.15	5724.29	5731.34	4904.66
GBP68	-37.07	-12.31	3895.33	4200.23	4313.73	3490.78	2941.68	2740.05	2765.04	2595.33	2869.52	2797.81	3212.31	3542.49	3280.36
USP70	38.67	-121.36	4628.29	5007.20	5377.73	5256.44	5689.19	4438.14	4214.75	4481.83	5898.39	5532.60	4728.29	4205.56	4954.87
USP71	55.34	-160.49	2604.41	2652.11	3449.52	2934.19	1815.00	1220.09	888.55	1449.53	1885.64	2043.37	2436.15	2517.87	2158.04
USP72	28.10	-80.65	6545.96	6686.32	7567.17	7736.43	7178.47	4986.99	4540.62	4297.34	4947.11	6140.74	6346.14	6266.94	6103.35
USP73	-64.77	-64.05	1720.50	1702.45	1492.12	1580.25	1269.11	1468.84	1738.56	1549.95	1405.43	1590.88	1551.69	1762.50	1569.36
USP74	37.17	-99.77	4923.26	5004.24	5798.25	6627.51	6333.14	6469.83	5756.50	5925.84	5684.79	5318.30	5020.11	4431.33	5607.76
USP75	38.00	78.40	4372.26	5006.42	5672.30	6358.87	5993.93	5840.84	5631.61	5385.30	4903.20	4495.74	4502.09	4275.53	5203.17
USP76	64.67	-147.10	2357.73	3182.65	4056.91	4437.61	5307.92	3827.01	3082.07	2595.43	2423.57	1731.79	1873.67	2197.37	3089.48
USP77	19.29	166.61	4438.66	4202.98	4047.37	3806.54	3807.34	3062.28	2960.37	2901.42	2631.80	2993.84	3302.66	4232.63	3532.32
USP78	28.22	-177.37	5431.19	5030.50	4995.29	5130.01	4629.16	3704.91	3051.53	3341.17	3644.99	4456.92	4395.73	4557.28	4364.06
USP79	21.52	-157.99	3544.98	3689.02	3483.57	3525.92	3539.88	2799.79	2647.57	2910.82	2773.95	2867.31	2762.70	2953.82	3124.94
USP80	13.57	144.93	3133.46	3902.83	3569.20	2958.88	2608.91	2450.95	1734.70	1327.10	1230.66	1555.59	2338.88	2950.49	2480.14

Table 10 Normalized monthly averages of ⁷Be concentrations used to produce global ⁷Be map plot for each month (see Figure *25* and Figure *27*).

STATION CODE	LAT	LON	January NORM	February NORM	March NORM	April NORM	May NORM	June NORM	July NORM	August NORM	September NORM	October NORM	November NORM	December NORM
ARP01	-34.54	-58.47	1.348	1.200	1.143	1.045	0.814	0.738	0.692	0.733	0.856	0.991	1.165	1.274
ARP03	-41.15	-71.16	1.540	1.527	1.274	0.978	0.797	0.551	0.542	0.665	0.813	0.965	1.114	1.235
AUP04	-37.73	145.10	1.362	1.238	1.190	0.998	0.846	0.676	0.678	0.822	0.971	0.964	1.117	1.137
AUP05	-67.60	62.87	1.358	1.357	1.175	0.892	0.765	0.865	0.795	0.839	0.829	0.981	1.039	1.105

AUP06	-19.25	146.77	0.907	0.833	0.941	0.893	0.943	0.804	0.846	1.063	1.235	1.259	1.163	1.112
AUP07	-54.50	158.95	0.923	0.985	1.085	0.981	0.952	0.972	0.976	0.865	1.141	1.114	1.116	0.889
AUP08	-12.19	96.83	1.182	0.899	0.821	0.861	0.876	0.873	0.905	1.057	1.111	1.167	1.186	1.062
AUP09	-12.43	130.89	0.711	0.729	0.695	0.960	1.052	1.055	1.038	1.291	1.292	1.302	1.096	0.779
AUP10	-31.93	115.98	1.257	1.273	1.188	1.016	0.908	0.768	0.761	0.800	0.856	0.933	1.066	1.174
BRP11	-22.99	-43.42	0.924	0.955	0.966	1.010	1.133	0.990	1.007	1.060	1.074	0.989	0.994	0.896
CMP13	3.78	10.15	1.509	1.377	1.141	0.810	0.792	1.211	1.296	0.865	0.345	0.348	0.863	1.442
CAP14	48.65	-123.45	0.883	0.986	1.080	1.068	1.226	0.794	0.709	0.960	1.259	1.050	1.005	0.982
CAP15	74.71	-94.97	1.347	1.183	1.466	1.555	1.112	0.620	0.906	0.535	0.582	0.695	0.952	1.047
CAP16	62.48	-114.47	0.742	0.854	1.089	1.311	1.459	1.496	1.386	1.070	0.769	0.548	0.598	0.678
CAP17	47.59	-52.74	0.902	1.003	1.196	1.256	0.974	0.864	1.107	1.014	1.122	0.757	0.866	0.940
CLP18	-53.14	-70.88	1.235	1.383	1.166	1.020	0.879	0.731	0.848	0.921	0.923	1.012	0.946	0.938
CLP19	-27.13	-109.35	1.082	1.256	1.095	1.011	0.888	0.808	0.810	0.820	0.895	1.062	0.978	1.296
CKP23	-21.20	-159.81	0.815	0.846	0.808	0.921	0.999	0.978	1.063	1.166	1.091	1.256	1.073	0.983
FJP26	-17.76	177.45	0.887	0.779	0.690	0.815	0.967	0.901	1.256	1.239	1.068	1.220	1.040	1.137
FRP27	-17.57	-149.57	0.925	0.915	0.960	0.874	1.007	1.063	1.054	1.132	0.988	1.125	1.093	0.863
FRP28	16.26	-61.53	0.886	0.859	1.198	1.149	1.166	1.201	1.124	0.977	0.749	0.844	0.917	0.931
FRP29	-20.91	55.59	0.930	0.910	0.860	0.931	0.948	0.989	0.993	1.029	1.094	1.086	1.118	1.112
FRP30	-49.35	70.26	1.105	1.132	1.143	1.010	0.878	0.803	0.843	0.987	0.944	1.016	1.036	1.103
FRP31	5.17	-52.69	1.171	1.162	1.471	1.324	0.996	0.681	0.713	0.866	1.117	0.972	0.763	0.763
DEP33	47.92	7.91	0.764	0.776	0.945	1.115	1.204	1.205	1.234	1.129	1.103	1.047	0.792	0.687
ISP34	64.13	-21.90	1.022	1.131	1.200	1.288	1.257	0.983	0.843	0.828	0.752	0.860	0.809	1.025
JPP37	26.50	127.90	1.443	1.316	1.412	1.220	0.852	0.396	0.320	0.316	0.778	1.231	1.310	1.405
JPP38	36.30	139.08	0.767	1.043	1.182	1.331	1.258	1.001	0.641	0.678	1.018	1.272	1.034	0.774
KIP39	2.01	-157.39	0.710	0.822	0.719	0.573	0.695	0.838	1.148	1.507	1.392	1.511	1.114	0.972
KWP40	29.34	47.91	0.679	0.759	0.974	0.988	1.089	1.307	1.455	1.302	1.121	0.907	0.729	0.691
MYP42	4.48	101.37	1.068	1.289	1.298	1.034	0.827	1.241	1.233	0.954	0.975	0.940	0.580	0.563
MRP43	18.14	-15.92	1.016	1.089	1.036	1.018	1.005	0.998	0.959	0.897	0.817	0.977	1.103	1.086
MXP44	27.96	-114.06	1.200	1.044	1.166	0.982	1.012	0.808	0.655	0.794	0.968	1.124	1.139	1.109
MNP45	47.89	106.33	0.831	0.921	0.981	1.135	1.146	1.129	1.153	1.058	1.020	0.921	0.859	0.845
NZP46	-43.82	-176.48	1.327	1.323	1.238	1.023	0.866	0.741	0.710	0.709	0.898	0.956	1.056	1.153
NZP47	-35.07	173.29	1.352	1.254	1.148	0.980	0.838	0.733	0.728	0.770	0.932	0.993	1.079	1.193
NOP49	78.23	15.39	1.225	1.282	1.425	1.499	1.130	0.748	0.643	0.672	0.789	0.635	0.848	1.104
PAP50	8.98	-79.53	1.361	1.527	1.797	1.476	1.046	0.581	0.678	0.609	0.486	0.501	0.788	1.150
PGP51	-2.58	150.81	0.825	1.060	0.926	0.750	0.659	0.832	0.949	1.228	0.984	1.508	1.128	1.149
PHP52	14.58	121.37	1.183	1.447	1.771	1.643	0.928	0.672	0.540	0.615	0.499	1.101	0.812	0.790
PTP53	37.74	-25.70	0.907	1.010	1.012	1.125	1.101	1.114	1.110	0.982	0.925	0.855	0.958	0.903
RUP54	58.59	49.41	0.747	0.750	0.794	1.100	1.612	1.514	1.341	1.388	0.875	0.659	0.659	0.562
RUP56	59.62	112.64	0.902	1.065	1.157	1.430	1.438	1.461	1.329	0.743	0.518	0.508	0.447	0.000
RUP58	44.15	132.00	0.971	1.042	1.260	1.308	0.943	0.844	0.718	0.897	1.086	1.174	0.922	0.835
RUP59	53.94	84.79	0.686	0.647	0.895	1.300	1.353	1.448	1.294	1.093	0.984	0.879	0.693	0.727

RUP60	53.05	158.78	1.031	1.056	1.542	1.434	0.760	0.833	0.662	0.809	1.116	0.947	0.971	0.838
RUP61	56.74	37.25	0.577	0.797	0.835	1.157	1.519	1.439	1.548	1.310	0.838	0.719	0.639	0.622
SEP63	59.41	17.95	0.816	0.850	0.952	1.135	1.274	1.267	1.231	1.266	0.945	0.814	0.689	0.761
TZP64	-6.78	39.20	1.284	1.244	0.849	0.759	0.944	1.008	0.992	0.964	1.016	0.957	0.930	1.052
GBP66	-7.30	72.40	1.056	1.262	1.052	0.956	1.065	0.930	0.927	0.933	0.972	1.021	0.940	0.886
GBP67	-15.94	-5.67	1.200	1.063	0.966	0.914	0.918	0.891	0.805	0.775	1.022	1.111	1.167	1.169
GBP68	-37.07	-12.31	1.187	1.280	1.315	1.064	0.897	0.835	0.843	0.791	0.875	0.853	0.979	1.080
USP70	38.67	-121.36	0.934	1.011	1.085	1.061	1.148	0.896	0.851	0.905	1.190	1.117	0.954	0.849
USP71	55.34	-160.49	1.207	1.229	1.598	1.360	0.841	0.565	0.412	0.672	0.874	0.947	1.129	1.167
USP72	28.10	-80.65	1.073	1.096	1.240	1.268	1.176	0.817	0.744	0.704	0.811	1.006	1.040	1.027
USP73	-64.77	-64.05	1.096	1.085	0.951	1.007	0.809	0.936	1.108	0.988	0.896	1.014	0.989	1.123
USP74	37.17	-99.77	0.878	0.892	1.034	1.182	1.129	1.154	1.027	1.057	1.014	0.948	0.895	0.790
USP75	38.00	78.40	0.840	0.962	1.090	1.222	1.152	1.123	1.082	1.035	0.942	0.864	0.865	0.822
USP76	64.67	-147.10	0.763	1.030	1.313	1.436	1.718	1.239	0.998	0.840	0.784	0.561	0.606	0.711
USP77	19.29	166.61	1.257	1.190	1.146	1.078	1.078	0.867	0.838	0.821	0.745	0.848	0.935	1.198
USP78	28.22	-177.37	1.245	1.153	1.145	1.176	1.061	0.849	0.699	0.766	0.835	1.021	1.007	1.044
USP79	21.52	-157.99	1.134	1.181	1.115	1.128	1.133	0.896	0.847	0.931	0.888	0.918	0.884	0.945
USP80	13.57	144.93	1.263	1.574	1.439	1.193	1.052	0.988	0.699	0.535	0.496	0.627	0.943	1.190

Table 11 [7]Be concentrations used to produce equatorial band plots (see Figure _28_).

Equatorial band monthly averaged values over all available years	10°	39°	72°	101°	131°	151°	-157°	-80°	-53°
Jan	3995.16	5829.26	2971.75	2082.17	3730.51	1072.41	1514.46	3218.08	2946.49
Feb	3646.63	5647.72	3549.76	2513.01	3825.44	1378.02	1753.56	3608.43	2922.83
Mar	3021.81	3850.91	2959.27	2530.97	3647.4	1203.85	1533.91	4248.16	3701.82
Apr	2145.73	3443.16	2690.87	2015.9	5035.43	974.16	1223.55	3487.77	3330.92
May	2096.94	4286.13	2996.12	1612.33	5517.01	856.95	1483.37	2471.71	2506.54
Jun	3204.95	4572.52	2615.82	2419.01	5533.37	1081.75	1787.51	1372.74	1713.4
Jul	3431.3	4501.36	2609.03	2404.07	5441.42	1232.8	2449.64	1602.91	1793.51
Aug	2290.87	4376.59	2623.81	1859.23	6768.98	1595.67	3215.4	1440.29	2179.95
Sep	912.63	4610.74	2734.13	1900.67	6774.19	1279.12	2969.98	1148.89	2809.79
Oct	921.23	4341.54	2873.41	1833.09	6827.85	1960.01	3223.09	1185.3	2446.63
Nov	2284.18	4222.72	2645.14	1130.16	5747.12	1466.27	2376.9	1862.71	1919.06

Dec	3818.35	4776.14	2493.23	1097.36	4083.92	1492.73	2073.67	2717.95	1919.69
Equatorial band monthly averaged normalized values over all available years	10°	39°	72°	101°	131°	151°	-157°	-80°	-53°
Jan	1.509	1.284	1.056	1.068	0.711	0.825	0.71	1.361	1.171
Feb	1.377	1.244	1.262	1.289	0.729	1.06	0.822	1.527	1.162
Mar	1.141	0.849	1.052	1.298	0.695	0.926	0.719	1.797	1.471
Apr	0.81	0.759	0.956	1.034	0.96	0.75	0.573	1.476	1.324
May	0.792	0.944	1.065	0.827	1.052	0.659	0.695	1.046	0.996
Jun	1.211	1.008	0.93	1.241	1.055	0.832	0.838	0.581	0.681
Jul	1.296	0.992	0.927	1.233	1.038	0.949	1.148	0.678	0.713
Aug	0.865	0.964	0.933	0.954	1.291	1.228	1.507	0.609	0.866
Sep	0.345	1.016	0.972	0.975	1.292	0.984	1.392	0.486	1.117
Oct	0.348	0.957	1.021	0.94	1.302	1.508	1.511	0.501	0.972
Nov	0.863	0.93	0.94	0.58	1.096	1.128	1.114	0.788	0.763
Dec	1.442	1.052	0.886	0.563	0.779	1.149	0.972	1.15	0.763
Equatorial band monthly averaged values over El-Niño years	10°	39°	72°	101°	131°	151°	-157°	-80°	-53°
Jan	3835.7	6208.72	3621.87	2396.98	4396.04	899.08	1598.88	3332.89	3233
Feb	4012.44	5248.04	4187.76	3207	4968.69	1319.35	1628.71	3870.36	2885.13
Mar	3458.8	4191.99	3987.08	3636.33	4760.09	1322.73	1416.95	4158.74	3482.66
Apr	2962.87	3326.44	2943.65	2288.09	4327.23	858.95	1237.79	2895.97	3333.75
May	2651.55	4800.68	2507.38	1492.97	5448.34	862.83	1865.16	2688.36	1555
Jun	2472.24	4631.19	2680.92	2509.2	5544.08	1237.95	1621.22	1642.68	2747.04
Jul	3814.82	4593.38	2785.86	2079.41	5667.52	1344.67	2370.57	1951.15	2107.56
Aug	1010.97	4530.22	2871.2	1575.98	7186.03	2404.52	3736.26	1895.42	2591.04
Sep	699.53	5360.33	2713.13	2209.97	7409.18	1201.09	3180.05	1755.25	3253.8
Oct	789.31	4867.52	3224.63	2254.77	7827.05	2415.28	3583.21	1311.92	2391.19
Nov	2354.82	4269.79	2918.96	1422.23	6501.09	1332.02	3182.96	1723.37	1725.12

Dec	4408.19	4728.53	2575.91	1110.2	4792.71	1875.22	2343.48	2552.82	2368.11
Equatorial band monthly averaged normalized values over El-Niño years	10°	39°	72°	101°	131°	151°	-157°	-80°	-53°
Jan	1.418	1.313	1.174	1.099	0.766	0.632	0.691	1.343	1.225
Feb	1.483	1.11	1.358	1.47	0.866	0.927	0.704	1.56	1.093
Mar	1.278	0.886	1.292	1.667	0.83	0.93	0.612	1.676	1.319
Apr	1.095	0.703	0.954	1.049	0.754	0.604	0.535	1.167	1.263
May	0.98	1.015	0.813	0.684	0.95	0.606	0.806	1.083	0.589
Jun	0.914	0.979	0.869	1.15	0.967	0.87	0.701	0.662	1.041
Jul	1.41	0.971	0.903	0.953	0.988	0.945	1.025	0.786	0.798
Aug	0.374	0.958	0.931	0.722	1.253	1.69	1.615	0.764	0.982
Sep	0.259	1.133	0.879	1.013	1.292	0.844	1.374	0.707	1.233
Oct	0.292	1.029	1.045	1.033	1.365	1.698	1.549	0.529	0.906
Nov	0.87	0.903	0.946	0.652	1.133	0.936	1.376	0.694	0.654
Dec	1.629	1	0.835	0.509	0.836	1.318	1.013	1.029	0.897
Equatorial band monthly averaged values over non El-Niño years	10°	39°	72°	101°	131°	151°	-157°	-80°	-53°
Jan	4022.97	5670.98	2497.12	1969.37	3354.46	1155.01	1497.58	3163.85	2863.63
Feb	3585.66	5857.94	3078.76	2347.2	3232.04	1417.97	1776.74	3508.32	2938.93
Mar	2944.4	3760.72	2556.02	2218.26	3259.84	1154.61	1577.28	4270.24	3792.54
Apr	2060.22	3480.18	2613.88	1909.95	5204.37	1004.22	1217.07	3631.46	3329.65
May	1991.47	4144.88	3142.98	1659	5547.28	854.95	1307.81	2418.4	2820.55
Jun	3242.08	4520.15	2595.84	2514.51	5454.52	943.68	1714.89	1373.98	1588.27
Jul	3343.63	4474.56	2553.66	2548.08	5341.21	1202.24	2467.02	1525.1	1740.36
Aug	2548.51	4346.88	2439.48	1974.12	6541.51	1291.26	3121.53	1315.24	2079.68
Sep	943.22	4499.96	2741.29	1825.55	6484.36	1300.62	2936.28	1069.11	2745.28
Oct	964.36	4169	2637.66	1660.27	6117.76	1672.17	3159.42	1149.12	2463

Nov	2265.4	4205.79	2507.44	986.56	5254.57	1576.69	2222.1	1897.18	1973.91
Dec	3718.44	4792.95	2439.35	1091.1	3660.98	1321	2003.38	2767.09	1785.16
Equatorial band monthly averaged normalized values over non El-Niño years	10°	39°	72°	101°	131°	151°	-157°	-80°	-53°
Jan	1.526	1.262	0.942	1.041	0.677	0.931	0.719	1.352	1.141
Feb	1.36	1.304	1.162	1.241	0.652	1.142	0.853	1.499	1.171
Mar	1.117	0.837	0.964	1.172	0.658	0.93	0.757	1.824	1.511
Apr	0.782	0.774	0.986	1.009	1.05	0.809	0.584	1.551	1.327
May	0.756	0.922	1.186	0.877	1.12	0.689	0.628	1.033	1.124
Jun	1.23	1.006	0.979	1.329	1.101	0.76	0.823	0.587	0.633
Jul	1.269	0.996	0.964	1.347	1.078	0.969	1.184	0.652	0.693
Aug	0.967	0.967	0.92	1.043	1.32	1.04	1.498	0.562	0.829
Sep	0.358	1.001	1.034	0.965	1.309	1.048	1.409	0.457	1.094
Oct	0.366	0.928	0.995	0.878	1.235	1.347	1.516	0.491	0.981
Nov	0.859	0.936	0.946	0.521	1.061	1.27	1.067	0.81	0.786
Dec	1.411	1.067	0.92	0.577	0.739	1.064	0.962	1.182	0.711

Table 12. For each year the cross-point day # and predicted monsoon onset day # is given based on [7]Be trans-equatorial approach method A, B, C and D. correlation between IMD monsoon onset day reaches 0.90 with method C. Kerala, India is the reference region for monsoon onset.

Year	IMD monsoon onset	Method A		Method B		Method C		Method D Averaged predicted monsoon onset (Method A, B and C)
		cross point 2 (CP2)	Predicted monsoon onset	cross point 1 (CP1)	Predicted monsoon onset	cross point 1 (CP1)	Predicted monsoon onset	
2009	143	253	n/a	91	143	109	141	142
2010	151	257	154	93	145	116	148	149
2011	149	262	158	94	146	117	149	151
2012	157	245	163	106	158	123	155	159
2013	152	254	146	102	154	123	155	152

2014	157	254	155	110	162	128	160	159
2015	156	252	155	103	155	123	154	155
2016	160	250	153	104	156	128	160	156
2017	157	246	151	110	162	140	167	162
2018	145	n/a	147	90	142	106	137	142
Correlation between IMD monsoon onset and predicted onset using method A, B, C and D over all available years (2009-2018)	0.37		0.89		0.85		0.93	

Table 13 For each station the ^{7}Be % of yearly growth versus the overall average is calculated (the growth is based on 1.001 increase of the normalized averaged time series). % values are rounded to zero decimals. Dataset is based on 120 days averaged normalized ^{7}Be concentration corrected from cosmic rays.

Treaty n.	2003	2004	2005	2006	2007	2008	2009	2010	2011	2012	2013	2014	2015	2016	2017	2018	2019
RN01	-16.68	-8.53	-0.32	-0.71	-5.06	-4.00	1.21	-3.48	-2.75	-2.62	3.90	-3.00	2.76	5.29	9.20	5.89	18.91
RN03		-18.18	-6.14	10.17	20.95		-2.48	-0.85	-3.55	2.98	-10.13	-14.54	0.03	3.63	-3.86	1.34	20.62
RN04	-15.95	-8.59	-13.42	-11.41	2.01	-1.76	0.76	10.98	-1.76	-3.53	2.89	0.06	-0.51	8.08	9.41	6.88	15.85
RN05											-4.46	-4.75	-8.62	-5.40	-5.44	10.12	18.55
RN06	11.71	2.68	2.41	0.03	-3.43	-8.59	-2.45	-6.60	-21.72	-10.12	-4.34	-0.48	2.47	12.86	15.59	11.24	-1.24
RN07											-2.88	-6.10	0.81	4.28	-3.30	-1.70	-1.06	9.95
RN08	50.12	49.60	19.69	7.29	0.19	-11.33	-6.20	-9.29	-6.36	-20.46	-25.38	-12.76	-4.39	-26.61	-19.15	2.19	12.86
RN09	18.45	-2.69	1.90	10.11	0.36	17.05	-13.60	-0.03	-19.02	-5.19	-0.65	0.49	1.99	0.30	-1.39	3.85	-11.94
RN10	-22.13	-21.03	-11.23	-8.20	0.88	1.05	5.05	13.64	5.39	7.76	2.10	1.37	4.07	3.24	4.93	0.45	12.66
RN11	18.66	-0.85	-6.59	6.84	0.66	8.63	-8.74	4.42	-3.20	-2.30	-0.71	-3.02	2.52	-1.08	-1.91	-5.80	-7.54
RN13						5.66	-15.52	7.09	15.33	-8.96	-3.72	3.49		-10.67	3.70	-1.74	5.34
RN14							20.37	-1.78	-16.78	-1.29	-13.17	2.03	11.70	-5.59	-7.37	-1.38	13.25
RN15			-6.77	-12.87	-21.80	7.91	-14.74	-15.03	17.04	20.62	1.46	-12.05	0.51	15.03	8.97	3.18	8.56
RN16	-15.09	-11.56	-9.67	2.52	3.77	-0.61	-5.03	10.79	2.38	4.41	-1.15	-1.69	1.36	5.28	7.92	1.42	4.95
RN17				-0.83	3.11	-6.20	4.98	-15.45	-6.79	6.88	4.14	2.47	1.42	3.30	0.80	6.23	-4.06

RN18	-9.43	-10.34	11.95		-13.03	-23.22	-21.01	-18.10	14.21	22.98	-10.46	-8.48	8.41	10.76	14.12	20.39	11.26
RN19	-11.64		-23.58	-8.34	-3.89				21.86	28.74	19.97	-7.33	0.09	5.12	-4.08	-9.61	-7.31
RN23	5.87	-7.16	0.66	-0.64	-0.21	-5.15	-1.78	2.72	4.37	-0.08	1.27	2.95	3.52	8.63	1.22	-6.71	-9.48
RN26			12.65	7.76	-7.03	-6.08	8.13	8.02	-17.07	-7.09	9.49	7.79	0.48	7.22	0.11	-10.45	-13.94
RN27	-7.68	-13.22	-20.29	13.27	18.78	33.50	34.40			17.23	-8.89	-9.87	-8.58	-8.76	-10.55	-13.22	-16.13
RN28			-7.38	3.23	13.74	8.51	-3.39		-13.59	-11.72	-0.02	7.07	2.72	0.28	-4.07	9.07	-4.46
RN29		-17.59	-17.58	-11.66	1.07	-15.04	-15.94	-2.13	-8.13	-9.53	10.21	11.32	5.78	10.76	16.10	18.66	23.70
RN30				6.98	-9.24	3.04	-0.24	-11.48	4.51	-0.42	-12.52		6.89	6.32	-2.46	4.92	3.70
RN31			-14.60	-1.00	-7.88	26.10	10.77	-13.94	-21.74	-17.85	-3.82	6.84	20.69	-13.72	-32.25	14.21	48.17
RN33					2.15	10.75	11.07	9.17	-4.41	-8.57	-18.02	-3.94	-10.82	-1.35	3.62	7.31	3.04
RN34	-10.41	10.08			-11.48	7.17		13.28	13.31	9.97	-4.65	-17.47	-13.21	-3.70	4.34	-10.23	13.00
RN37					-18.91	-14.66	-15.79	-18.94	-6.37	-22.84	8.56	4.27	-10.16	23.34	23.13	17.48	30.89
RN38	-3.13	-0.19	13.85	-6.83	1.17	16.31	13.23	-21.99	-10.95	-13.73	6.30	0.75	-7.06	-3.57	2.53	-3.48	16.79
RN39					24.06	-15.99	5.01	-6.22	-9.44	-6.15	48.94	-7.11	-16.67		2.41	5.12	-23.94
RN40		32.16	-1.71	-27.81	-7.40	-28.61	-46.47	-45.48	-6.98	15.15	-23.92		28.35	16.17	31.76	23.20	41.61
RN42							-7.28	-12.10	-9.31	-9.29	-1.10	1.91	18.80	19.26	-16.69	-4.27	20.07
RN43				-0.14	9.52	7.19	3.37	7.86	10.63	22.74	-17.22	-23.16	-21.94	-14.28	-3.77	4.30	14.90
RN44									-10.51	3.70	-10.25	-0.87	9.18	-1.52	-5.70	10.52	5.45
RN45	-16.28	-8.67	-23.79	-18.56	-18.39	0.44	-0.54	-0.69	1.80	-6.93	-20.47	15.24	9.92	28.14	14.84	18.04	25.91
RN46	-20.14	-3.24	6.06	-5.44	3.96	6.50	-3.24	-8.53	-8.45	7.54	5.49	0.74	-2.83	9.54	-3.84	-0.56	16.45
RN47	-22.43	-7.55	2.09	6.82	13.71	8.41	3.10	-11.82	-1.47	-2.62	1.97	-5.93	-0.97	3.32	3.35	2.82	7.21
RN49	-8.48	37.11			-3.66	3.81	11.25	8.44	-32.92	-15.61	7.84	-5.59	4.25	-11.49	-4.29	-5.60	14.93
RN50			-32.53	17.97	3.75	6.23	24.51	-26.02	-6.22	-8.91	2.48	5.42	10.62	2.63	-9.82	-10.08	19.98
RN51	11.15	4.64	22.71	-24.44	-11.66	3.28		26.93	-0.11	-14.41	-22.15	-19.16	30.13	-15.80	-3.27	7.95	4.19
RN52				17.24	11.28	-25.26	-1.57	-50.78	-16.28	-5.55	12.98	14.60	28.73	-2.08	-6.12	-9.29	32.09
RN53									-7.77	-17.17	-12.57	-13.89	-6.40	1.52	-1.74	29.50	28.52
RN54						-15.39			5.60	3.10	17.02	-4.56	0.24	8.16	-16.08	4.12	-2.21
RN58								1.69	-1.65	-9.47	-1.52	4.50	4.24	0.74	10.95	-3.60	-5.89
RN59					3.79	6.81	18.71	11.72	14.67	19.19	-3.53		-17.04	-11.04	-19.03	-21.31	-2.94
RN60					-12.78	8.49	12.09	-2.72	11.15	0.17	-21.28	-1.87	-4.29	-17.49	15.38	13.16	

Treaty number	2003	2004	2005	2006	2007	2008	2009	2010	2011	2012	2013	2014	2015	2016	2017	2018	2019
RN61							14.93	28.14	5.45	-6.39	0.90	5.05	-12.33	-20.73	-35.54	13.28	7.23
RN63	-5.73	-4.05	-5.49		2.25	-1.35	-4.05	1.26	-0.89	-6.44	-4.99	5.43	-4.53	-9.46	-2.30	18.01	22.35
RN64					-12.90	3.32	4.34	-1.61	-0.96	1.92	-4.24	-7.70	9.28	-1.05	-6.91	2.20	14.32
RN66		1.00	7.22	19.30	6.85	4.63	-2.23	-23.69	-19.13	-14.02	3.38	6.30	54.08	-8.71	-3.41	-16.55	-15.02
RN67					-9.52	2.52	0.48	19.62	11.34	-2.33	-0.19	-11.97	0.39	2.93	-11.18	-10.12	8.01
RN68		-2.11	24.99	7.06	-5.80	-15.41	-4.07	-3.94	3.23	-0.67	-4.96	-7.66	-0.45	1.63	2.71	5.06	0.40
RN70		-1.55	-9.64		3.36	10.04	9.25	-12.17	-13.52	8.32	-2.26	-0.26	11.44	7.27	3.49	-3.14	-10.63
RN71					-2.60	17.45	5.49	-9.00	7.50	-4.53	16.41	10.23	-6.23	-8.05	27.63	-32.18	-22.11
RN72		-12.06	3.03	10.70	13.00	7.38	8.50	2.86	5.05	-2.01	-9.04	-7.30	-4.81	-0.10	-10.12	-1.25	-3.84
RN73				14.86	5.82	-12.45	-7.33	-6.15	-16.56	-12.60	3.27	-1.39	2.95	-2.92	24.13	-6.19	14.56
RN74	-12.28	-2.74	-7.61	-3.65	2.42	1.35	5.46	-6.27	0.41	14.63	3.11	0.36	6.94	-5.30	5.62	3.27	-5.71
RN75	-17.77	-11.44	-5.08	9.67	17.59	10.26	-0.18	-16.22	-9.18	10.37	4.45	10.05	1.92	-2.97	2.21	-5.96	2.30
RN76					35.07	-4.36	15.07	-5.11	-5.80	-17.04	-1.51	-0.10	-5.18	-21.26	-7.87	6.26	11.83
RN77						-10.44	-1.33	2.80	4.55	2.09	4.86	-3.56	7.39	2.76	0.12	0.69	-9.94
RN78							-22.13	-0.76	-14.31	-16.27	1.31	0.55	5.13	6.07	19.31	5.23	15.86
RN79			-7.14	-4.87	-10.41	-2.87	-6.99	3.16	-3.79	-4.03	2.57	-7.27	1.33	-0.88	20.99	-0.18	20.36
RN80						-8.89	-3.74	7.28	-10.70	-1.93	4.45	-7.01	10.96	0.67	0.36	-5.58	14.13

Table 14 N. of days above average during which ^{7}Be activity concentrations are above 1.001 absolute value (1.001 based on overall averaged normalised data time series). This period indicates the extended "warm period" for each year between 2003 and 2019. High levels of concentration are indicators for high tropopause which is a proxy for warmer tropospheric temperatures. Dataset is based on 120 days averaged normalized ^{7}Be concentration corrected from cosmic rays. N. of days are rounded to zero decimals.

Treaty number	2003	2004	2005	2006	2007	2008	2009	2010	2011	2012	2013	2014	2015	2016	2017	2018	2019
RN01		-33.88	8.12	34.12	-19.88	-25.88	25.12	1.12	11.12	-13.88	28.12	-9.88	8.12	33.12	74.12	15.12	36.12
RN03		-51.41	14.59	98.59	45.59			30.59	49.59	34.59	-0.41	-23.41	38.59	75.59	20.59	38.59	40.59
RN04	-162.65	-14.65	-114.65	-31.65	34.35	-12.65	36.35	45.35	21.35	-3.65	11.35	14.35	42.35	37.35	65.35	13.35	18.35
RN05											15.76	64.76	76.76	82.76	82.76	150.76	148.76
RN06	-50.06	-7.06	27.94	-6.06	-6.06	-83.06	-15.06	-97.06	-90.06	-61.06	-14.06	9.94	44.94	192.94	105.94	121.94	-74.06
RN07										25.06	-28.94	110.06	195.06	61.06	57.06	82.06	155.06

RN08	-30.47	218.53	214.53	44.53	54.53	-104.47	28.53	-17.47	-22.47	-135.47	-140.47	5.53	0.53	-88.47	-98.47	34.53	36.53
RN09	-54.35	11.65	36.65	-1.35	17.65	109.65	-55.35	30.65	-52.35	7.65	-6.35	-0.35	27.65	-6.35	19.65	39.65	-124.35
RN10			-84.59	-78.59	14.41	33.41	37.41	69.41	112.41	37.41	14.41	1.41	40.41	8.41	77.41	14.41	17.41
RN11	-51.18	-47.18	-110.18	165.82	47.82	158.82	-35.18	117.82	2.82	-47.18	6.82	-38.18	117.82	-4.18	20.82	-145.18	
RN13						99.65	1.65	150.65	139.65	-8.35	53.65	-1.35		-35.35	121.65	26.65	23.65
RN14						-91.59	83.41			128.41	5.41	125.41	223.41	32.41	9.41	103.41	91.41
RN15			25.24	-124.76	-120.76	34.24	-14.76	-45.76	99.24	31.24	23.24	-27.76	82.24	118.24	71.24	92.24	12.24
RN16	-125.65	-36.65	-37.65	30.35	8.35	2.35	12.35	37.35	8.35	31.35	21.35	-8.65	1.35	41.35	30.35	10.35	-26.65
RN17				-92.24	76.76	-17.24	62.76	-131.24	-42.24	133.76	85.76	85.76	10.76	71.76	30.76	162.76	-35.24
RN18	-129.94	-104.94	70.06		-44.94				141.06	-72.94	-24.94	-24.94	108.06	195.06	95.06	228.06	113.06
RN19				5.12	60.12				-18.88	235.12	79.12	-57.88	108.12	118.12	92.12	-46.88	1.12
RN23	-63.76	-48.76	51.24	15.24	11.24	-24.76	-0.76	-26.76	-33.76	5.24	6.24	59.24	34.24	132.24	41.24	-23.76	-133.76
RN26			33.88	110.88	5.88	-8.12	47.88	74.88	-33.12	5.88	88.88	78.88	65.88	52.88	0.88	-79.12	-148.12
RN27	-103.24	-57.24	-78.24	242.76	244.76	244.76	-109.24			68.76	6.76	-70.24	-6.24	-11.24	17.76	-31.24	-118.24
RN28			-7.41	47.59	168.59	140.59	-8.41		-61.41	-42.41	-118.41	10.59	42.59	92.59	6.59	116.59	-23.41
RN29			-126.59	-81.59	12.41	-91.59	-112.59	-88.59	-124.59		75.41	223.41	45.41	212.41	191.41	157.41	114.41
RN30				-55.00	-11.00	117.00	61.00		107.00	65.00			126.00	73.00	-10.00	120.00	25.00
RN31				-26.76		226.24	102.24	-3.76	-76.76	-85.76	24.24	52.24	174.24	27.24		94.24	96.24
RN33					32.12	164.12	81.12	62.12	4.12	39.12	-83.88	25.12	-4.88	47.12	62.12	77.12	18.12
RN34		3.12				-22.88		163.12	121.12	130.12	29.12	-95.88	-56.88	33.12	140.12	-8.88	59.12
RN37					20.53	31.53	-1.47	26.53	51.53	-29.47	74.53	98.53	7.53	-28.47	100.53	111.53	70.53
RN38		-106.29	91.71	-103.29	80.71	-65.29	97.71		-32.29	-109.29	71.71	54.71	-1.29	35.71	111.71	13.71	102.71
RN39						-1.24	35.76	84.76	113.76	63.76	57.76	-37.24	25.76		53.76	124.76	-34.24
RN40		37.35	51.35		-92.65				1.35	113.35			-0.65	91.35	230.35	173.35	71.35
RN42							-55.65	-52.65	19.35	47.35	114.35	44.35	220.35	174.35		107.35	92.35
RN43				-117.18	183.82	114.82	89.82	125.82	191.82	131.82			-123.18	-25.18	129.82	108.82

RN44									-37.00	112.00	-61.00	84.00	87.00	82.00	50.00	172.00	79.00
RN45		-63.88				36.12	60.12	10.12	73.12	-21.88		189.12	69.12	117.12	89.12	139.12	92.12
RN46		-1.29	-117.29	-52.29	59.71	74.71	24.71	-23.29	-53.29	36.71	21.71	31.71	24.71	54.71	5.71	17.71	40.71
RN47		-36.76	13.24	74.24	87.24	30.24	-2.76	-24.76	-26.76	-5.76	2.24	-30.76	-4.76	59.24	-0.76	32.24	-5.76
RN49	-81.24	-97.24			35.76	64.76	88.76	38.76		3.76	60.76	5.76	101.76	4.76	24.76	27.76	75.76
RN50				76.71	37.71	53.71	30.71	-62.29	33.71	-13.29	40.71	49.71	75.71	28.71	5.71	-5.29	41.71
RN51	-9.00	43.00	-37.00	-47.00	15.00	-111.00		3.00	63.00	-7.00	-97.00	-50.00	225.00	-86.00	8.00	173.00	39.00
RN52				98.65	72.65	-123.35	-3.35		-1.35	-5.35	77.65	79.65	149.65	72.65	20.65	6.65	68.65
RN53									40.12		25.12	-1.88	94.12	208.12	120.12	33.12	173.12
RN54						-64.82			55.18	103.18	2.18	90.18	90.18	112.18	48.18	102.18	34.18
RN58								87.29	60.29	-22.71	35.29	109.29	175.29	60.29	178.29	78.29	-35.71
RN59				-61.82	103.18	93.18	115.18	116.18	112.18	17.18				31.18	-4.82	3.18	20.18
RN60							93.35	92.35	80.35	134.35	79.35	-79.65	30.35	49.35	-88.65	101.35	117.35
RN61							104.82	121.82	75.82	58.82	72.82	102.82	5.82	0.82		129.82	20.82
RN63	-99.65	22.35	-21.65		16.35	-4.65	10.35	8.35	42.35	6.35	22.35	77.35	1.35	-20.65	19.35	73.35	-6.65
RN64						98.65	144.65	69.65	26.65	31.65	-17.35	-2.35	190.65	28.65	44.65	-50.35	-38.35
RN66		-101.00	28.00	-10.00	82.00	109.00	79.00				131.00	112.00	218.00	-32.00	8.00		
RN67					-81.76	25.24	-45.76	241.24	182.24	32.24	56.24	-32.76	43.24	117.24	-39.76	-63.76	61.24
RN68		-127.24	144.76	59.76	13.76	-56.24	6.76	-12.24	44.76	-4.24	8.76	-9.24	8.76	6.76	37.76	28.76	-12.24
RN70	-155.82	-31.82	-78.82	-115.82	79.18	172.18	39.18	-131.82	-130.82	177.18	-12.82	26.18	130.18	83.18	113.18	-45.82	-116.82
RN71					52.88	136.88	65.88	62.88	62.88	65.88	125.88	166.88	-63.12	-57.12	76.88		
RN72			62.18	99.18	112.18	97.18	47.18	48.18	66.18	24.18	-33.82	-78.82	-55.82	5.18	-40.82	21.18	-65.82
RN73				54.29	145.29	-63.71	-28.71	13.29		-44.71	44.29	52.29	84.29	-25.71	233.29	-7.71	70.29
RN74		31.88	-124.12	-14.12	-15.12	42.88	72.88	-35.12	27.88	193.88	12.88	-18.12	78.88	-86.12	85.88	3.88	-92.12
RN75		-82.35	-71.35	94.65	139.65	81.65	-0.35	-144.35	-98.35	84.65	25.65	94.65	43.65	-14.35	40.65	-38.35	1.65
RN76					110.29	27.29	102.29	21.29	49.29	-1.71	46.29	31.29	17.29	-93.71	39.29	107.29	14.29
RN77						-68.71	39.29	92.29	94.29	80.29	106.29	10.29	79.29	59.29	81.29	87.29	-92.71
RN78								81.12		-80.88	80.12	70.12	118.12	103.12	221.12	116.12	114.12

RN79				-78.06	-100.06	35.94	-29.06	54.94	4.94	13.94	39.94	-79.06	73.94	42.94	245.94	11.94	118.94
RN80						24.59	27.59	48.59	7.59	51.59	78.59	56.59	61.59	89.59	56.59	54.59	54.59

Table 15 Count the maximum consecutive n. of days per year per station that are required to transit from the yearly MEAN value (based on normalized ^{7}Be value) up to the yearly MAXIMA which is a variable threshold from year to year. The Maxima indicates when the convergence zone is closest to the station. The transit time between Mean and the Maxima indicate a time period of cell progression which is a proxy for Hadley cell circulation strengthening or weakening. The higher the number of days required to reach the maxima, the slower the cell progression, the weaker the circulation. N. of days are rounded to zero decimals. Dataset is based on 120 days averaged normalized ^{7}Be concentration corrected from cosmic rays.

Treaty number	2003	2004	2005	2006	2007	2008	2009	2010	2011	2012	2013	2014	2015	2016	2017	2018	2019
RN01	54	177	182	208	170	159	188	184	186	177	183	170	169	187	184	159	138
RN03		140	168	189	134		2	167	194	165	168	179	172	177	167	169	131
RN04	44	175	199	199	191	161	199	169	196	184	164	185	215	177	187	159	151
RN05												82	158	148	173	159	143	134
RN06	64	125	172	149	166	145	153	129	129	146	176	170	190	148	185	184	90
RN07											155	167	147	179	186	161	169	134
RN08	61	176	120	133	178	75	190	136	168	183	172	207	158	162	204	159	128
RN09	67	189	172	151	176	193	186	194	190	185	164	167	173	148	192	165	115
RN10	51	202	165	169	171	189	155	153	238	181	167	155	170	162	198	171	127
RN11	61	125	219	173	201	196	172	224	181	178	170	165	209	164	203	160	138
RN13						170	194	224	94	136	194	89		147	177	148	108
RN14							4	179	146	207	162	163	226	183	208	196	120
RN15			175	17	99	155	195	168	135	103	150	198	223	168	174	218	117
RN16	54	185	161	186	158	164	183	164	165	181	182	156	159	191	171	160	125
RN17				68	187	203	156	198	195	233	200	212	143	158	164	204	114
RN18	52	162	163		112	184	167	164	182	63	135	193	182	167	168	165	133
RN19	38		82	167	160				28	193	136	107	188	159	196	198	114
RN23	57	174	209	179	173	178	164	97	66	167	140	190	180	169	196	189	125
RN26			148	224	187	163	172	177	160	190	165	206	214	155	153	180	130
RN27	69	169	121	134	160	108	4			99	169	203	186	138	176	180	96

RN28			163	158	150	247	217		119	127	18	67	160	241	157	187	114
RN29		45	177	108	149	145	214	71	120	210	187	140	143	156	175	190	102
RN30				24	181	203	166	75	200	171	125		184	170	162	174	123
RN31			147	95	31	159	175	177	150	175	167	152	175	164	144	159	122
RN33					156	190	192	159	144	205	144	232	210	184	180	188	139
RN34	47	63			111	58		171	143	153	145	137	203	153	207	146	129
RN37					195	193	197	218	189	206	186	218	156	49	189	204	153
RN38	5	13	120	46	191	18	162	192	163	186	128	171	175	195	186	165	110
RN39					43	169	137	203	155	146	25	121	1		123	165	110
RN40		91	182	75	95	187	234	16	156	170	58		67	179	190	160	99
RN42							93	202	195	164	229	139	166	156	194	226	136
RN43				24	189	193	149	246	201	159	150	192	167	163	195	193	98
RN44									67	181	37	204	63	180	179	196	139
RN45	60	204	182	194	188	193	218	170	223	180	227	229	151	178	152	137	121
RN46	39	153	24	139	196	193	177	182	236	170	150	176	178	149	159	176	141
RN47	44	178	167	216	191	175	154	206	168	167	154	170	166	211	155	185	145
RN49	47	11			179	170	196	139	99	175	160	163	206	137	154	159	162
RN50			31	167	166	176	119	97	181	164	170	174	190	158	160	161	121
RN51	39	149	87	143	176	5		92	178	153	114	76	126	146	132	170	147
RN52				125	193	192	133	29	161	165	179	182	141	204	167	173	146
RN53									139	203	168	130	205	196	159	44	120
RN54						28			125	166	59	180	171	180	194	173	117
RN58								170	188	142	158	191	207	150	152	205	134
RN59					27	178	154	143	183	176	131		17	164	150	197	121
RN60						8	141	143	200	142	182	179	153	181	180	137	119
RN61							169	186	165	179	170	193	161	167	193	209	112
RN63	69	194	135		146	144	185	151	191	182	200	153	186	187	181	191	130
RN64					112	181	196	208	167	130	201	149	159	177	203	54	66
RN66		16	109	55	136	198	215	35	23	192	228	99	151	120	181	167	139
RN67					81	146	79	152	188	170	194	196	186	207	100	142	112

RN68		46	156	145	180	145	166	154	174	136	164	186	153	144	168	161	127
RN70		133	123		202	116	135	205	138	203	172	183	180	186	149	139	71
RN71					177	148	180	201	176	209	196	175	212	194	178	212	149
RN72		32	213	144	144	193	188	168	213	194	191	215	223	162	213	194	128
RN73				83	195	107	160	201	177	168	170	191	169	139	176	186	125
RN74	62	212	207	181	143	200	204	234	196	161	170	154	207	202	159	157	110
RN75	62	148	203	191	201	185	158	248	170	170	157	189	193	189	186	148	157
RN76					145	156	149	163	177	166	165	148	161	192	170	214	112
RN77						162	162	190	163	175	207	167	155	167	210	201	142
RN78							85	191	176	175	182	175	185	191	165	145	134
RN79			49	85	182	187	185	157	188	161	144	208	191	184	155	156	132
RN80						196	160	157	203	180	196	201	140	211	180	188	146

Table 16 Tropopause profile figure 4 is based on the below data table featuring ^{7}Be % of growth over the overall average and re-analysis of radiosonde data (aggregation of different grid resolution as presented in figure 1 of Schmidt et al. 2008). The correlation with ^{7}Be growth in 2017 is 0.81. Positive trend is in agreement with the re-analysis data. In 2019 the trend varies at the equator but we currently do not have re-analysis data from radiosonde of 2019 available. 2005, 2017, and 2019 are selected to show the tropopause growth trend.

IMS Station	^{7}Be % of Growth versus average along the Canadian-Antarctica profile				Aggregation of Re-analysis of radiosonde measurement (Schmidt et al. 2008)	
	Latitude	% (2005)	% (2017)	% (2019)	Latitude	mt/Yr (2001-2007)
RN73	-64.5		24.13	14.56	-75	40
RN18	-53.1	11.95	14.12	11.26	-68	18
RN03	-41.1	-6.14	-3.86	20.62	-55	-10
RN01	-34	-0.32	9.20	18.91	-35	45
RN11	-22.5	-6.59	-1.91	-7.54	-20	-5
RN50	8.9	-32.53	-9.82	19.98	9	-18
RN44	28		-5.70	5.45	19	2
RN70	38.7	-9.64	3.49	-10.63	30	37
RN14	49.3		-7.37	13.25	60	3
RN15	74.7	-6.77	8.97	8.56	85	28
Correlation between ^{7}Be % of growth and radio-sonde based data (2001-2007)	0.5	0.8	-0.1			

Annex B Supplementary Figures

See attachments.

Personal Data

Name: Lucrezia Terzi

Address: Krapfenwaldgasse 39, 1190 Wien

Date and place of birth: 25 March 1979, Bologna, Italy

Education:

2007 Laurea Magistrale (Bachelor and Master) in Geophysics at Universita Statale di Milano.

2003. IGPP, SCRIPPS, Inst. of Oceanography, San Diego, California. Thesis on Magnetotellurics (experimental part).

2002. Ecole Normale Superieure de Lyon, Lyon, France (Erasmus program).

Professional summary:

2020-Q1: Data analyst, Safeguards Division, International Atomic Energy Agency (IAEA)

2016- Present: Research scientist, Belgium Nuclear Research Centre (SCK.CEN)

2004- 2015 Comprehensive Nuclear Test Ban Treaty Organization (CTBTO)

Other:

2016-2019. Member of the Board of Governors of the Vienna International School.

Conference presentations (during the completion of this work):

2020. EGU2020 (online conference). A new comparative scale between tropopause height and beryllium 7. Online presentation via live chat.

2019. SCKCEN lunch talk (Mol, Belgium), EGU2019, SnT2019, Nuklearsymposium-2019 (Vienna, Austria). Climate change through the eyes of radioisotopes. Oral presentations.

2019. SnT2019 Panel discussion on Nuclear Technology for Climate Change.

2019. CFMIP2019 (Greece). Tropopause instability, how nuclear monitoring tracks climate change. Poster.

2019. AGU2019 (San Francisco, Ca, USA). Tropopause Instability, Weakening of Atmospheric Circulation and Poleward Movement of Hadley Cell: How Nuclear Monitoring Help Track Climate Change. Poster.

2018. EGU2018 (Vienna, Austria). New early warning indices for monsoon onset and withdrawal in all regions based on cosmogenic radionuclide ^{7}Be. Poster.

2017. AGU2017 (New Orleans, USA). Atmospheric ^{7}Be concentration changes as a possible new indicator for early warning on Indian Monsoon onset. Poster.

2017. EGU2017 (Vienna, Austria).
World-wide seasonal variation of ^{7}Be related to large-scale atmospheric circulation dynamics. Poster.
Use of IMS Data and Its Potential for Research Through Global Noble Gas Concentration Maps. Oral presentation.

2017. SnT2017 (Vienna, Austria). Use of IMS Data and Its Potential for Research Through Global Noble Gas Concentration Maps. Oral presentation.

2017. INGE2017 Workshop. Noble Gas Concentration Map for Global Emission Inventory Feedback. (London, UK). Oral presentation.

2017. Video interview related to the practical application of ^{7}Be time series for monsoon warning. http://www.unmultimedia.org/avlibrary/asset/1952/1952336/

2017. Prezi award for presentation on "World-wide seasonal variation of ^{7}Be related to large-scale atmospheric circulation dynamics" https://prezi.com/awards/

Patent:

An international patent application (PCT/EP2018/067982) has been filed to the European Patent Office on trans-equatorial approach and related methods as described in https://doi.org/10.1038/s41598-019-39664-7. PCT-application has been published on 9 January 2020 as WO2020/007454 A1.

List of publications

This thesis is based on the following papers.

Terzi L. and Kalinowski M. (2017) World-wide seasonal variation of ^{7}Be related to large-scale atmospheric circulation dynamics, Journal of Environmental Radioactivity, http://dx.doi.org/10.1016/j.jenvrad.2017.06.031

Terzi L., Kalinowski M., Schoeppner M., Wotawa G. (2019). How to predict seasonal weather and monsoons with radionuclide monitoring, Scientific Reports, https://doi.org/10.1038/s41598-019-39664-7

Abstract video: https://www.youtube.com/watch?v=lcATY_3UjSc

Terzi L., Wotawa G., Kalinowski M., Schoeppner M., Saey P., Steinmann P., Luan L. and Staten P.W. (2020) Radioisotopes demonstrate changes in global atmospheric circulation possibly caused by global warming. Accepted for publication at Scientific Reports.

Publications related press:

India, July 2019 https://www.thehindubusinessline.com/economy/agri-business/new-way-of-predicting-monsoon-could-help-farmers/article28322673.ece

India, July 2019 http://www.newindianexpress.com/nation/2019/jul/09/how-scientists-used-tech-meant-to-monitor-nuclear-explosions-to-predict-monsoon-2001353.html

India, July 2019 http://www.newindianexpress.com/states/tamil-nadu/2019/jul/09/nuke-stations-help-decode-the-monsoon-2001344.html

India, July 2019 https://krishijagran.com/agriculture-world/this-new-method-of-predicting-monsoon-could-help-indian-farmers/

Austria, June 2019
https://www.derstandard.at/story/2000104684459/wettervorhersage-mit-radioaktivem-blick

Belgium, March 2019 https://www.standaard.be/cnt/dmf20190227_04214418